QUANTUM IMAGING OF BIOSAMPLES

FLORENCE GRENAPIN

Thesis submitted to the University of Ottawa
in partial Fulfillment of the requirements for the
Master's degree in Physics

Department of Physics
Faculty of Science
University of Ottawa

Abstract

All far-field optical imaging is limited by diffraction from optical elements, a phenomenon called Rayleigh's curse. It has been shown that through the use of the spatial mode demultiplexing technique (SPADE), an arbitrarily small separation between two point sources can be resolved, given a sufficiently large total number of photons N. This quantum metrology approach to super-resolution has since then been demonstrated and generalized to more complex situations. We propose a variant of SPADE, that we call biphoton SPADE, applied to imaging systems with spatially entangled photon pairs generated through spontaneous parametric downconversion. Our method can achieve a higher precision than SPADE, given any non-zero level of entanglement. We furthermore demonstrate our technique in a coincidence imaging setup and show super-resolution while only projecting on a select few of the total optimal modes in the 2D joint basis. Since the method uses quantum light and provides even further sensitivity to SPADE, it can potentially be used in the future for various light-sensitive imaging applications and in combination with neural networks.

In nature, one often finds structures that have only been replicated by humans through years of precise, state-of-the-art engineering. Polymer spherulites, naturally occurring birefringent crystals that grow around defects in a radial pattern, are an example of this. We show through the example of ascorbic acid, commonly referred to as Vitamin C, that spherulites are capable of creating beams with orbital angular momentum (OAM) through a pro-

cess called spin-to-orbit coupling. This action of the ascorbic acid crystals is analogous to the one of spatially structured waveplates called q-plates, which are built to have an azimuthally dependant optic axis. This opens the door for potentially cheaper fabrication of q-plates, and possibilities of tuning the growth of the molecules for arbitrary wavefront shaping with natural crystals. Finally, because of the wide range of crystals in the spherulite class, further investigation into different spherulites could shed light on the relationship between crystal symmetry and structure, and the shaping of light.

Statement of Originality and Collaborative Contributions

To the best of her knowledge, the author states that the projects and work described in this Master's thesis constitute original research in the field of physics. The contributions of different collaborators on the two projects are described here.

Dr. Ebrahim Karimi was the supervisor for both projects of the thesis. Dr. Alessio D'Errico assisted Dr. Karimi in his supervision of both projects, as he was the postdoc overseeing most of my work. For section 2, Dilip Paneru, Dr. Alessio D'Errico and Dr. Karimi collaborated with me to establish a foundation for the theory of super-resolution with entangled light. Dilip Paneru set up most of the source for the generation of SPDC light, and contributed greatly to the analysis of the results. The idea of biphoton SPADE with coincidence counts as described in the publication, as well as the development of the theory, simulation, collection of data and analysis has been my work. I along with all included co-authors Dilip Paneru, Dr. Alessio D'Errico, Dr. Vincenzo Grillo, Dr. Gerd Leuchs, and Dr. Ebrahim Karimi contributed to writing the manuscript. For section 3, Dr. Karimi proposed the original idea, and Dr. Alessio D'Errico supervised and assisted throughout the different phases of the project; he also elevated the quality of the manuscript. I performed the data collection and analysis, with help from both Dr. Alessio D'Errico and Dr. Karimi. I along with co-authors Dr. Alessio D'Errico and Dr. Ebrahim Karimi contributed to writing the manuscript.

Acknowledgements

Many thanks to Dr. Ebrahim Karimi for welcoming me in the group as an undergraduate student. He has always pushed me and all our group members to take on a wide variety of projects, to develop our own ideas, and to experience more learning and teaching opportunities. I am grateful for the kindness in our conversations and his support regardless of my career decisions; I wish him luck with the group in the future.

A very big thank you to Dr. Alessio D'Errico for overseeing my projects, for his kindness and his cool even while overflowing with tasks to do. I appreciated having someone so reliable to help debug and to focus efforts when needed, it really made the difference for me. Thank you.

Another person to acknowledge is Dilip Paneru. We have worked on the same corner of a table for two years, brainstorming through the puzzle of super-resolution from a ghost imaging perspective. I appreciated his knowledge in Python and Mathematica, and his contribution to the manuscript this year, despite his other engagements. Thank you to Manuel, Felix, Alicia, Xiaoqin and Nazanin for making the group a more fun place.

Finally, I'd like to give a huge thanks to my friends and family for motivating me and supporting me throughout my studies. I would not have done it without them.

Contents

1 Introduction **1**

1.1 Introduction to Waveplates 1

1.1.1 Wavefront shaping with PBOEs 6

1.1.2 Biaxial Birefringence 10

1.1.3 Motivation 14

1.2 Relevant Quantum Mechanics Notations 14

1.3 Spontaneous Parametric Down Conversion 17

1.4 Projection Method 21

2 Super-resolution **25**

2.1 Introduction to Super-resolution 25

2.1.1 Rayleigh's Curse 25

2.1.2 Increasing resolution 28

2.1.3 Increasing resolution in low photon regime 29

2.1.4 Mode sorting super-resolution (SPADE) 31

2.1.5 In the presence of noise 35

2.1.6 Motivation 36

2.2 Methods 37

2.2.1 Fisher Information in an entangled imaging setup . . . 37

2.2.2 Introducing a separation 42

2.2.3 Estimation 45

2.3 Publication 48

3 Spin-Orbit Coupling in Spherulite Crystals **61**

3.1 Methods 62

3.1.1 Polarization Tomography 62

3.1.2 Interferometry 68

3.1.3 Fabrication 69

3.2 Publication 70

4 Conclusion **78**

List of Tables

1 Jones vector notations for polarization bases 3

2 Expressions for generalized waveplate actions 6

List of Figures

1 Optic axes of birefringent mediums 2

2 Optic axes varying locally as a function of radius and angle . . 7

3 Intensity collected during tomographic measurements 9

4 Indicatrix ellipsoid for biaxial birefringent mediums 11

5 Biaxial crystals with a twisting local axis. 13

6 Type I SPDC 18

7 Hermite-Gauss modes 19

8 Schmidt Decomposition of SPDC 20

9 Phase-Amplitude Hologram 22
10 Generating and selecting the first order of diffraction. 23
11 Rayleigh's curse in 2D and 3D 26
12 Fraunhofer diffraction 27
13 Experimental setup for QGI 30
14 Traditional SPADE 34
15 Traditional SPADE with noise 36
16 Setup for incoherent separation 43
17 Experimental setup for the biphoton SPADE technique 44
18 Experimental data versus no-noise model probabilities 45
19 Experimental data versus no-noise non-schmidt model 61
20 Polarization tomography basics 64
21 $I_{H,V,L,R,A,D}$ collected during polarization tomography process . 66
22 Stokes parameters calculated from the experimental data . . . 66
23 Polarization profile of ascorbic acid shaped light 67
24 Experimental setup for real-time polarization tomography . . 67
26 Microscope images of ascorbic acid 78

1 Introduction

This thesis is a compilation of the work that I undertook throughout my Master's. It appears as two sections, defined by two separate projects. Section 2 consists of work on a biphoton super-resolution project, using spatial correlations in an entangled photon pair to achieve results that surpass conventional mode sorting super-resolution. Section 3 discusses the potential for naturally occuring crystals, in particular ascorbic acid, to be used as waveplates that generate vector vortex beams through spin-to-orbit coupling. These two projects are quite different in nature, however; they both offer novel insight related to structured light which will be shown in their respective sections. In this introductory section, we present the basic concepts on which both projects are based, namely: birefringence, notations around wavefunctions, entanglement, and projective measurements.

1.1 Introduction to Waveplates

A light field $\mathbf{E}$ normally incident on a medium of length d and of uniform refractive index n acquires a phase upon propagation of $\theta = \frac{2\pi nd}{\lambda}$, which is expressed as a phase retardation in the light field of $\mathbf{E}e^{i\theta}$. At the microscopic level, this phase is due to electrons being excited by the field passing through the material. In regions with high electron density, such as in axes where molecules have double bonds, the phase retardation is higher as more electrons absorb energy.

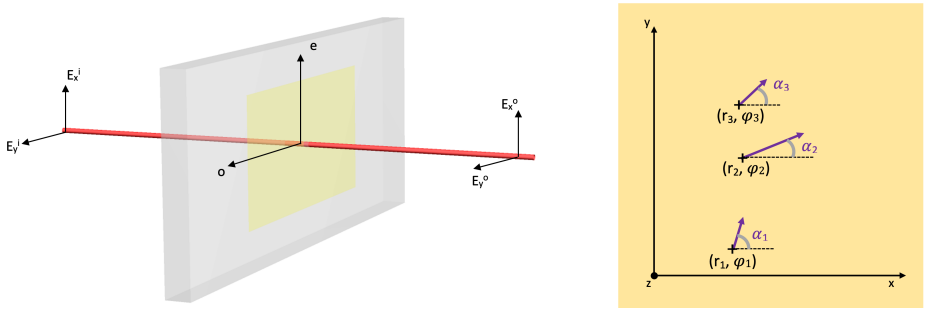

Figure 1: **Left.** Schematic of a birefringent element with extra-ordinary and ordinary optical axes aligned with the horizontal and vertical components of the electric field, respectively. Each electric field component of the red light depicted interacting with the sample acquires a different phase shift, as shown in Eq.(1). **Right.** Simple graph depicting local optic axis angles $\alpha(r_i, \phi_i)]$ in the transverse plane.

In a birefringent medium like some crystals, unless propagating in the direction of the optic axis, the refractive index experienced by the light field is dependent on its direction of oscillation: the polarization component oscillating along the plane of the optic axis of the medium will experience an "extraordinary refractive index" n_e, while the polarization component perpendicular to that axis will experience an "ordinary refractive index" n_o. In the simplest case, the optic axis is chosen to be along the plane of the crystal, perpendicular to the field's propagation direction. The phase retardation between both polarization directions will then be $e^{i\Delta n d \frac{2\pi}{\lambda}}$, where $\Delta n = |n_e - n_o|$.

To keep track of the changes of different polarization components of $\mathbf{E}$, it is useful to adopt the Jones formalism for representing amplitude and phase of electric fields in the transverse plane, see Table[1].

H-V polarization Basis	Circular Polarization Basis
$\|H\rangle = \begin{pmatrix}1\\0\end{pmatrix}$, $\|V\rangle = \begin{pmatrix}0\\1\end{pmatrix}$	$\|H\rangle = \frac{1}{\sqrt{2}}\begin{pmatrix}1\\1\end{pmatrix}$, $\|V\rangle = \frac{1}{\sqrt{2}}\begin{pmatrix}1\\-1\end{pmatrix}$
$\|L\rangle = \frac{1}{\sqrt{2}}\begin{pmatrix}1\\i\end{pmatrix}$, $\|R\rangle = \frac{1}{\sqrt{2}}\begin{pmatrix}1\\-i\end{pmatrix}$	$\|L\rangle = \begin{pmatrix}0\\1\end{pmatrix}$, $\|R\rangle = \begin{pmatrix}1\\0\end{pmatrix}$
$\|D\rangle = \frac{1}{\sqrt{2}}\begin{pmatrix}1\\1\end{pmatrix}$, $\|A\rangle = \frac{1}{\sqrt{2}}\begin{pmatrix}1\\-1\end{pmatrix}$	$\|D\rangle = \frac{1}{2}\begin{pmatrix}1+i\\1-i\end{pmatrix}$, $\|A\rangle = \frac{1}{2}\begin{pmatrix}1-i\\1+i\end{pmatrix}$

Table 1: Jones vector notations for two different polarization bases. Equations in the paper are written in the circular basis, but will be derived here in the H-V basis. One can obtain one from the other with the transition matrix $P = \sqrt{\frac{1}{2}}\left(\begin{smallmatrix}1 & i\\ 1 & -i\end{smallmatrix}\right)$.

So, a general EM field's transverse amplitude and phase can be represented as $\mathbf{E} = E_x\mathbf{x} + E_y\mathbf{y} = \left(\begin{smallmatrix}E_x\\ E_y\end{smallmatrix}\right)$. If the extraordinary and ordinary local axes are respectively aligned with the horizontal and vertical polarization components Fig.(1) then the EM field components are modified by the birefringent element in the following way:

$$\begin{aligned}\begin{pmatrix} E_x^o \\ E_y^o \end{pmatrix} &= \begin{pmatrix} e^{i\frac{2\pi}{\lambda}dn_e} & 0 \\ 0 & e^{i\frac{2\pi}{\lambda}dn_o} \end{pmatrix} \begin{pmatrix} E_x^i \\ E_y^i \end{pmatrix} \\ &= e^{i\frac{2\pi}{\lambda}dn_e} \begin{pmatrix} 1 & 0 \\ 0 & e^{i\frac{2\pi}{\lambda}d(n_o-n_e)} \end{pmatrix} \begin{pmatrix} E_x^i \\ E_y^i \end{pmatrix} \\ &= \Gamma \begin{pmatrix} 1 & 0 \\ 0 & e^{i\eta} \end{pmatrix} \begin{pmatrix} E_x^i \\ E_y^i \end{pmatrix}. \end{aligned} \tag{1}$$

where $-\pi \leqslant \eta = e^{i\frac{2\pi}{\lambda}d(n_o-n_e)} \leqslant \pi$ is the phase retardation and $\Gamma = e^{i\frac{2\pi}{\lambda}dn_e}$ is a constant phase factor acquired through the birefringent element. The matrix $\left(\begin{smallmatrix} 1 & 0 \\ 0 & e^{i\eta} \end{smallmatrix}\right)$ represents the action of a waveplate with fast/slow axes aligned with the H-V basis. More generally, we can consider a birefringent element with fast/slow axes angles that vary with (r, ϕ) in the transverse plane of propagation (see Fig.(1)). It then makes more sense to refer to the axis angle α between the fast axis and the horizontal direction as a local axis $\alpha(r, \phi)$, since the angle is free to vary point by point across the element. At a localized point, the orthogonal polarization components that will experience

the phase shifts of $e^{i\frac{2\pi}{\lambda}dn_e}, e^{i\frac{2\pi}{\lambda}dn_o}$ are aligned with the fast/slow axes:

$$\begin{pmatrix} E_e^i \\ E_o^i \end{pmatrix} = \mathcal{R}(\alpha) \begin{pmatrix} E_x^i \\ E_y^i \end{pmatrix} = \begin{pmatrix} cos(\alpha) & sin(\alpha) \\ -sin(\alpha) & cos(\alpha) \end{pmatrix} \begin{pmatrix} E_x^i \\ E_y^i \end{pmatrix}. \tag{2}$$

After passing through the element, those polarization components have acquired the phase shift expressed in Eq.(1):

$$\begin{pmatrix} E_e^o \\ E_o^o \end{pmatrix} = \begin{pmatrix} 1 & 0 \\ 0 & e^{i\eta} \end{pmatrix} \begin{pmatrix} cos(\alpha) & sin(\alpha) \\ -sin(\alpha) & cos(\alpha) \end{pmatrix} \begin{pmatrix} E_x^i \\ E_y^i \end{pmatrix}. \tag{3}$$

So, rotating back to the H-V basis we get the expression for the action $WP_{gen}(\alpha)$ of a general waveplate with a fast/slow axis local angle $\alpha(r, \phi)$:

$$\begin{aligned} \begin{pmatrix} E_x^o \\ E_y^o \end{pmatrix} &= WP_{gen}(\alpha) \begin{pmatrix} E_x^i \\ E_y^i \end{pmatrix} \\ &= \mathcal{R}(-\alpha)\Gamma \begin{pmatrix} 1 & 0 \\ 0 & e^{i\eta} \end{pmatrix} \begin{pmatrix} cos(\alpha) & sin(\alpha) \\ -sin(\alpha) & cos(\alpha) \end{pmatrix} \begin{pmatrix} E_x^i \\ E_y^i \end{pmatrix} \\ &= \Gamma \begin{pmatrix} cos(\alpha) & -sin(\alpha) \\ sin(\alpha) & cos(\alpha) \end{pmatrix} \begin{pmatrix} 1 & 0 \\ 0 & e^{i\eta} \end{pmatrix} \begin{pmatrix} cos(\alpha) & sin(\alpha) \\ -sin(\alpha) & cos(\alpha) \end{pmatrix} \begin{pmatrix} E_x^i \\ E_y^i \end{pmatrix} \end{aligned}$$

$$= \Gamma \begin{pmatrix} cos^2(\alpha) + sin^2(\alpha)e^{i\eta} & cos(\alpha)sin(\alpha)(1 - e^{i\eta}) \\ cos(\alpha)sin(\alpha)(1 - e^{i\eta}) & sin^2(\alpha) + cos^2(\alpha)e^{i\eta} \end{pmatrix} \begin{pmatrix} E_x^i \\ E_y^i \end{pmatrix}. \quad (4)$$

Half-Wave Retardation	Quarter-Wave Retardation
$HWP(\alpha) = \Gamma \begin{pmatrix} cos(2\alpha) & sin(2\alpha) \\ sin(2\alpha) & -cos(2\alpha) \end{pmatrix}$	$QWP(\alpha) = \Gamma \begin{pmatrix} cos^2(\alpha) + isin^2(\alpha) & sin(\alpha)cos(\alpha)(1-i) \\ sin(\alpha)cos(\alpha)(1-i) & sin^2(\alpha) + icos^2(\alpha) \end{pmatrix}$
$HWP(0) = \Gamma \begin{pmatrix} 1 & 0 \\ 0 & -1 \end{pmatrix}$	$QWP(0) = \Gamma \begin{pmatrix} 1 & 0 \\ 0 & i \end{pmatrix}$

Table 2: Expressions for waveplates with two different values of phase retardation. The expressions for $\alpha(r, \phi) = c$, where c is a constant, are those of the common half waveplates (HWPs) and quarter waveplates (QWPs) with the fast/slow axis at an angle of α with respect to the H-V basis. The matrices for $\alpha = 0$ in particular are shown.

We can distinguish different categories of waveplates, in particular those with half-wave retardation ($\Gamma = e^{i\pi}$) and those with quarter-wave retardation ($\Gamma = e^{i\pi/2}$) - see Table [2].

1.1.1 Wavefront shaping with PBOEs

The type of waveplates seen in the previous section, with local optic axis angles $\alpha(r, \phi)$ that vary along the transverse plane, are also called Pancharatnam Berry Optical Elements (PBOEs). This appellation refers to the Pancharatnam Berry phase that the polarization states acquire through propagation across the sample that allow for an arbitrary shaping of the field's

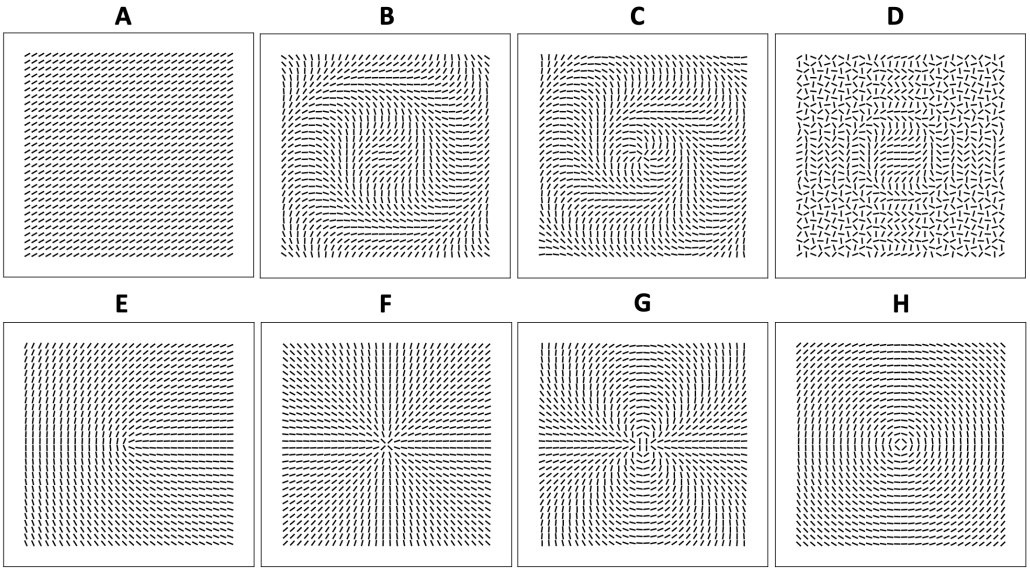

Figure 2: Local optic axes plotted for different expressions of $\alpha(r,\phi)$. **A.** $\alpha(r,\phi) = 0$. **B.** $\alpha(r,\phi) = r$. **C.** $\alpha(r,\phi) = r + \phi$. **D.** $\alpha(r,\phi) = r^2$. **E.** $\alpha(r,\phi) = \frac{\phi}{2}$. **F.** $\alpha(r,\phi) = \phi$. **G.** $\alpha(r,\phi) = 2\phi$. **H.** $\alpha(r,\phi) = \phi + \pi/2$

wavefront as a function of input polarization [1].

We can find the output field expression by taking Eq.(1) and choosing conditions of phase retardation and input polarization. At half-wave retardation and horizontal input polarization:

$$E_{out}^{H} = \Gamma \begin{pmatrix} cos(2\alpha) & sin(2\alpha) \\ sin(2\alpha) & -cos(2\alpha) \end{pmatrix} \begin{pmatrix} 1 \\ 0 \end{pmatrix} = \frac{\Gamma e^{i2\alpha}}{2} \begin{pmatrix} 1 \\ 1 \end{pmatrix} + \frac{\Gamma e^{-i2\alpha}}{2} \begin{pmatrix} 1 \\ -1 \end{pmatrix}. \quad (5)$$

At half-wave retardation and with circular input polarizations:

$$E_{out}^{L,R} = \Gamma \begin{pmatrix} cos(2\alpha) & sin(2\alpha) \\ sin(2\alpha) & -cos(2\alpha) \end{pmatrix} \begin{pmatrix} 1 \\ \pm i \end{pmatrix} = \frac{\Gamma e^{\pm i2\alpha}}{2} \begin{pmatrix} 1 \\ \mp i \end{pmatrix}. \quad (6)$$

The waveplate introduces a phase factor $e^{\pm i2\alpha}$ where α is again dependent on the beam's transverse coordinates, thus introducing a shape onto the beam's wavefront. For example, if $\alpha \propto r^2$ the waveplate can act as a sort of localized lens, and if $\alpha \propto \phi$ the wavefront introduces an azimuthal phase factor $e^{il\phi}$ typical of vector vortex beams carrying orbital angular momentum(OAM) [3]. Note that Γ is simply a complex coefficient so the wavefront shaping is determined entirely by the phase factor in α. The results can be similarly found for other input polarizations, and other phase retardations.

Waveplates dubbed "q-plates" have a local axis distribution described as above, where $\alpha(r, \phi) = q\phi + a_0$. The value of q is called the topological charge, it is determined by the orientation of the molecules in the transverse plane and can take integer or half-integer values. These q-plates impart a phase factor $e^{i2\phi}e^{2\alpha_0}$ to the output field, thus generating vector vortex beams with an angular momentum of twice the topological charge (OAM$= 2q$), through a process called spin-to-orbit coupling. Indeed, we can see from Eq.(6) that such a q-plate inverts the polarization handedness of the input beam and introduces a factor $e^{il\phi}$: there is conversion of input spin angular momentum to orbital angular momentum.

$$E_{out}^{L,R} = \Gamma_{new} \frac{e^{\pm i2\phi}}{2} \begin{pmatrix} 1 \\ \mp i \end{pmatrix}.$$

In nature, we expect to find birefringent crystal structures with low topo-

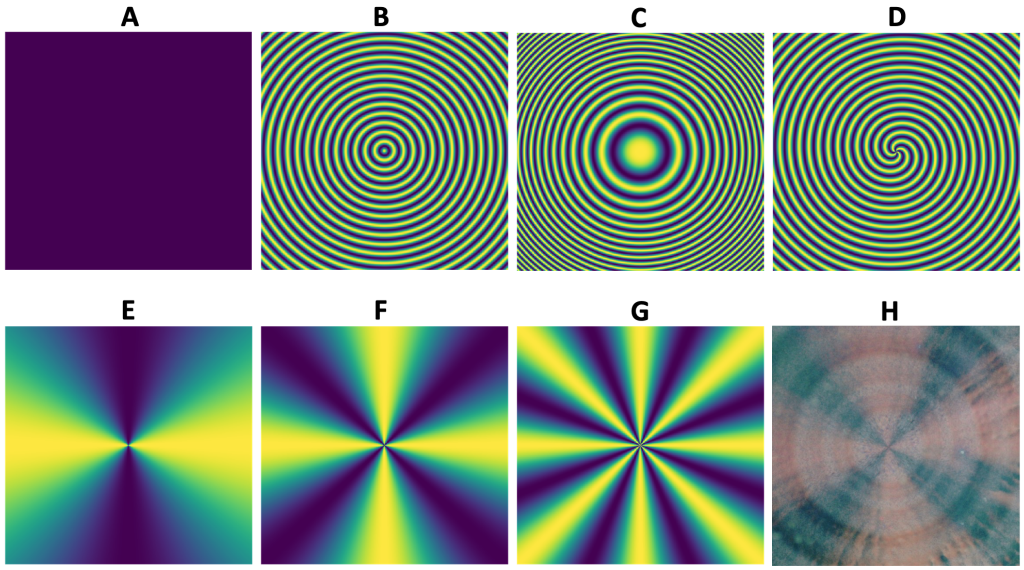

Figure 3: **A-G:** Intensity of E^H_{out} after projection onto vertical polarization state, for different values of $\alpha(r,\phi)$. Simulates image seen through cross polarizers. **A.** $\alpha(r,\phi) = 0$. **B.** $\alpha(r,\phi) = r$. **C.** $\alpha(r,\phi) = r^2$. **D.** $\alpha(r,\phi) = r + \phi$. **E.** $\alpha(r,\phi) = \frac{\phi}{2}$. **F.** $\alpha(r,\phi) = \phi$. **G.** $\alpha(r,\phi) = 2\phi$. **H.** Image of an ascorbic acid crystal defect through the crossed polarizers of a polarizing microscope. The cross like pattern typical of polymer spherulites is called a "Maltese pattern".

logical charges as their configuration is more energetically favorable. (It is however possible with liquid crystal technology to engineer q-plates imparting high values of OAM [2].) As seen Fig.(3) polymer spherulites such as ascorbic acid crystals, under cross-polarizers, manifest the same intensity patterns as q-plates with $q = 1$. In our publication 2.3, we study the optical properties of ascorbic acid crystals as half-wave retardation PBOEs and confirm their ability to generate vector vortex beams. Perhaps by influencing the crystallization process of spherulite crystals it would be possible to engineer

different topological charges or completely different optic axis distributions across the sample.

1.1.2 Biaxial Birefringence

In a biaxial birefringent crystal, all three crystallographic axes have different refractive indices. By convention the largest, intermediate and smallest refractive indices are n_γ, n_β and n_α respectively, and can be represented by an indicatrix ellipsoid unit (see Fig.(4)). In the previous sections, Jones matrices of waveplates were obtained assuming a uniaxial crystal structure with one optic axis. The results are identical with biaxial crystals if the N_1 and N_2 axis are constrained to the plane of incidence of the EM field.

More particularly, Eq.(1) in section 1.1 was obtained considering an optic axis N_1 in the x-y plane rotated about the z axis (also the N_3 axis) at an angle α. In nature however, crystals are not necessarily built with the condition that the optic axis remains in the x-y plane. There can be two additional rotations of the indicatrix about the N_1 or N_2 axes. We can thus find a more general expression for the action of a unixial or biaxial waveplate, considering these additional rotations. (Note that uniaxial crystals are symmetrical about the optic axis N_1, so rotations about that axis of the indicatrix will not change the expression found previously.)

In a similar derivation as above, we find that the EM field components travelling through a biaxial waveplate that has not been rotated with respect to the x, y, z axes is:

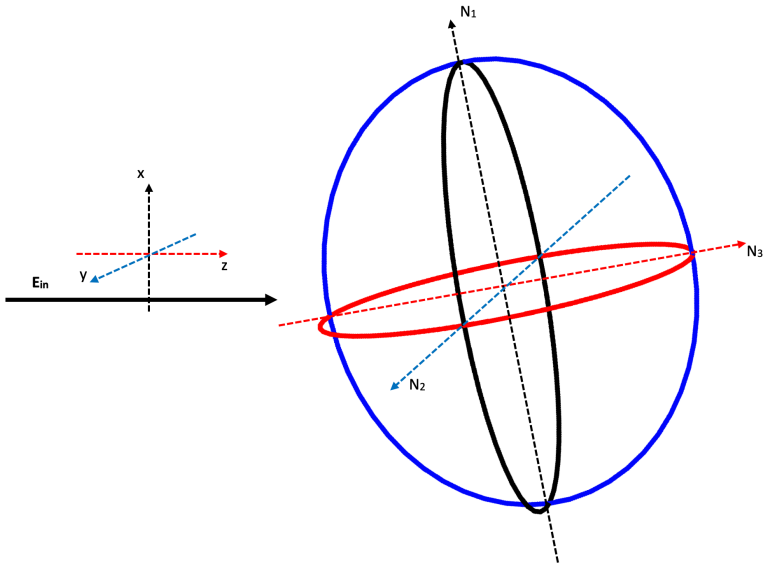

Figure 4: Representation of a local indicatrix ellipsoid, with three axes N_1, N_2, N_3 rotated by angles α, β, γ with respect to the x, y, z axes of the input field E_{in}. In the case of a uniaxial crystal, two of the three refractive indices along the indicatrix axes are equal.

$$\begin{pmatrix} E_x^o \\ E_y^o \\ E_z^o \end{pmatrix} = \begin{pmatrix} e^{i\frac{2\pi}{\lambda}dn_\gamma} & 0 & 0 \\ 0 & e^{i\frac{2\pi}{\lambda}dn_\beta} & 0 \\ 0 & 0 & e^{i\frac{2\pi}{\lambda}dn_\alpha} \end{pmatrix} \begin{pmatrix} E_x^i \\ E_y^i \\ E_z^i \end{pmatrix}$$
$$= \begin{pmatrix} \Gamma_\gamma & 0 & 0 \\ 0 & \Gamma_\beta & 0 \\ 0 & 0 & \Gamma_\alpha \end{pmatrix} \begin{pmatrix} E_x^i \\ E_y^i \\ E_z^i \end{pmatrix}. \quad (7)$$

Applying rotations about 3 axes:

$$WP_{gen}(\alpha,\beta,\gamma) = R_z(-\alpha)R_x(-\beta)R_y(-\gamma)\begin{pmatrix}\Gamma_\gamma & 0 & 0\\ 0 & \Gamma_\beta & 0\\ 0 & 0 & \Gamma_\alpha\end{pmatrix}R_y(\gamma)R_x(\beta)R_z(\alpha), \tag{8}$$

where R_x, R_y, R_z are the 3D rotation matrices with rotation around the x, y, z axes, respectively. Assuming again an EM field travelling in the z direction, the general waveplate expression becomes a more complex matrix, written out element by element as:

$$\begin{aligned}
WP_{gen}[11] &= \Gamma_\gamma C_\alpha^2 C_\gamma^2 - \Gamma_\alpha S_\gamma(S_\alpha S_\beta - C_\alpha C_\beta S_\gamma) + \Gamma_\beta C_\gamma S_\alpha(C_\beta S_\alpha + C_\alpha S_\beta S_\gamma),\\
WP_{gen}[12] &= -\Gamma_\gamma C_\alpha C_\gamma^2 S_\alpha - \Gamma_\alpha S_\gamma(C_\alpha S_\beta + C_\beta S_\alpha S_\gamma) + \Gamma_\beta C_\gamma S_\alpha(C_\alpha C_\beta - S_\alpha S_\beta S_\gamma),\\
WP_{gen}[21] &= \Gamma_\alpha C_\gamma S_\beta(S_\alpha S_\beta - C_\alpha C_\beta S_\gamma) + \Gamma_\gamma C_\alpha C_\gamma(-C_\beta S_\alpha + C_\alpha S_\beta S_\gamma)\\
&+ \Gamma_\beta(C_\beta S_\alpha + C_\alpha S_\beta S_\gamma)(C_\alpha C_\beta + S_\alpha S_\beta S_\gamma),\\
WP_{gen}[22] &= \Gamma_\alpha C_\gamma S_\beta(C_\alpha S_\beta + C_\beta S_\alpha S_\gamma) - \Gamma_\gamma C_\gamma S_\alpha(-C_\beta S_\alpha + C_\alpha S_\beta S_\gamma)\\
&+ \Gamma_\beta(C_\alpha C_\beta - S_\alpha S_\beta S_\gamma)(C_\alpha C_\beta + S_\alpha S_\beta S_\gamma),
\end{aligned} \tag{9}$$

where $C_i = Cos[i]$, $S_j = Sin[j]$. Note that for $\beta = 0$, $\gamma = 0$ the matrix reduces to Eq.(6) where the slowest axis and the intermediate axis are in the x-y plane. An EM field passing through such a waveplate, between cross polarizers (H, then V), has an output intensity described as the modulus

square of Eq.(9). Note that the equations in Eq.(9) are derived considering polarization components only, which are valid inside the crystal. The output field is affected by additional refraction effects which have not been described by Jones polarization matrices here.

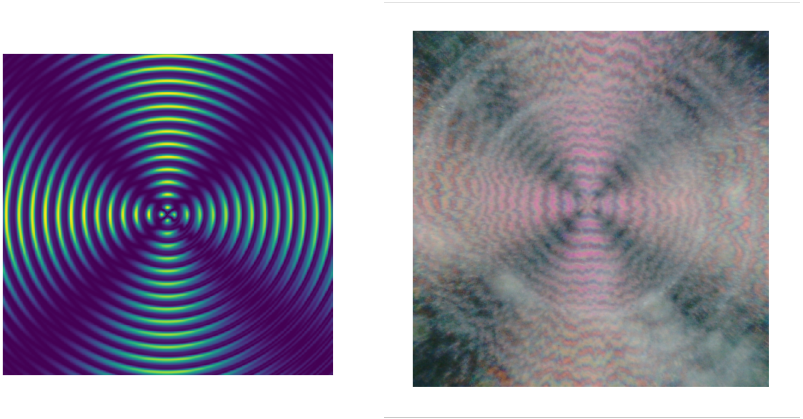

Figure 5: **Left**. Simulation of intensity seen through cross polarizers, assuming the crystals grow with a slight twist about the slow axis. **Right**. Image of Ascorbic acid between cross polarizers, exhibiting double banded Maltese cross patterns.

For $\alpha = \phi$, $\beta = 0.157$, $\gamma \propto r$ and similar birefringence values as in ascorbic acid crystals, the output intensity pattern becomes Maltese patterns with double banded concentric rings - see Fig.(5). At higher temperatures during crystal growth, the ascorbic acid crystals exhibited these concentric patterns. However for thin, mostly planar crystals, the expression derived previously Eq.(1) remains a good approximation. Indeed, the condition of thin crystals assures that the molecules mostly grow along the plane of incidence, assuring that rotations of the molecules along N_2 or N_3 are minor.

1.1.3 Motivation

After reviewing the previous literature, to the best of our knowledge, the light structuring ability of polymer spherulites such as ascorbic acid has not yet been explored. We will confirm by means of polarization tomography and interferometry in Section 3, the wavefront shaping induced by the ascorbic acid crystal and the OAM acquisition of light passing through the natural spherulite waveplate.

1.2 Relevant Quantum Mechanics Notations

In Section 2, we deal with wavefunctions of photons in order to make sense of the physics of imaging systems. This subsection serves as a reminder of basic definitions and operations concerning wavefunctions [3, 4, 5].

Spatial wavefunctions are descriptions of the quantum state of a quantum system in the transverse plane of propagation that satisfy the Schrödinger wave equation. They exist as vectors in a Hilbert space of infinite dimension that is spanned by orthogonal bases of spatial modes (e.g. Hermite-Gauss modes and Laguerre-Gauss modes). As such any spatial wavefunction $\Psi(x, y)$ represented in the bra-ket notation as the state $|\Psi\rangle$, can be expressed as a linear combination of a particular basis $\{\mathcal{B}_i, i \in \mathbb{N}\}$ of spatial modes:

$$|\Psi\rangle = \sum_i a_i \, |\mathcal{B}_i\rangle \,, \tag{10}$$

where $a_j = \sqrt{\mathcal{P}_j}$ are the complex probability amplitudes that the system be in the state $|\mathcal{B}\rangle$. The scalar product defined on the Hilbert space, like any other scalar product, determines the projection of two vectors in that space. It is defined in Eq.(11), where $\Psi^*(x, y)$ is the complex conjugate of $\Psi(x, y)$:

$$\langle \Psi_u | \, \Psi_v \rangle = \int_{-\infty}^{+\infty} \int_{-\infty}^{+\infty} \Psi_u^*(x, y) \cdot \Psi_v(x, y) dx dy. \tag{11}$$

Wavefunctions representing physical states are normalized, meaning that they satisfy $\langle \Psi | \, \Psi \rangle = 1$. There exist pure and mixed states in quantum mechanics. Pure states can be represented by a single wavefunction, expressed as linear combination of modes such as in Eq.(10). Mixed states are a probabilistic mixture of pure states. They cannot be represented as a single wavefunction, as the state is either entirely in one mode or another, with a certain probability associated to the uncertainty. It is thus easier to represent all states with density matrices:

$$\rho = \sum_i c_i^2 \, |\Psi_i\rangle\langle\Psi_i| \, , \tag{12}$$

where c_i^2 are the probabilities that the state is in the pure state $|\Psi_i\rangle$. The general expression for the probability that upon measurement, a state (pure or mixed) with density matrix ρ projects onto an arbitrary state $|\psi\rangle$ is:

$$\mathcal{P}_\psi = \langle \psi | \, \rho \, | \psi \rangle \tag{13}$$

$$= \sum_i c_i^2 \langle\psi|\,\Psi_i\rangle\langle\Psi_i|\,\psi\rangle$$
$$= \sum_i c_i^2 |\langle\psi|\,\Psi_i\rangle|^2.$$

A wavefunction can also represent the state of two or more distinguishable photons, as a separable product of wavefunctions in their own Hilbert space, $\Psi_{a,\ldots,n} = \Psi_a \otimes \ldots \otimes \Psi_n$, which we can write out as in Eq.(10):

$$\Psi_{a,\ldots,n} = \sum_i a_i \,|\mathcal{B}\rangle_i \otimes \ldots \otimes \sum_i n_i \,|\mathcal{B}\rangle_i \,.$$

Wavefunctions representing entangled multiphoton states cannot be separated in the same way and can generally be written out as in Eq.(14). Note that the formalism here only describes entangled photons that are otherwise distinguishable in another degree of freedom.

$$\Psi_{1,\ldots,n} = \sum_\alpha \ldots \sum_\eta A_{\alpha,\ldots,\eta}\,|\mathcal{B}_\alpha\rangle_1 \otimes \ldots \otimes |\mathcal{B}_\eta\rangle_n \,. \tag{14}$$

Density matrices ρ_m of multiphoton states are obtained as in Eq.(12), where Ψ_i are the multiphoton wavefunctions composing the state. The single photon density matrix can be calculated from the multiphoton one in the following way:

$$\rho_s^i = Tr_{1,\ldots,i-1,i+1,\ldots,n}[\rho_m] \tag{15}$$
$$= \sum_{\alpha,\ldots,\eta-1} {}_1\langle\mathcal{B}_\alpha| \otimes \ldots \otimes {}_n\langle\mathcal{B}_{\eta-1}|\rho_m\,|\mathcal{B}_{\eta-1}\rangle_n \otimes \ldots \otimes |\mathcal{B}_\alpha\rangle_1 \,. \tag{16}$$

For example, an entangled two particle system $\Psi_{1,2} = \sum_{a,b} A_{a,b} \left|\mathcal{B}_a\right\rangle_1 \otimes \left|\mathcal{B}_b\right\rangle_2$ has a density matrix $\rho_m = \left|\Psi_{1,2}\right\rangle\left\langle\Psi_{1,2}\right|$ and a single photon density matrix $\rho_s^i = \sum_{\alpha,\beta,\gamma} A_{\alpha,\beta} A^*_{\alpha,\gamma} \left|\mathcal{B}_\alpha\right\rangle_j {}_j\left\langle\mathcal{B}_\alpha\right|$, $i \neq j$.

1.3 Spontaneous Parametric Down Conversion

SPDC is a nonlinear process in which an incident pump photon of higher energy is converted into a pair of lower energy photons called signal and idler photons, via a non-linear crystal [6, 7].

In a non-linear dielectric material such as the type I BBO crystal which used in our experiment, an incident pump field will generate a polarization P that has nonlinear components. Assuming the pump field is relatively weak, only the linear $P_i^L = \epsilon_0 \chi E_i$ and bilinear components $P_i^{NL} = \chi_{ijk} E_j E_k$ will dominate. This nonlinear contribution adds a term in the interaction Hamiltonian inside the crystal, which results in the creation of two photons, and the annihilation of the pump photon.

Only specific polarizations of the pump, idler and signal modes satisfy the phase matching conditions inside the crystal. For type I phase matching, idler and signal share the same polarization state orthogonal to the pump photon's polarization. The expression of the biphoton state generated by the SPDC process with a Gaussian pump shape, where $q_{i,s}$ are the transverse wavevectors of signal and idler, Δk is the phase mismatch in the phase matching process, L is the dimension of the crystal, w_p the width of the pump

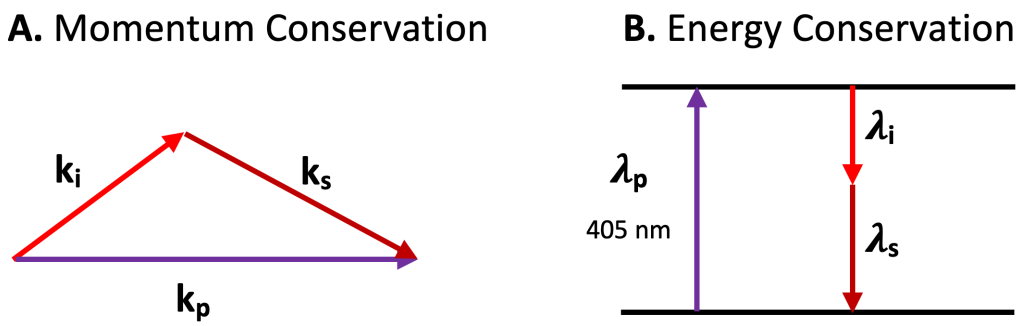

Figure 6: **A.** The momentum conservation of the photons implies that the wave vectors obey $k_s + k_i = k_p$. **B.** Energy conservation implies $\frac{1}{\lambda_p} = \frac{1}{\lambda_s} + \frac{1}{\lambda_i}$.

beam and N, Φ are constants [8]:

$$\Psi(q_i, q_s) = Nexp\Big(- \frac{w_p^2}{4}|q_s + q_i|^2 \Big) sinc\Big(\frac{L\Delta k_z}{2} + \Phi \Big) \tag{17}$$

The so called Schmidt decomposition of the spatial entanglement can be found from Eq.(17): $\Psi_{12} = \sum_i \sqrt{\lambda_i}\,|u_i\rangle\,|v_i\rangle$, where $|u_i\rangle$, $|v_i\rangle$ are pure single particle states called Schmidt modes. Their derivation can be found in [9].

Hermite-Gauss $\mathcal{HG}(x, y)$ modes $|m, n\rangle = |m\rangle \otimes |n\rangle$ are an orthonormal basis of spatial modes for the 2D transverse plane that have the following normalized expression:

$$\langle x, y|\, m, n\rangle = \frac{1}{\sqrt{2^m 2^n m! n! \pi}} \mathcal{H}_m(x) e^{-\frac{x^2}{2}} \otimes \mathcal{H}_n(y) e^{-\frac{y^2}{2}}, \tag{18}$$

where $\mathcal{H}_i(x_k)$ is the Hermite polynomial of the i^{th} order for the variable x_k.

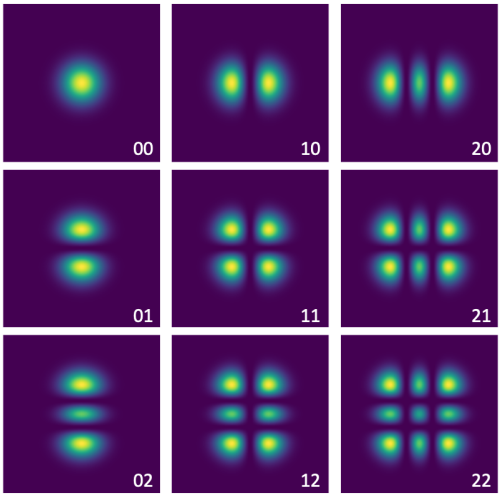

Figure 7: Hermite-Gauss (HG) modes are solutions to the paraxial wave equation. They form an orthonormal basis of the spatial functions in the Hilbert space. At any given transverse plane, the light from any beam can be decomposed into a linear combination of one of these modes. Our imaging system makes use of orthogonality of HG modes.

They represent the Schmidt modes $|u_i\rangle$, $|v_j\rangle$ of the Schmidt decomposition of the biphoton SPDC state, when it is derived in Cartesian coordinates. The decomposition can be written explicitly as:

$$|\Psi\rangle = \sum_{m,n} C_{mn} \, |m,n\rangle_s \otimes |m,n\rangle_i \, , \tag{19}$$

where the $C_{m,n}$ coefficients have the following expression:

$$C_{mn} = \frac{4\gamma}{(1+\gamma)^2} \left|\frac{1-\gamma}{1+\gamma}\right|^{(m+n)}, \tag{20}$$

and where γ is a constant that is determined by source parameters such as

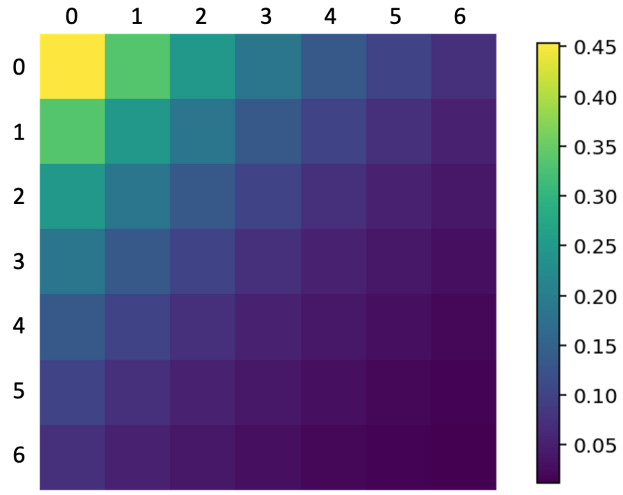

Figure 8: Plot of coefficients C_{mn} of the Schmidt decomposition of SPDC, with $\gamma = 0.15$. Columns m represent horizontal mode indices and rows n represent vertical mode indices.

crystal length L and pump beam waist w_p as $\gamma = \frac{1}{w_p}\sqrt{\frac{L}{k_p}}$. The decomposition for $\gamma = 0.15$ is shown in Fig.(8).

The Schmidt decomposition has the particularity that is provides a quantification of entanglement. Indeed, the Schmidt number $K = \frac{1}{4}(\gamma + \gamma^{-1})^2$ corresponds to the number of significant modes in the schmidt decomposition, or, the number of modes of one photon that are exactly correlated to another mode of the other photon. A biphoton state is separable when $K = 1$ and is entangled for $K > 1$. The level of entanglement increases asymptotically (in theory, but there are experimental constraints) as γ approaches 0.

1.4 Projection Method

As the choice of projection method is crucial in a mode sorting experiment; we elaborate on it briefly here. In the super-resolution setup, we chose to use the intensity flattening technique, first developed in [10], to perform the projective measurements on spatial modes. The technique has the potential to measure arbitrary spatial modes with the help of a spatial light modulator (SLM), and a single mode fiber (SMF).

SLMs are liquid crystal devices that can imprint any phase and amplitude onto an incident light beam through a screen (hologram) of precisely controlled liquid crystal pixels [11]. The orientation of the birefringent liquid crystals determines the local phase that will be added onto beam's wavefront.

Holograms are built assuming an incident plane wave beam E_r tilted at an angle with respect to the z direction of propagation. The total electric field E_t at the plane of the hologram with a desired field E_d is then: $E_t = E_r + E_d e^{-ikx}$. Thus, the diffraction pattern P represented on the hologram is the modulus squared of E_t: $P = |E_r|^2 + |E_d|^2 + E_r E_d^* e^{ikx} + E_r^* E_d e^{-ikx}$. Any light E_{in} incident on the hologram without grating is approximately modulated as:

$$E_{out} = P E_{in} \tag{21}$$

If a grating is applied to the hologram such that the pattern is modulated by an additional cyclical phase, then the modulated beam E_{out} is split into

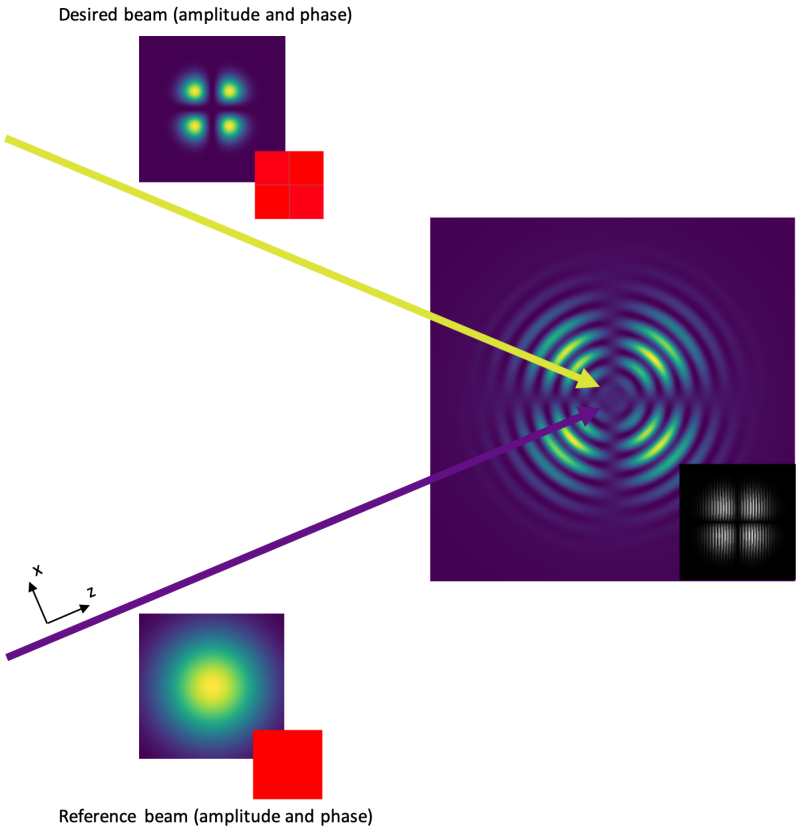

Figure 9: Diffraction pattern of a desired beam and a reference beam, used to create a hologram. The inset shows a blazed hologram generated using beam shaping technique.

orders of diffraction corresponding to different k-vectors. The desired portion of the beam is in the first order of diffraction and can be selected in the far field of the SLM or at the focus of a lens. There exist different kinds of diffraction gratings (see Fig.(10)) - the blazed grating, which uses a phase ramp, can send up to 100% of the input power to the first order of diffraction [12]. With amplitude masking however, which annuls many pixels of the hologram, the output power decreases, especially in higher modes.

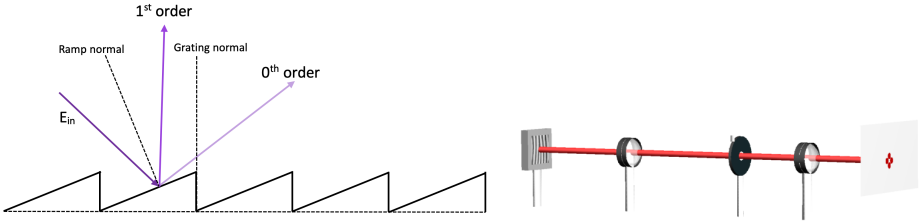

Figure 10: Generating and selecting the first order of diffraction. **Left.** Diagram of a blazed grating, and how different orders diffract off of it. **Right.** Schematics of experimental method to select the desired order of diffraction. Four optical elements are shown: from left to right hologram, lens, iris, lens.

An SLM itself cannot project onto a certain spatial mode. The intensity flattening technique relies on a SMF which couples only modes matching its fundamental mode - a Gaussian of waist σ. Recalling the orthogonality relations of $\mathcal{HG}$ modes:

$$\int\int \mathcal{HG}_{mn}(x,y)\mathcal{HG}_{kl}(x,y)dxdy = \delta_{mk}\delta_{nl}. \tag{22}$$

The action of the SLM is given by Eq.(21). Assuming an arbitrary wavefunction (for simplicity let us consider a single photon wavefunction) $\Psi(x,y) = \sum_{m,n} A_{mn}\mathcal{HG}_{mn}(x,y)$ we can write the expression of the field after selecting the first order of diffraction: $\Psi_{1st} = \sum_{m,n} A_{mn}\mathcal{HG}_{mn}P$, where in the case of a projection onto a particular $\mathcal{HG}_{kl}(x,y)$ mode $P = \mathcal{HG}^*_{kl}(x,y) = \mathcal{HG}_{kl}(x,y)$. So the field collected by the SMF is:

$$\sum_{m,n} A_{mn} \int_{-x_m}^{+x_m} \int_{-y_m}^{+y_m} \mathcal{HG}_{mn}(x,y)\mathcal{HG}_{kl}(x,y)e^{-\frac{x^2+y^2}{\sigma^2}}dxdy \neq A_{kl}. \tag{23}$$

The idea of the intensity flattening technique is to make the $e^{-\frac{x^2+y^2}{\sigma^2}} \rightarrow 1$ to retrieve the orthogonality relations. This is done by demagnifying the beam size from the SLM to the SMF, such that when considering the backwards propagating beam originating from the SMF, σ will be so large that the beam will appear flat over the hologram.

We chose a demagnification factor such that the visibility (percentage of counts attributed to diagonal elements of the crosstalk matrix with respect to total counts) should be 98%. The downside of this technique is that the losses are quite high, especially for higher order modes, and smaller projection waists on the SLM. Note that other successful super-resolution experiments have performed heterodyne detection [13, 14] instead of true projection measurements, which is much more robust to losses.

2 Super-resolution

This chapter is based on the following paper:

Grenapin, F., Paneru, D., D'Errico, A., Grillo, V., Leuchs, G., & Karimi, E. (2022). Super-resolution enhancement in bi-photon spatial mode demultiplexin. arXiv preprint arXiv:2212.10468.

2.1 Introduction to Super-resolution

2.1.1 Rayleigh's Curse

Direct imaging systems (also called image plane counting (IPC) systems), or imaging systems where the intensity is collected in the image plane of the object, are intrinsically limited in resolution due to diffraction effects [15]. In fact, any point-like source in the object plane is mapped to a larger surface in the image plane, through a function called the point spread function. The width of that point spread function (PSF) is then related to the resolution of the imaging system: if one considers two point-like sources close together in the object plane, their corresponding surfaces will overlap in the image plane, affecting the ability to resolve one point object from the other. Let us consider an imaging system consisting of a single positive lens with a circular aperture. This type of optical element is the most common in direct imaging systems. Light from a point-like source will diffract off of the lens and in the far field will exhibit Fraunhofer diffraction pattern for circular apertures. As opposed to Fresnel diffraction, the diffraction pattern observed far from an

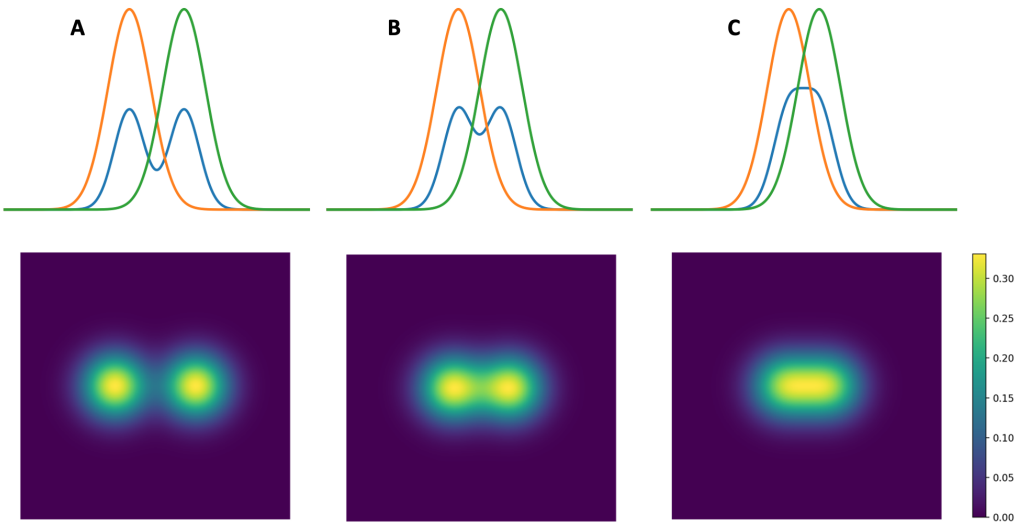

Figure 11: **Top.** Half of the total (blue) and separate (green, orange) intensities of two point sources modulated by a Gaussian PSF, for 3 different values of separation, in 1D. Rayleigh's criterion is obtained in **B**, where the maximal intensity of the combined field is about 75% of the individual peaks' maximum. **Bottom.** Total intensity of the combined field for 3 different values of separation, in 2D.

object or in the focal plane of a positive lens is given by Fraunhofer equations [16].

For circular apertures the solutions to the EM field are sinc functions, whose intensities correspond to Airy diffraction patterns with a central disk characterized by $\sin(\theta) = \frac{1.22\lambda}{D}$, where D is the diameter of the lens and λ is the wavelength of light. Since these equations apply to the far field, the beams are treated as parallel and the angle θ is such that the small angle approximation applies: $\sin(\theta) \approx \tan(\theta) \approx \frac{1.22\lambda}{D}$. So, with f the focal length of the lens, and d the radius of the brightest disk of the diffraction pattern: $\frac{d}{f} \approx \frac{1.22\lambda}{D}$.

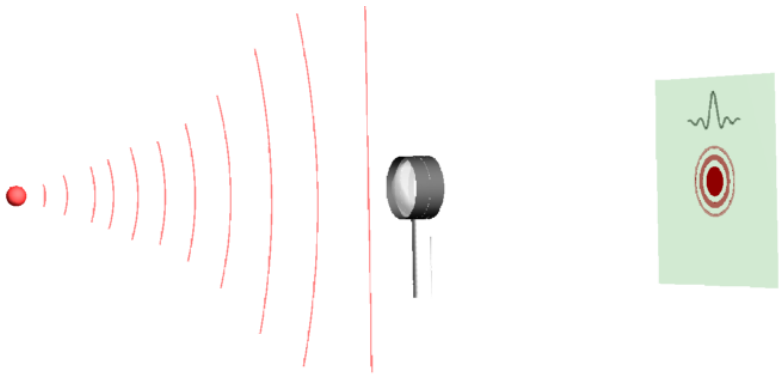

Figure 12: Conditions for Fraunhofer diffraction in far field region of the lens. The electric field in the image plane is a sinc function, which gives an Airy intensity pattern.

The width of the PSF is then related to the following equation, where R is a constant criterion (1.21 for Rayleigh or 1 for Abbe) and $\mathcal{NA} = \frac{nD}{2f}$ is the numerical aperture of the lens:

$$d = R * \frac{\lambda}{\mathcal{NA}} \tag{24}$$

The maximal value of resolution of an imaging system has thus been defined by Rayleigh's criterion, in terms of levels of distinguishability between two overlapping disks in the image plane. Imaging systems with multiple lens systems also have sinc PSFs. These are often approximated to Gaussian profiles as the central disk's intensity is mainly of importance.

2.1.2 Increasing resolution

Looking at Eq.(24) there seem to be straightforward ways to increase the resolution of a far field imaging system. Current imaging methods work around this criterion. For example. some imaging methods operate at small wavelengths, using UV or X-rays, with the drawback that for light-sensitive objects, these wavelengths pack too much energy and risk damaging the sample. Alternatively, some methods focus on increasing $\mathcal{NA}$, such as confocal imaging [17, 18] or structured illumination microscopy [19, 20]. These techniques offer modest improvements as they remain within the constraints of Rayleigh's criterion.

For that reason, near field imaging has gathered a lot of interest in past super-resolution efforts, as diffraction effects do not apply similarly in that regime. Great progress has also been made in the field of fluorescence imaging, using light-activated fluorescent molecules at precise points on the sample [21, 22]. Combined with post processing methods the resolution enhancement is significant. Additionally, imaging methods outside of optical imaging altogether such as scanning tunneling microscopes (STMs) for conductors [23], scanning electron microscopes (SEMs) [24] and atomic force microscopes (AFM) [25] have achieved resolutions exceeding the optical diffraction limit. Until Tsang's proposal [26] though, no simple far field optical imaging scheme has broken the diffraction limit. We will discuss it in detail in 2.1.4.

2.1.3 Increasing resolution in low photon regime

The ability to distinguish between two point sources is equally limited by the number of photons N collected; indeed, the signal-to-noise ratio (SNR), related to the resolution achieved during an imaging experiment, scales as $\frac{1}{\sqrt{N}}$. In low photon regimes, this criteria is the limiting factor affecting the resolution of the image.

Quantum ghost-imaging (QGI) uses the correlations between two entangled photons generated by a process called Spontaneous Parametric Down Conversion (SPDC) to produce a low noise image [27, 28]. The generated photons, conventionally named signal and idler photons, are split into two different paths. In one of the paths, the photon interacts with the object and is collected by a non-spatially resolving detector, while in the other the photon passes through a delay line and is imaged into a camera. The camera is triggered to open its shutters only when a signal photon is registered by the detector. Since the photon pair is correlated in position and momentum degrees of freedom, even though the idler photons never interacted with the object, they form an image of the object on the camera. This provides a better SNR over classical imaging as most of the ambient background light is discarded by the triggering process. Combined with interaction-free measurement [29], even higher SNR values can be attained, allowing the formation of images with on average fewer than one detected photon per pixel [30]. However, since ghost-imaging is a far field IPC method, it is limited by Rayleigh's criterion. Additionally, the maximum attainable resolution is limited by the

strength of the spatial correlations in the photon pair [31].

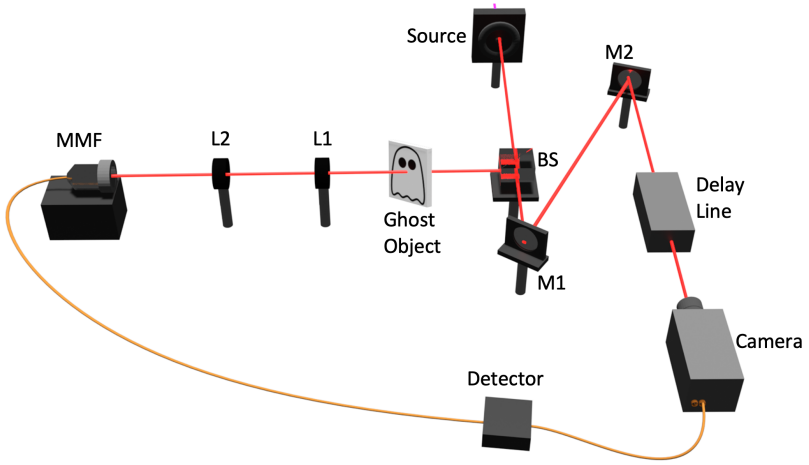

Figure 13: Experimental setup for QGI. Only key components on the set-up are shown. The entangled photon pairs are down converted at the non-linear crystal. They are split at a 50:50 beamsplitter (BS) and one photon is sent to interrogate the ghost object, the other passes through a delay line before reaching the camera - (an Intensified CCD camera that has an external triggering mechanism). The detector receives counts from the signal beam, which triggers the camera externally. MMF: multimode fibers; L1, L2: lenses; M1, M2: mirrors.

This technique also distinguishes itself by the ability to illuminate the sample with light of a different wavelength than the one sensed by the camera. Indeed, the phase matching of the SPDC process can be made so that two non-degenerate (of different wavelengths) entangled photons are produced. This is useful in situations where one wavelength is needed to illuminate the object (e.g., sensitive biological tissues) and another to obtain the spatial information (e.g., wavelength at which the detector is more sensitive).

2.1.4 Mode sorting super-resolution (SPADE)

In 2016, a finding by Tsang [26] based in quantum metrology proposed a super-resolution imaging method applicable to far-field optical imaging. The method was subsequently demonstrated and further efforts to generalize it to higher dimensions and 2D imaging applications have been investigated [32, 33, 34, 35, 36, 37]. The idea is to view the resolution of two point sources as a parameter estimation problem. Let us come back to the two point-like sources that were used to define maximal resolution criteria of far field imaging systems. Assuming a PSF $\Psi(r)$ and point sources of equal strength, we can write the EM field in the image plane as a function of the separation θ between them, and $\Psi^+(r,\theta)$, $\Psi^-(r,\theta)$ the two fields generated by the point sources. If Ψ^+ and Ψ^- are incoherent with each other, then the field in the image plane is a mixed state of both fields Eq.(25). In the coherent case, the field in the image plane is a superposition of the two Eq.(26).

$$\rho_{inc} = \frac{1}{2}\left|\Psi^+\right\rangle\left\langle\Psi^+\right| + \frac{1}{2}\left|\Psi^-\right\rangle\left\langle\Psi^-\right|, \tag{25}$$

$$\begin{cases} \left|\Psi_{coh}\right\rangle = \frac{1}{\sqrt{2}}(\left|\Psi^+\right\rangle + \left|\Psi^-\right\rangle). \\ \rho_{coh} = \left|\Psi_{coh}\right\rangle\left\langle\Psi_{coh}\right|. \end{cases} \tag{26}$$

In his initial proposal, Tsang considers an incoherent separation, although

later work has considered the coherent case as well [38, 39, 40, 41]. In this proposal, Rayleigh's curse is explained as a loss of information about θ, the distance separating the two point sources, in the intensity pattern collected in the image plane. A different kind of measurement which consists of projecting the far-field onto a spatial basis of modes is proposed, which maximizes the available information about θ.

The measure indicating how precisely the parameter θ can be extracted from a set of measurements M on a system of state ρ is given by the Fisher Information (FI):

$$\mathcal{FI} = Tr[\frac{\partial \rho}{\partial \theta} L_\rho(M)], \tag{27}$$

where $L_\rho(M)$ is the symmetric logarithmic operator defined as $\{L, p\} = 2\frac{\partial \rho}{\partial \theta}$ [42]. The lower bound on the unbiased estimation of θ, or the minimum possible variance on the value of θ extracted from the measurements, is called the Cramer Rao Lower Bound (CRLB). It goes as the inverse square root of the FI of the system: the higher the FI gathered, the more precise the estimation of θ and the more distinguishable the two point sources can be made out to be. Intensity measurement in the image plane is linked to projective measurements carried out on the 2D delta function basis $|x, y\rangle\langle x, y|$. This means that the FI about θ in typical far field imaging systems takes the form in Eq.(28), with the intensity measurement outcomes for each infinitely small

pixel $P_{xy} = \frac{1}{2}|\Psi(x+\theta/2,y)|^2 + \frac{1}{2}|\Psi(x-\theta/2,y)|^2$ obtained from Eqs.(25,13):

$$\mathcal{FI}(\theta) = \int\int \frac{1}{P_{xy}}\left(\frac{\partial P_{xy}}{\partial \theta}\right)^2 dxdy. \tag{28}$$

It is easy to show, numerically (see Fig.(14)) that the FI in Eq.(28) drops to 0 as θ approaches 0. The solution proposed by Tsang is to perform spatial mode demultiplexing (SPADE), i.e. to instead sort the light in a basis of spatial modes, chosen optimally for the PSF of the imaging system. For Gaussian PSFs, the optimal basis is the 2D Hermite-Gauss ($\mathcal{HG}$) spatial mode basis. Their definition is given in section 1.3. The FI collected in SPADE is given by:

$$\mathcal{FI}(\theta) = \sum_i \frac{1}{P_i}\left(\frac{\partial P_i}{\partial \theta}\right)^2, \tag{29}$$

with probability P_i the projection outcomes of the state ρ_{inc} onto the spatial mode $\mathcal{HG}_i$. With the correct normalization, it can be shown that the total FI collected in SPADE is a constant value $\mathcal{FI} = \frac{1}{2}$ across all separations. For small values of θ, most of the FI is contained in the first derivative modes, which has made possible schemes like binary SPADE, where only two projective measurements (onto the ground PSF state and first optimal state) are performed. In the supplemental of the manuscript, we show in a simple proof that for any PSF Ψ the optimal projection in the small separation regime is a normalized mode proportional to the derivative Ψ', which also gives a total of $\mathcal{FI} = \frac{1}{2}$. The result is groundbreaking since it means that an

arbitrarily small separation can be estimated up to a precision of $\frac{1}{\sqrt{2N}}$ with N the total number of photons.

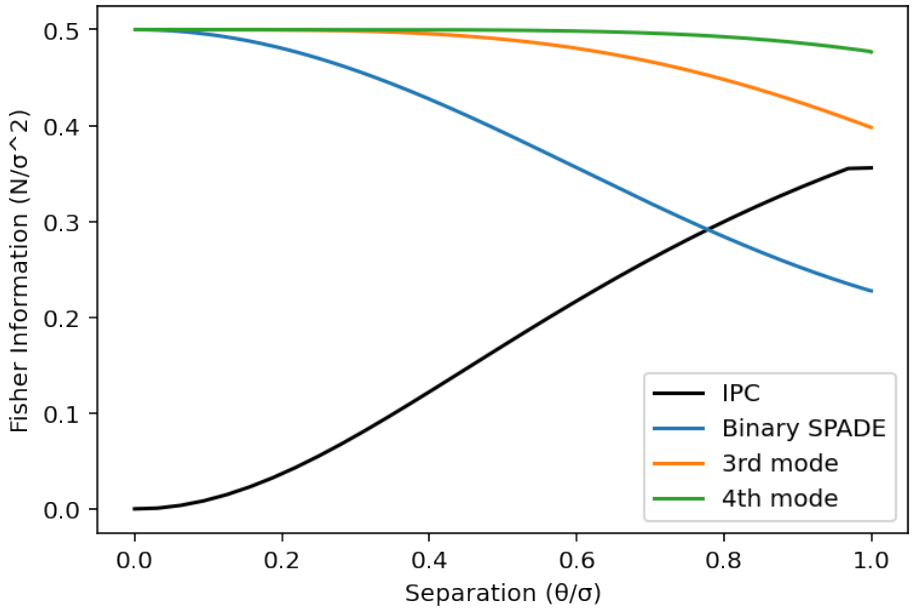

Figure 14: Fisher Information of the separation θ as a function of θ, in the IPC and SPADE methods. The curve in black is the FI curve representing Eq.(28) for direct intensity measurements. In orange, the FI curve for binary SPADE - obtained with the first two optimal measurements of SPADE. FI curves obtained by collecting information in higher modes are also shown. It is easily seen that most of the FI is captured by binary SPADE for small separations.

Calculating the fisher information for more than two point sources of arbitrary brightness and coherence quickly becomes a complex quantity to determine. Recent theoretical proofs have made progress in that direction [43]. However, generalized super-resolution with SPADE can be achieved experimentally without an explicit underlying model for the FI: 2D mode sorting

experiments using deconvolution algorithms and machine learning to recombine images from different modal outputs, have achieved super-resolution [44, 45].

2.1.5 In the presence of noise

Another limitation of the SPADE technique is its sensitivity to noise. In fact, it has been shown that for noise manifesting as crosstalk within the demultiplexing system, the resolvable distance scales as $N^{\frac{1}{4}}$, as opposed to $\sqrt{N}$ as before [46, 47], where N is the total number of photons sorted across all modes. For small values of crosstalk the advantage of SPADE remains major. To understand this effect, let us consider the projection intensities collected in the presence of noise (e.g., background noise). They take on the form $P_i^{exp} = \alpha_i + P_i^{th}$ where α represents counts collected due to noise. Hence, the FI becomes:

$$\mathcal{FI}(\theta) = \sum_i \frac{1}{\alpha + P_i} \left(\frac{\partial(\alpha + P_i)}{\partial \theta} \right)^2. \tag{30}$$

For $|m\rangle\langle m|$ an optimal measurement, P_m^{th} varies as θ^2 (see supplemental material of the manuscript). Taking the limit of Eq.(30) with $\theta \to 0$ we find once again that $\mathcal{FI}(\theta = 0) = 0$. Notice though that in Fig.(15), even while the FI is degraded in the presence of noise, there remains a range for which the information collected by SPADE is superior to the IPC method's

FI. This means that there is a number of photons N such that in that range, the separation can be super-resolved.

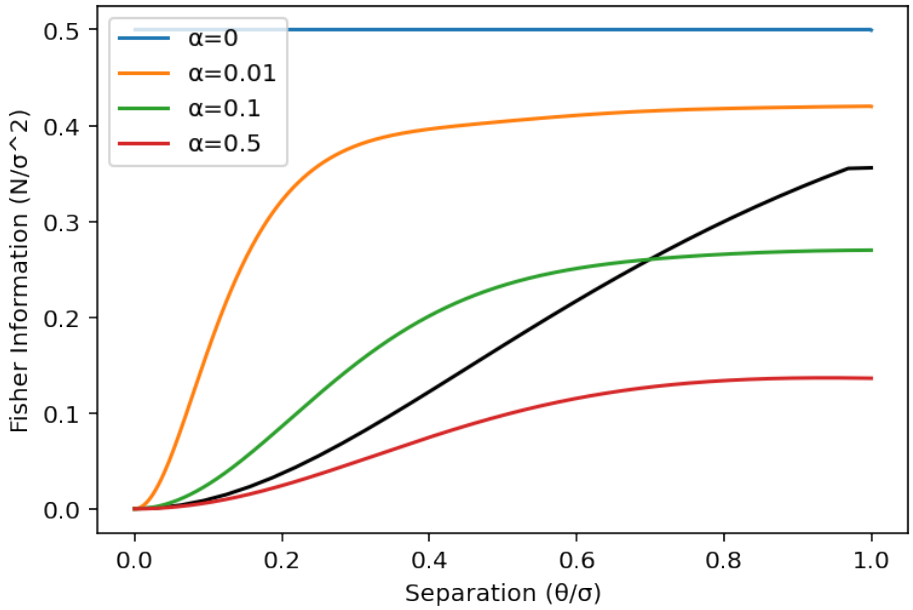

Figure 15: Fisher Information of the separation θ as a function of θ, with varying amounts of noise present in the counts. In black is the reference for the direct imaging (IPC) method, with no noise considered.

Progress has been made to considerably reduce the effect of noise by improving the detection within the demultiplexing system [13].

2.1.6 Motivation

After reviewing the previous literature, to the best of our knowledge, a far-field super-resolution technique has not been developed with entangled photon pairs. We aim to show that high-dimensional entanglement provides additional advantages to single photon mode sorting methods. Considering

the biphoton state as the imaging system's PSF, we perform the first proof of principle super-resolution experiment with SPDC light, in a modified coincidence imaging setup equipped with two separate projective measurements.

2.2 Methods

In this section, we hope to clarify the decisions that were made in the process of perfecting the technique described in the paper. We will walk through the choice of projection basis, experimental projection technique, separation tunability, and model used for the estimation.

2.2.1 Fisher Information in an entangled imaging setup

The Fisher Information associated to different available projection methods were evaluated before opting for the joint basis of $\mathcal{HG}$ modes, which we will show contains optimal information for SPDC with a diagonal Schmidt decomposition. Some of the explanations will overlap with the derivations in the supplemental materials of the manuscript.

The biphoton SPDC state can be decomposed as a tensor product of two linear combinations of Hermite-Gauss modes, as shown in Eq.(19).

In the conventional SPADE technique, only the light that has directly interacted with the object is sorted into a basis of HG modes, with a waist of the size of the PSF waist. In the biphoton imaging system at our disposition, we can equally perform this kind of SPADE technique, considering only the density matrix of a single signal photon Eq.(12) out of the pair. Instead

of choosing a projection beam waist of the size of the PSF induced by the apertures in the imaging system, we choose the beam waist of the Schmidt modes of the SPDC decomposition.

So, considering a displacement in the signal arm creating a mixed state of two paths as in Eq.(25), the single photon density matrix can be written out as:

$$\rho_s^{+,-} = \frac{1}{2}\sum_{mn} C_{mn}^2 \Big[|\langle k|\, m^+\rangle|^2 + |\langle k|\, m^-\rangle|^2 \Big]. \tag{31}$$

And the probability outcomes $\mathcal{P}_{kl}^s$ of projecting the signal photon of the entangled pair onto an element $|k,l\rangle\langle k,l|$ of the $\mathcal{HG}$ Schmidt basis can be found with Eq.(13):

$$\mathcal{P}_{kl}^s = \frac{1}{2}\sum_{m} C_{m,l}^2 \Big\{ |\langle k|\, |m^+\rangle\, |^2 + |\langle k|\, |m^-\rangle\, |^2 \Big\}. \tag{32}$$

In the small separation limit, we can approximate a displaced $\mathcal{HG}_m$ state by $|m^\pm\rangle = |m\rangle \pm \delta\, |m\rangle^{(1)}$. We use that approximation in Eq.(32) to get an idea of the behaviour of the probability outcome and $\mathcal{FI}$ in the sub-rayleigh limit:

$$\mathcal{P}_{kl}^s \approx C_{k,l}^2 + \frac{\delta^2}{2}\Big\{ (k+1)C_{k+1,l}^2 + kC_{k-1,l}^2 \Big\}. \tag{33}$$

Notice that the expression does not have a straightforward δ^2 dependence

as in the optimal SPADE method. The $\mathcal{FI}$ associated to this method is thus not constant, and succumbs to a similar effect as with direct imaging methods.

$$\mathcal{FI}_{kl} \approx \frac{2\delta^2\Big\{(k+1)C^2_{k+1,l} + kC^2_{k-1,l}\Big\}^2}{C^2_{k,l} + \delta^2\Big\{(k+1)C^2_{k+1,l} + kC^2_{k-1,l}\Big\}}. \tag{34}$$

Another possibility in the biphoton imaging setup is to use exploit both photons in the mode sorting process. In coincidence imaging, the signal photon is projected onto an element of the $\mathcal{HG}$ basis, and the correlated idler photon is imaged with a camera that opens its shutters only when triggered by the detection of a photon in the signal arm. The intensity pattern on the camera thus contains a certain amount of $\mathcal{FI}$ about the object (or separation, in our case) on the signal side. The density matrix of this particular configuration can be written as in Eq.(12), composed of two pure states $|\Psi_i\rangle = |\Psi^{\pm}\rangle$ that are the biphoton wavefunctions with, respectively, a positively and negatively displaced signal photon.

An intensity measurement is equivalent to a projection onto the 2D-delta function basis $\{|x_i, y_i\rangle\langle x_i, y_i|\}$ (assuming pixels are infinitely small) where $\langle x'_i, y'_i|\,|\Psi\rangle = \Psi(x'_i, y'_i)$. Thus, the joint basis of projection $\{|m,n\rangle_s\langle m,n|_s \otimes |x_i, y_i\rangle\langle x_i, y_i|\}$ gives projection outcomes $\mathcal{P}^{x_i,y_i}_{mn}$ for each position (x_i, y_i) on the camera:

$$\mathcal{P}^{x_i,y_i}_{kl} = \langle k,l|_s \otimes \langle x_i, y_i|\,\rho_{BI}\,|k,l\rangle_s \otimes |x_i, y_i\rangle$$

$$= \frac{1}{2}\sum_{m,m'} C_{m,l}C^{*}_{m',l}\Big\{ \langle k|\, m^{+}\rangle\big\langle m'^{+}\big|\, k\big\rangle$$

$$+ \langle k|\, m^{-}\rangle\big\langle m'^{-}\big|\, k\big\rangle\Big\}\mathcal{HG}_{m,l}(x_s,y_s)\mathcal{HG}_{m',l}(x_i,y_i). \tag{35}$$

In the small separation limit, obtained similarly as above we have the behaviours of the probability outcome and $\mathcal{FI}$ in the sub-rayleigh range, where SPADE should outperform direct imaging:

$$\mathcal{P}^{x_i,y_i}_{kl} = C^2_{k,l}\mathcal{HG}^2_{k,l}(x_i,y_i) + \delta^2\Big\{\mathcal{A}^2_{+1} + \mathcal{A}^2_{-1} - 2\mathcal{A}_{+1}\mathcal{A}_{-1}\Big\}, \tag{36}$$

$$\begin{cases} \mathcal{A}_{+1} = \sqrt{\frac{k+1}{2}}C_{k+1,l}HG_{k+1,l}(x_i,y_i). \\ \mathcal{A}_{-1} = \sqrt{\frac{k}{2}}C_{k-1,l}HG_{k-1,l}(x_i,y_i). \end{cases}$$

Again, notice that the expression does not have a straightforward δ^2 dependence as in the optimal SPADE method. The $\mathcal{FI}$ is not constant and has a similar behaviour as the single photon case above, i.e.,

$$\mathcal{FI}^{x_i,y_i}_{kl} = \frac{4\delta^2\Big\{\mathcal{A}^2_{+1} + \mathcal{A}^2_{-1} - 2\mathcal{A}_{+1}\mathcal{A}_{-1}\Big\}^2}{C^2_{k,l}\mathcal{HG}^2_{k,l}(x_i,y_i) + \delta^2\Big\{\mathcal{A}^2_{+1} + \mathcal{A}^2_{-1} - 2\mathcal{A}_{+1}\mathcal{A}_{-1}\Big\}}. \tag{37}$$

In both methods considered above, the $\mathcal{FI}$ falls to 0 as the separation approaches 0. There may still be a range in which these methods surpass direct imaging, but not with the same strength as conventional SPADE does for conventional far field imaging systems.

Instead of performing an intensity measurement on the idler side, we choose to perform another projective measurement onto the $\mathcal{HG}$ mode basis and consider only the joint outcomes from this process; this method is also called collecting coincidence counts. The density matrix considered is the same as for coincidence imaging, but the basis elements are different: $|k,l\rangle_s\langle k,l|_s \otimes |k',l'\rangle_i\langle k',l'|_i$. Many terms are thus eliminated from the summations:

$$\mathcal{P}_{kl}^{k'l'} = \frac{1}{2}C_{k',l}^2\Big\{|\langle k\,|k'^{+}\rangle|^2 + |\langle k\,|k'^{-}\rangle|^2\Big\}\delta_{l,l'}. \tag{38}$$

The behaviour for small separations is given by:

$$\mathcal{P}_{kl}^{k'l'} \approx C_{k',l}^2\left[\delta_{k,k'}^2\big\{1-\frac{s^2}{2}(2k'+1)\big\} + \delta_{k,k'-1}^2\frac{k'}{2} + \delta_{k,k'+1}^2\frac{k'+1}{2}\right]\delta_{l,l'}^2,$$

$$\begin{cases} \mathcal{P}_{kl}^{kl} \approx C_{k,l}^2(1-\frac{s^2}{2}(2k+1)). \\ \mathcal{P}_{kl}^{k+1,l} \approx s^2C_{k+1,l}^2\frac{k+1}{2}. \\ \mathcal{P}_{kl}^{k-1,l} \approx s^2C_{k-1,l}^2\frac{k}{2}. \end{cases} \tag{39}$$

For modes on the diagonal ($k=k'$) the $\mathcal{FI}$ again does not have the straightforward δ^2 dependence. However, for slightly off-diagonal modes ($k=k'\pm1$) the projection outcome has the same form as for optimal measurements,

where $\mathcal{P}_i$ is proportional to δ^2,

$$\begin{cases} \mathcal{FI}_{kl}^{kl}(s) \approx \frac{\left[C_{k,l}^2(2k+1)s\right]^2}{4-2s^2(2k+1)} \to 0. \\ \mathcal{FI}_{kl}^{k+1,l} \approx \frac{k+1}{2} C_{k+1,l}^2. \\ \mathcal{FI}_{kl}^{k-1,l} \approx \frac{k}{2} C_{k-1,l}^2. \end{cases} \tag{40}$$

The $\mathcal{FI}$ does not vanish for off-diagonal modes of the joint basis of projection. In fact, the sum of the $\mathcal{FI}$ contained in all the off-diagonal modes is equal to $\frac{1}{2}\sqrt{K}$ (see supplemental materials of the manuscript). This indicates that for any level of entanglement ($K \leqslant 1$), the biphoton SPADE technique just described surpasses conventional SPADE. For this reason, and because mode sorting super-resolution with entangled photons has not been yet explored, we opted for this method and carried out a proof of principle experiment, detailed in the manuscript.

2.2.2 Introducing a separation

For the sake of clarity about the experimental setup, in this subsection we go over the method chosen to achieve a mixed state of separated beams. There are a couple ways of introducing a transverse incoherent separation in a beam. In this experiment it is important to have very precise control over the separation, for a range of separations varying from 0 to a couple beam waists. The incoherent separation is introduced between H and V polarization components of the signal beam via an unbalanced Mach-Zender

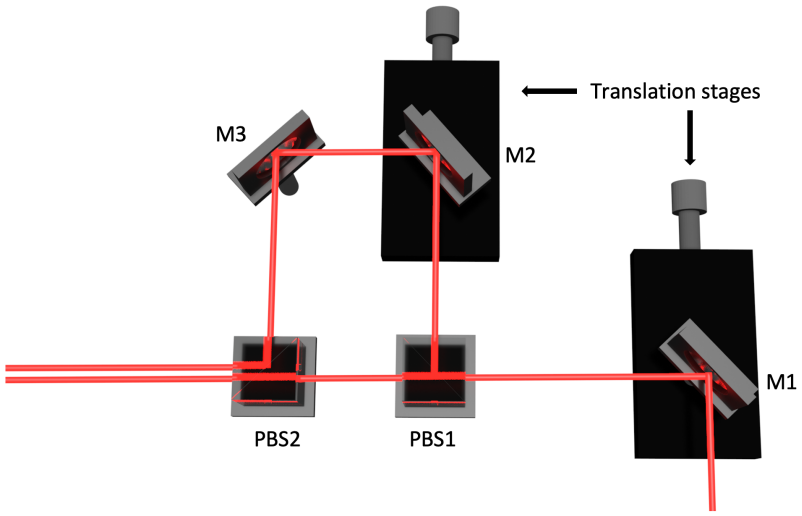

Figure 16: Unbalanced MZI used to produce a symmetric incoherent separation to test the biphoton SPADE technique. The mirror on the right of the MZI M1 can be shifted vertically, which shifts the position of both H and V polarization components exiting the MZI. To compensate, M2 in the unbalanced arm is also placed on a translation stage to control the V polarization component, which re-establishes a symmetry about the center of the undisplaced beam.

interferometer (MZI), of which two mirrors are placed on translation stages. Both stages are shifted by values that have been previously calibrated to generate a tunable separation that is symmetric with respect to the center of the undisplaced signal beam (see Fig.(16)).

A half waveplate at 22.5° is placed before the MZI to rotate the horizontal polarization of the downconverted light into equal parts of H and V. Since the SLM only converts H input polarization components into V polarization in the first order of diffraction, another half waveplate at 22.5° is placed between the interferometer and the SLM. That way, half of both separated beams

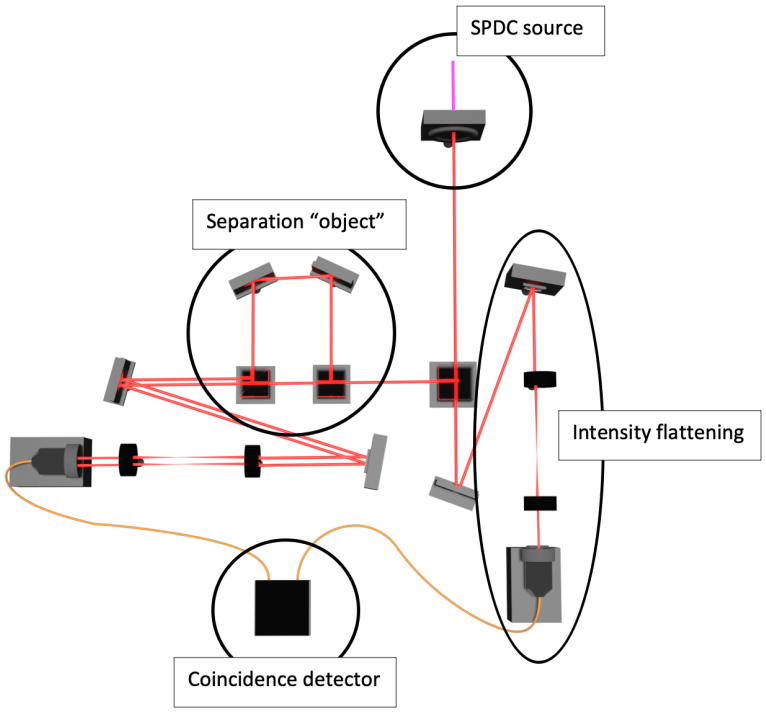

Figure 17: Experimental setup for the biphoton SPADE technique. Only key components on the set-up are shown, and the specific functions of different sections of the setup are labeled. The entangled photon pairs are generated at the SPDC crystal source, and are split at a 50:50 beamsplitter. The signal photon is sent to an interferometer where an incoherent separation is introduced into the beam. It is then projected onto a HG mode via the intensity flattening technique. The idler photon goes through another intensity flattening technique in the opposite arm of the setup. Counts collected on both ends are sent to a coincidence box which registers the simultaneous detections.

will undergo the projection onto $\mathcal{HG}$ modes. The second half is discarded, which is another source of loss in this technique. Furthermore, the MZI is unbalanced to ensure that the path difference between both separated beams is much larger than the coherence length of the downconverted light. This

insures that in the section of the setup between the SLM and the SMF when both separated beams have vertical polarization, the EM field remains a mixed state of the two.

2.2.3 Estimation

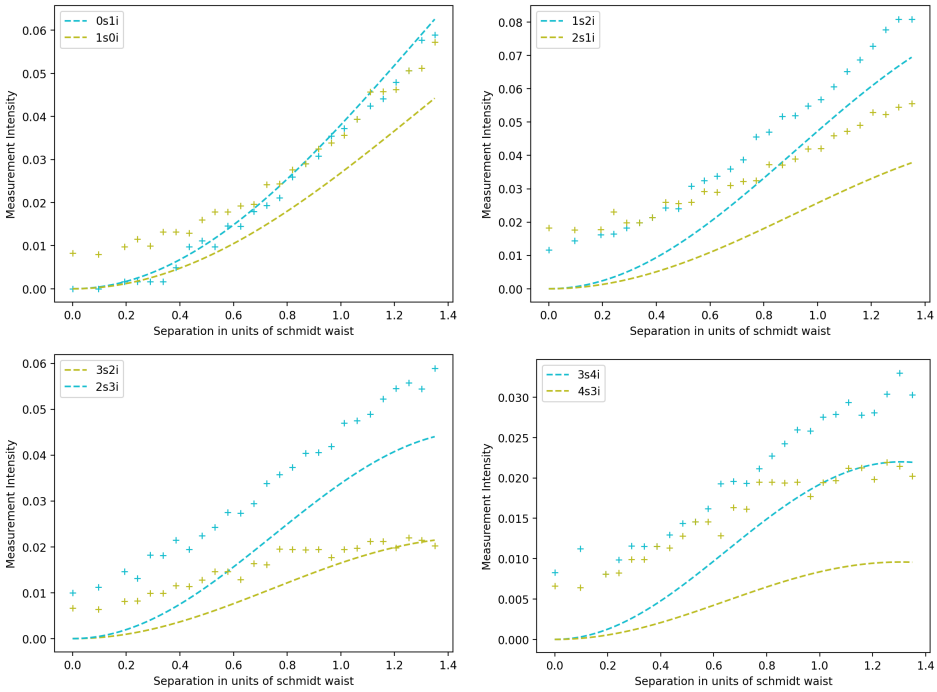

Figure 18: Experimental data versus no-noise model probabilities, for projections onto optimal modes. n_i, m_s in the legend represent the joint projection measurement of idler photon onto $\mathcal{HG}_n$ and signal photon onto $\mathcal{HG}_m$. The experimental data is offset by some noise, most likely modal cross-talk, attenuation, and dark counts.

In this subsection we elaborate on the choice of model for the final estimation of the separation. Data was collected in the form of 7x7 crosstalk matrices (with $n, n' = 0$ and m, m' varying from 0 to 6) of coincidence counts accu-

mulated for 60s for each lateral separation applied to the signal beam. The separation ranged from 0 to $1.35\sigma_s$ in increments of $0.0465\sigma_s$, and in total $N = 37000$ photons were collected. Recall that the lower bound of the error on the unbiased estimation of the separation goes as $\frac{1}{\sqrt{N\mathcal{F}\mathcal{I}}}$. For the estimation, we applied a Maximum Likelihood Estimation procedure (MLE) for each separation recorded experimentally, which consists of maximizing the likelihood function $L(s) := \left(\frac{N!}{\prod nij!}\right) \prod_{ij} P_{ij}(s)^{n_{ij}}$, where n_{ij} are the experimental counts for joint projections onto $\mathcal{HG}_{i0}(x, y)$ on the signal photon and $\mathcal{HG}_{j0}(x, y)$ on the idler photon, and $P_{ij}(s)$ is the model's theoretical value for a separation s. The function is maximized when the value of s most closely matches the experimental counts. Using the theoretical model in which the SPDC light is perfectly diagonal, the MLE method did not yield accurate estimation outcomes, as the experimental counts suffered from cross-talk due to noise in the optimal modes, which makes the estimation biased, and the error on the estimation much higher than the CRLB. The results of this estimation are shown in the manuscript.

At first we tried to explain the noise with a non-diagonal Schmidt decomposition model of SPDC. Instead of assuming a biphoton wavefunction as in Eq.(19), we have a decomposition in a different basis of spatial $\mathcal{HG}$ modes where the $C_{mn}^{m'n'}$ coefficients are not nul for $m, n \neq m'n'$:

$$|\Psi\rangle_{BI} = \sum_{m,n} \sum_{m',n'} C_{m,m'}^{n,n'} |m, n\rangle_s \otimes |m', n'\rangle_i . \tag{41}$$

The idea is that perhaps the projection was performed onto a $\mathcal{HG}$ basis with a waist slightly different from the Schmidt waist. The resulting cross-talk matrix would be distributed a bit more across the non-diagonal modes. The density matrix for such a state is represented as $\rho_{BI} = |\Psi\rangle\langle\Psi|$. Introducing a separation δ to the signal arm, the state becomes mixed as seen previously in Eq.(25):

$$\rho_{BI} = \frac{1}{2}\sum_{m,n}\sum_{m',n'}\sum_{p,q}\sum_{p',q'} C^{n,n'}_{m,m'}C^{q,q'}_{p,p'}\Big[\,|m^+\rangle\langle p^+| + |m^-\rangle\langle p^-|\,\Big]\,|n\rangle\langle q| \otimes |m',n'\rangle\langle p',q'| \tag{42}$$

Projecting on an element $|k,l\rangle_{s\,s}\langle k,l| \otimes |k',l'\rangle_{i\,i}\langle k',l'|$ of the joint basis of projection, $\mathcal{P}^{k'l'}_{kl}$ takes the new form:

$$\begin{aligned}\mathcal{P}^{k'l'}_{kl} &= \frac{1}{2}\sum_{m,p} C^{l,l'}_{m,k'}C^{l,l'}_{p,k'}\Big\{\langle k|\,m^+\rangle\langle p^+|\,k\rangle + \langle k|\,m^-\rangle\langle p^-|\,k\rangle\Big\} \\ &= \frac{1}{2}|\sum_{m} C^{l,l'}_{m,k'}\langle k|\,m^+\rangle|^2 + \frac{1}{2}|\sum_{m} C^{l,l'}_{m,k'}\langle k|\,m^-\rangle|^2 \end{aligned} \tag{43}$$

The non-diagonal theoretical model, see Fig.(19), is not better suited to explain the discrepancies between the model and experimental counts, which would indicate that the noise is generated through a different mechanism. As a result, we chose to fit the counts linearly as a function of the theoretical probabilities. We can think of this fitting as a calibration of the imaging system, which would be performed before taking sets of data. Note that

the CRLB, or error on the estimation itself, was not calculated as part of the experiment since only one set of 7x7 cross-talk matrices were collected for each separation. From the FI obtained and the total number of photon counts N collected, we were able to simulate the precision attained by this technique in the conditions of noise of this experiment, which is roughly one order of magnitude higher than direct imaging with a Gaussian of Schmidt waist.

2.3 Publication

Super-resolution enhancement in bi-photon spatial mode demultiplexing

Florence Grenapin,[1] Dilip Paneru,[1] Alessio D'Errico,[1] Vincenzo Grillo,[2] Gerd Leuchs,[1,3] and Ebrahim Karimi[1,3]

[1] *Nexus for Quantum Technologies, University of Ottawa, Ottawa, K1N 6N5, ON, Canada*
[2] *Istituto Nanoscienze, Consiglio Nazionale delle Ricerche, Via G. Campi 213/A, 41125 Modena, Italy*
[3] *Max Planck Institute for the Science of Light, 91058 Erlangen, Germany*

Imaging systems measuring intensity in the far field succumb to Rayleigh's curse, a resolution limitation dictated by the finite aperture of the optical system. Many proof-of-principle and some two-dimensional imaging experiments have shown that, by using spatial mode demultiplexing (SPADE), the field information collected is maximal, and thus, the resolution increases beyond the Rayleigh criterion. Hitherto, the SPADE approaches are based on resolving the lateral splitting of a Gaussian wavefunction. Here, we consider the case in which the light field originates from a bi-photon source, i.e. spontaneous parametric down-conversion, and a horizontal separation is introduced in one of the two photons. We show that a separation induced in the signal photon arm can be super-resolved using coincidence measurements after projecting both photons on Hermite-Gauss modes. Remarkably the Fisher information associated with the measurement is enhanced compared to the ordinary SPADE techniques by $\sqrt{K}$, where K is the Schmidt number of the two-photon state that quantifies the amount of spatial entanglement between the two photons.

INTRODUCTION

The resolution of far-field optical imaging systems based on direct intensity measurements is limited by the Point Spread Function (PSF), a diffraction phenomenon dictated by light wavelength and aperture width of the optics involved [1]. The accuracy of this measurement diverges for small separations of two-point sources; an effect also referred to as "Rayleigh's curse". The discovery of this phenomenon has encouraged research efforts in other fields of imaging, such as near field imaging [2, 3] or imaging based on electronic effects [4, 5], which goes beyond the optical Rayleigh limit. In 2016, Tsang and his colleagues proposed a simple spatial mode demultiplexing (SPADE) scheme, which is robust to the resolution curse [6]. It shows that our ability to estimate a separation between two incoherent point sources collapses as the separation approaches zero when using conventional intensity measurements, thus assimilating Rayleigh's curse to an intrinsic loss of Fisher information at small separations. The SPADE scheme proposed uses spatial mode sorting, with mode projections tailored to the PSF of the imaging system, which collects maximal Fisher information regardless of the separation magnitude. This has prompted many further theoretical and experimental findings in recent years, exploring applications and modifications of SPADE for different imaging systems [7–10], coherent point sources [11–13], limitations in the presence of cross-talk or other noise sources [14–16], and even extensions to higher-dimensional objects [17, 18]. Although the explicit model estimating all points of an arbitrary two-dimensional (2D) object is vastly complicated to derive in terms of Fisher information, 2D imaging simulations [19] and experiments [20] using post-processing algorithms (deconvolution, Machine Learning) have shown an increase in resolution beyond the Rayleigh limit. This solidifies the intuition relating the distinguishability of two-point sources to the overall resolution of a 2D imaging system.

The main idea behind SPADE is to estimate the separation between two-point sources by looking at the alteration of the field's phase, in particular, at the change in phase symmetry, which can be efficiently probed by the Hermite-Gauss (HG) decomposition for the usual Gaussian PSF. In this work, we address the following question: *Can the spatial correlations emerging from two-photon sources enhance the resolution sensitivity?* We show that it is possible to super-resolve a separation using mode-sorting in coincidence measurements with a PSF that is itself entangled in the form of SPDC light. More specifically, we consider a two-photon wavefunction which allows a Schmidt decomposition in HG modes, with Schmidt number K. An incoherent displacement, which mimics the effect of a transmitting sample, is applied on one of the two photons, and the displacement is estimated by projecting the resulting state on direct products of HG modes. We note that the somewhat related inverse problem of generating a spatially or temporally shaped pure photon state in one beam of an entangled pair (ghost interference) likewise requires the projection on pure states in the other beam of the entangled pair [21]. Our main result shows that the Fisher information, whose inverse gives a lower bound on the estimation error, scales as $\sqrt{K}/2$, where $K = 1$ corresponds to the separable case of a Gaussian point spread function. Hence any spatially entangled two-photon source provides an advantage with respect to the ordinary SPADE. Here, we derive this result and present a first proof-of-principle experimental implementation. We will conclude by discussing the possible settings in which the two-photon SPADE can give a practical advantage.

THEORY

To understand the resolution limits of a given experimental technique, one must evaluate the lower bound on the achievable uncertainty of the estimator δ (which, in our case, is the lateral displacement). This limit is given by the Cramer-Rao bound [6, 22]: the estimator's standard error is lower bounded by the inverse of the Fisher information $\Delta\delta \geq 1/\sqrt{n\,\mathcal{FI}}$ [23, 24], where n corresponds to the number of repeated measurements and the Fisher information, $\mathcal{FI}$, can be calculated from the probabilities $\mathcal{P}_j$ of a given measurement outcome j as $\mathcal{FI} = \sum_j \frac{1}{\mathcal{P}_j}\left(\frac{\partial \mathcal{P}_j}{\partial \delta}\right)^2$. In the following, we consider the problem of resolving an incoherent transverse displacement of a photon which is in a spatially correlated state with another idler photon. We will calculate the Fisher information for a bi-photon spatial mode demultiplexing scheme and compare the result with the classical SPADE, which emerges from the uncorrelated limit of our scenario.

In a typical imaging setup, the image plane of a point source is described by a two-dimensional PSF $\Psi(\mathbf{r})$ (with $\mathbf{r} = (x, y)$). In the case of two incoherent point sources separated horizontally by a distance s, the wavefunction in the image plane can be described by the mixed state: $\rho = \frac{1}{2}\left(|\Psi^+\rangle\langle\Psi^+| + |\Psi^-\rangle\langle\Psi^-|\right)$, where $\langle \mathrm{x}|\,\Psi^\pm\rangle := \Psi(x \pm \frac{s}{2}, y)$. An intensity measurement, which corresponds to a projective measurement in the position bases, results in the outcomes with a distribution, $I(x,y) = \frac{1}{2}\left(|\Psi^+|^2 + |\Psi^-|^2\right)$. The Fisher information for the direct imaging method is known to rapidly fall to zero for separations smaller than the width of the point spread function [6]. However, by mode sorting using modes that form orthogonal bases for the space containing the PSF (SPADE), the total FI remains constant across all values of s [6]. Optimal bases are ones in which most of the FI for small s is captured in the first couple of measurements, making schemes like binary SPADE [10] simple and attractive. We show in the Supplementary Material Section S1 how a projection on the derivative of the PSF with respect to the coordinate associated with the direction of the displacement is an optimal projection for the small separation regime. More rigorous ways to determine optimal measurement bases have been developed [7].

In a coincidence imaging setup with entangled SPDC photon pairs, there is no pure wavefunction describing one of the single photons' quantum states. The single particle state is maximally mixed, which can mimic a Gaussian in its intensity pattern when viewed on the camera. The pure state describing the entangled particles is a bi-photon state of signal and idler which can be expressed in the Schmidt basis of Hermite-Gauss (HG) modes [25]:

$$|\Psi\rangle = \sum_{m,n} C_{mn}\,|m,n\rangle_s \otimes |m,n\rangle_i\,, \tag{1}$$

where the C_{mn} coefficients are the Schmidt coefficients of the HG decomposition and $|m,n\rangle$ states are the 2D HG modes of order (m,n) with a beam waist parameter σ_s: $\langle x,y|\,m,n\rangle := \mathrm{HG}_{m,n}(x,y) = \mathcal{N}\exp(-(x^2+y^2)/\sigma_s^2)\,\mathrm{H}_m(\sqrt{2}x/\sigma_s)\,\mathrm{H}_n(\sqrt{2}y/\sigma_s)$, where $\mathrm{H}_m(x)$ are Hermite polynomials and $\mathcal{N}$ a normalization constant. In this basis, the correlations are diagonal: a signal photon in a particular $|i,j\rangle$ mode is entangled with an idler photon in that exact mode (see the Supplementary Material Section S2). In practice, any action occurring on one photon, such as the typical diffraction causing PSFs, is also reflected in the bi-photon wavefunction. The Schmidt coefficients can be given an analytical expression (see [26, 27]): $C_{m,n} = |(\gamma+1)/(\gamma+1)|^{m+n} 4\gamma/(1+\gamma)^2$, where $\gamma = \frac{1}{\sigma_p}\sqrt{\frac{L\lambda_p}{2\pi}}$ is a parameter defined by crystal length L, pump beam waist σ_p and wavelength λ_p. Here, we investigate how two-photon SPADE allows us to super-resolve separation introduced in one of the photon paths as if the PSF was of the form of the source (just as in [9, 10]) – which is the bi-photon wavefunction described above.

Finding the optimal basis of projection for SPADE is not as straightforward as in the single photon PSF cases. Although the derivative of the bi-photon PSF with respect to the signal photon's coordinates can be calculated directly (Supplementary Material Section S2), this is a nonseparable state for which it is challenging to devise a single-shot projector experimentally. However, we note that interesting progress is being made in that direction [28]). Instead, as in ordinary SPADE, we consider the projection on the basis of direct products of HG modes $\{|m,n\rangle_s\langle m,n| \otimes |m,n\rangle_i\langle m,n|\}$. The expression for a projection onto mode $\mathrm{HG}_{k,l}(x_i,y_i)$ in idler and $\mathrm{HG}_{k',l'}(x_s,y_s)$ in signal can be derived as,

$${}^{k',l'}_{k,l}\mathcal{P}_{coinc} = \frac{1}{2}C^2_{k',l}\delta_{l,l'}\sum_{\pm}|\,\langle k|\,k'^{\pm}\rangle|^2. \tag{2}$$

With $s = 0$ the correlations are diagonal: only projections where $k = k'$ have non-zero outcomes. As s increases, contributions from the first off-diagonal modes appear. Equation (2) can be given an analytical expression using the result: $\langle m|\,n^\pm\rangle = \sqrt{\frac{m!}{n!}}2^{\frac{m-n}{2}}(\pm s)^{n-m}e^{-\frac{s^2}{4}}\mathcal{L}_m^{n-m}(\frac{s^2}{2})$, where $\mathcal{L}_i^\alpha$ is the generalized Laguerre polynomial of order i, α, $n \geq m$ (see Supplementary Material Section S3 for the derivation).

For small values of s, we consider the expansion of ${}^{k',l'}_{k,l}\mathcal{P}_{coinc}$ to the order of s^2 by substituting $|m^\pm\rangle = |m\rangle \pm \frac{s}{2}|m\rangle' + O(\frac{s^2}{4})$ into Eq. (2). The result $\mathcal{P}_{kl}^{k'l'} \approx$

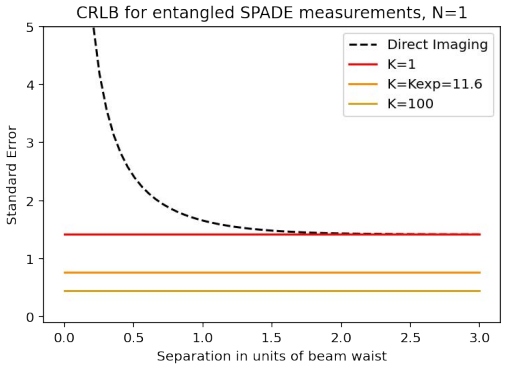

Figure 1. Classical SPADE measurements (lower bounded by $K = 1$) attain the SQL precision. Higher values of entanglement provide an advantage over classical SPADE.

$C^2_{k',l}\left[\delta_{k,k'}\left\{1-\frac{s^2}{2}(2k'+1)\right\}+\delta_{k,k'-1}\frac{k'}{2}+\delta_{k,k'+1}\frac{k'+1}{2}\right]\delta_{l,l'}$ implies that for each mode k considered in the signal beam, only the neighbouring k' modes give nonzero coincidence counts: $\mathcal{P}^{kl}_{kl} \approx C^2_{k,l}(1-\frac{s^2}{2}(2k+1))$, $\mathcal{P}^{k+1,l}_{kl} \approx s^2 C^2_{k+1,l}\frac{k+1}{2}$, $\mathcal{P}^{k-1,l}_{kl} \approx s^2 C^2_{k-1,l}\frac{k}{2}$. Of these terms, only the $k = k', k' \pm 1$ modes varying quadratically with the separation will translate to a nonzero FI in the small separation regime, $s \to 0$ (see Supplementary Material Section S4):

$$\begin{cases} \mathcal{FI}^{kl}_{kl}(s) \approx \frac{\left[C^2_{k,l}(2k+1)s\right]^2}{4-2s^2(2k+1)} \to 0 \\ {}^{k+1}_{k}\mathcal{FI}_{coinc} = \frac{1}{2}(k+1)C^2_{k+1,l} \\ {}^{k-1}_{k}\mathcal{FI}_{coinc} = \frac{1}{2}kC^2_{k-1,l} \end{cases}. \tag{3}$$

Since the FI in these particular projections is independent of the separation s, the variance of our separation estimates does not suffer from the so-called Rayleigh's curse, similar to the SPADE technique for a single photon.

The total Fisher Information can then be obtained by summing the individual contributions from all of the detected modes. Interestingly, for small values of s, the total has an upper bound dictated by the strength of the spatial correlation between the photon pair. More precisely,

$${}^{tot}_{2D}\mathcal{FI}_{coinc} = \gamma + \gamma^{-1} = \frac{\sqrt{K}}{2} \geq \frac{1}{2}, \tag{4}$$

where $K = \frac{1}{4}(\gamma + \frac{1}{\gamma})^2$ is the Schmidt rank often used to quantify the strength of bipartite entanglement (see Supplementary Material Section S2 for the derivation). This leads to a corresponding lower bound in the achievable precision as,

$$\Delta\hat{s}^2 \geq \frac{2}{\sqrt{K}}, \tag{5}$$

where $\Delta\hat{s}^2$ is the variance in the separation estimates. The result suggests that the precision in the measurement of near-zero separations is limited only by the strength of the spatial correlations, thereby suggesting high dimensional entanglement as a promising resource for super-resolution measurements. Not only does the method circumvent the so-called "Rayleigh curse" like the ordinary SPADE (which is bounded by the special case of $K = 1$, see Fig. 1), but it also offers further enhancement proportionate to the correlations in the system. In what follows, we describe in detail an experimental implementation and results of the method outlined above, along with some simulation results.

METHODS

For the purpose of a simpler experimental implementation in the laboratory, we considered a smaller subspace spanned by modes with $l = 0$, (i.e. $\mathrm{HG}_{00}, \mathrm{HG}_{01}, \mathrm{HG}_{02}, \ldots, \mathrm{HG}_{0n}$) for both the signal and idler photons. The total Fisher information associated with this set of joint projective measurements can be written as (see Supplementary Material Section S4),

$${}^{tot}_{1D}\mathcal{FI}_{coinc} = \frac{1}{2} + \frac{1}{2}\left(\frac{1-\gamma}{1+\gamma}\right)^2. \tag{6}$$

Experimentally, we reconstructed the correlation matrices in the Hermite Gauss (HG) basis, for a bi-photon state generated via spontaneous parametric downconversion (SPDC), for different traverse separations. The separation was then inferred from the observed correlation matrices using Maximum Likelihood Estimation.

Experimental Realization: The downconverted photon pairs are generated by pumping a 0.5-mm-thick type-I Barium Borate crystal (BBO) with a 200-mW 405-nm pump beam obtained from the Second Harmonic Generation (SHG) of a 1-GHz 100-fs laser beam. The pump beam is focused to a waist of $\sigma_p = 40$ μm at the BBO crystal, which sets a value of $\gamma = 0.15$. The value of γ determines the waist of the Schmidt modes, the Schmidt coefficients in the Hermite Gauss basis, and the Schmidt rank K [27, 29]. The generated photon pairs are then split into two paths by a 50:50 beamsplitter (BS), and the signal photon travels through an asymmetrical Mach-Zender Interferometer (MZI), which introduces a transverse separation between the Horizontal (H), and the Vertical (V) polarization components of the beam. Two mirrors are placed on translation stages,

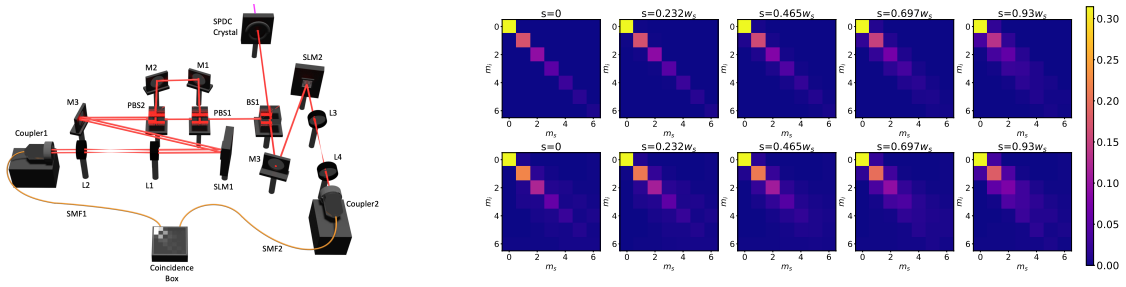

(a) Experimental Setup

(b) Theoretical (top) and Experimental (bottom) correlation matrices

Figure 2. a) A 405 nm laser shines a 1-mm type I BBO crystal generating degenerate downconverted photon pairs. Idler and signal photon are separated by a 50:50 beam splitter (BS). An unbalanced MZI interferometer implements an incoherent lateral displacement on the signal photon. The two photons are then projected on HG modes by coupling to single mode fibers (SMF) after being spatially modified by holograms displayed on spatial light modulators (SLM1 and SLM2). The photons are then detected by a pair of single photon avalanche diode (SPAD) detectors then the coincidence events are detected via a coincidence counting module. Legend: BS = Beam Splitter; PBS = Polarizing Beam Splitter; M = Mirror; SLM = Spatial Light Modulator; L= Lens; SMF = Single Mode Fiber. b)Theoretical (top) and Experimental (bottom) cross-talk matrices showing coincidence counts for first the 7x7 joint projections on signal and idler photons, for 5 different values of separation s between 0 and $0.93\sigma_s$. We can see the off-diagonal coefficients becoming more prominent as the separation increases.

specific combinations of which allow us to generate a tunable symmetric separation about the centre of the undisplaced beam. The MZI also ensures that a path difference of $\approx$ 20cm exists between the horizontal (H) and the vertical (V) polarization components, which ensures that we have two incoherent point sources. In each of the signal and the idler arms, projections onto the spatial Schmidt modes are realized via the amplitude flattening technique [30, 31], whereby a combination of appropriate holograms displayed in Spatial Light Modulators (SLM) along with suitable demagnification to the fibre plane approximates the ideal projective measurement for a particular spatial mode. The first order of the diffracted light is selected with a pinhole and coupled into a single mode fibre (SMF) after being filtered by bandpass filters (810 ± 5) nm to ensure the collection of degenerate pairs. Each SMF is then connected to a Single Photon Avalanche Diode (SPAD) detectors (Excelitas SPCM-AQRH-14-FC), and coincidence counts are registered via a time-correlated single photon counting system. Further details on the experimental setup with the essential components are illustrated in Fig. 2.

To determine the experimental Schmidt waist, multiple sets of data for differing waists of projection were taken for a zero displacement, and the experimental projection waist was chosen so as to have as close to a diagonal density matrix as possible. For each applied separation, the setup was realigned so that the centre of the displaced beam was coupled to the fibre. The coincidence counts in the diagonal modes for zero separation account for at least 82% of the total counts in the 7×7 cross-talk matrix. The deviation from a perfectly diagonal decomposition can be attributed to several factors, including a deviation of the pump beam shape from a Gaussian mode and modal cross-talk in the detection scheme. These factors can be tackled, in principle, by improved control of the pump shape (e.g. through spatial filtering or the use of SLMs) and the use of other detection schemes, respectively. Indeed, the recent advances in spatial mode sorting through multi-plane converters allow, in principle, a lossless and low cross-talk detection scheme [32].

Results

We applied evenly spaced lateral displacements at increments of $0.0465\,\sigma_s$, from $s = 0$ to $s = 1.35\,\sigma_s$, and recorded the outcomes of the joint measurements onto modes HG_{n_i,m_i} in the idler arm and HG_{n_s,m_s} in the signal arm for $n_{i/s} = 0$, and $m_{i/s} = 0, 1, \ldots, 6$. Each set of data is then a 7×7 matrix containing 49 joint projection outcomes, the coincidence counts for each of which were accumulated for up to 60s. The 7×7 matrix sums were normalized to account for laser intensity fluctuations. For such small separations, to a very good approximation, it can be safely assumed that almost all of the generated photons are in the 7×7 Hilbert space. In total, for each separation, $\approx 37,000$ photons were collected. The results for a few sets of displacements, along with the corresponding theoretical predicted outcomes (Eq. (2)), are illustrated in the

form of correlation matrices (see Fig. 2b)). The figure shows that the experimental outcomes closely match the corresponding theoretical predictions. We also see the modes just outside the diagonal starting to increase in significance symmetrically with the increasing separation. In order to obtain the estimates of the separation

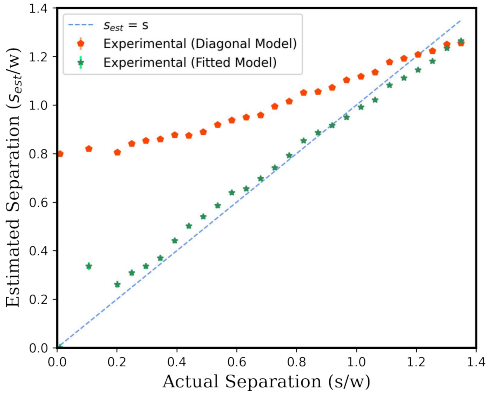

Figure 3. Estimates from the data vs the Actual Separation. The estimation was first performed assuming an ideal theoretical model, i.e. a perfectly diagonal mode decomposition (red) where probabilities are defined by Eqn. (2). We see a significant deviation from the ideal $s_{est} = s$ estimates, most likely due to modal cross-talk, attenuation, and dark counts. Therefore, in order to account for these effects, a linear fitting of the counts, as functions of the theoretical probabilities, was performed before the estimation, the results of which closely match the ideal curve (green).

parameter s, first, we perform the least squares fitting for the normalized counts (or equivalently probabilities) to the expression. $P_{ij} = \alpha_{ij}\mathcal{P}_{ij} + \beta_{ij}$, where $\mathcal{P}_{ij}$s are the theoretical probabilities given by Eq. (2), α_{ij} is a scaling factor to account for attenuation for different modes, and an additive factor β_{ij} to account for the spurious photon counts. For each separation, we then applied a Maximum Likelihood Estimation procedure (MLE), maximizing the likelihood function defined as $L(s) := (N!/\prod n_{ij}!)\prod_{ij} P_{ij}(s)^{n_{ij}}$, where $n_{i,j}$'s are the photon counts for the joint projection onto HG_{0i} for signal and HG_{0j} for the idler, and N is the total photon counts in all of the modes for that particular separation. The results of the estimation are shown in Fig. (3).

In order to compare the precision in the estimates obtained from this method with direct imaging, we also performed simulation runs of the experimental outcomes for the direct imaging of the SPDC point sources whose mode decomposition is characterized by $\gamma = 0.15$. The simulation results are plotted in Fig (4). We see that the biphoton SPADE outperforms the direct imaging of the SPDC and also the direct imaging of the Gaussian

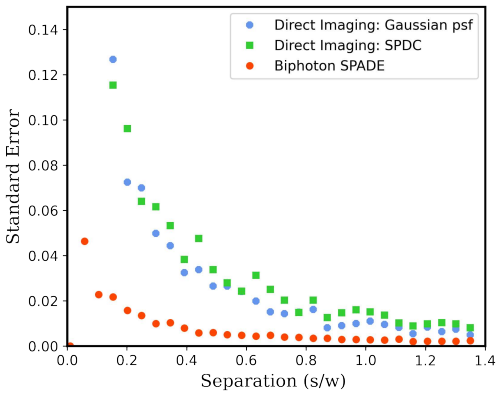

Figure 4. Simulation results for Biphoton SPADE compared with Direct Imaging of both Gaussian and SPDC PSFs for N = 37,000 photons. A 50-pixel array was used for direct imaging simulation, corresponding to intensity measurements at 50 different points. Similarly, for the biphoton SPADE ($K = 11.6$), the simulation was done for 49 mode projections with combinations of Hermite Gauss modes with indices $n = 0, m = 0, \ldots, 6$ for each signal and idler. A maximum likelihood estimation was performed on generated samples, and the standard error in the separation estimates was plotted.

with the same waist as the Schmidt's waist, especially offering an order of magnitude advantage for near zero separation.

DISCUSSION AND CONCLUSION

We have theoretically derived optimal projective measurements for separation estimation using a biphoton wavefunction generated via the SPDC process. The Fisher information for projection onto these modes remains constant even for near zero separation, which shows that the measurement scheme is not plagued by the so-called "Rayleigh's curse" inherent in Direct Imaging. Moreover, the precision in the proposed method is limited only by the strength of the spatial correlations inherent in the photon pairs. In particular, we show that the total Fisher information of the separation estimation is proportional to the square root of the Schmidt rank (K) of the system. Therefore, depending upon the strength of the correlations in the system, the method even offers further enhancement that scales with K compared to ordinary SPADE, which corresponds to the trivial case of $K = 1$. As a proof of concept, we also experimentally implemented the scheme using down-converted photon pairs and obtained results that are in good agreement with the theoretical predictions. We also performed simulations comparing the precision in our estimates with the case of Direct Imaging, where we indeed observe at least an or-

der of magnitude improvements, especially for near zero separations, where the errors start to diverge. Our theoretical and experimental results suggest the potential of using high-dimensional entanglement for further enhancing super-resolution measurements. Combined with neural networks (see, e.g. Ref. [20]), this technique can provide a new tool for high-resolution imaging in low-light conditions of passive samples with variable transmissivity. As a perspective, we believe that these ideas may have an appeal also in electron microscopy where the resolution problem is very relevant especially when trying to separate two close point-like objects like atoms. Optimal measurements (to which SPADE belongs) in the single electron framework have been already studied [33] but the recent advances in controlling entangled electrons [34, 35] could pave the way to increase the resolution below 10 pm, which would be the highest spatial resolution achieved so far. More generally, the Schmidt decomposition of electron pair could provide a new framework for advanced metrology in quantum transmission electron microscopy.

Acknowledgement: E.K. acknowledges the scientific discussions with Professor Aephraim Steinberg. This work was supported by the Canada Research Chair (CRC) Program, NRC-uOttawa Joint Centre for Extreme Quantum Photonics (JCEP) via the Quantum Sensors Challenge Program at the National Research Council of Canada, and the European Union's Horizon 2020 Research and Innovation Programme under grant agreement No 766970 (QSORT).

[1] L. Rayleigh, Xxxi. investigations in optics, with special reference to the spectroscope, The London, Edinburgh, and Dublin Philosophical Magazine and Journal of Science **8**, 261 (1879).
[2] E. Ash and G. Nicholls, Super-resolution aperture scanning microscope, Nature **237**, 510 (1972).
[3] E. Betzig and J. K. Trautman, Near-field optics: microscopy, spectroscopy, and surface modification beyond the diffraction limit, Science **257**, 189 (1992).
[4] M. Von Ardenne, Das elektronen-rastermikroskop, Zeitschrift für Physik **109**, 553 (1938).
[5] J. Tersoff and D. R. Hamann, Theory and application for the scanning tunneling microscope, Physical review letters **50**, 1998 (1983).
[6] M. Tsang, R. Nair, and X.-M. Lu, Quantum theory of superresolution for two incoherent optical point sources, Physical Review X **6**, 031033 (2016).
[7] R. Kerviche, S. Guha, and A. Ashok, Fundamental limit of resolving two point sources limited by an arbitrary point spread function, in *2017 IEEE International Symposium on Information Theory (ISIT)* (IEEE, 2017) pp. 441–445.
[8] M. Paúr, B. Stoklasa, Z. Hradil, L. L. Sánchez-Soto, and J. Rehacek, Achieving the ultimate optical resolution, Optica **3**, 1144 (2016).
[9] P. Boucher, C. Fabre, G. Labroille, and N. Treps, Spatial optical mode demultiplexing as a practical tool for optimal transverse distance estimation, Optica **7**, 1621 (2020).
[10] W.-K. Tham, H. Ferretti, and A. M. Steinberg, Beating rayleigh's curse by imaging using phase information, Physical review letters **118**, 070801 (2017).
[11] Z. Hradil, J. Řeháček, L. Sánchez-Soto, and B.-G. Englert, Quantum fisher information with coherence, Optica **6**, 1437 (2019).
[12] K. Liang, S. A. Wadood, and A. Vamivakas, Coherence effects on estimating two-point separation, Optica **8**, 243 (2021).
[13] S. Kurdzialek, Back to sources–the role of coherence in super-resolution imaging revisited, arXiv preprint arXiv:2103.12096 (2021).
[14] M. Gessner, C. Fabre, and N. Treps, Superresolution limits from measurement crosstalk, Physical Review Letters **125**, 100501 (2020).
[15] Y. L. Len, C. Datta, M. Parniak, and K. Banaszek, Resolution limits of spatial mode demultiplexing with noisy detection, International Journal of Quantum Information **18**, 1941015 (2020).
[16] L. Santamaria, D. Pallotti, M. S. de Cumis, D. Dequal, and C. Lupo, Balanced spade detection for distance metrology, arXiv preprint arXiv:2206.05246 (2022).
[17] J. Yang, S. Pang, Y. Zhou, and A. N. Jordan, Optimal measurements for quantum multiparameter estimation with general states, Physical Review A **100**, 032104 (2019).
[18] S. Zhou and L. Jiang, Modern description of rayleigh's criterion, Physical Review A **99**, 013808 (2019).
[19] K. K. Bearne, Y. Zhou, B. Braverman, J. Yang, S. Wadood, A. N. Jordan, A. Vamivakas, Z. Shi, and R. W. Boyd, Confocal super-resolution microscopy based on a spatial mode sorter, Optics Express **29**, 11784 (2021).
[20] A. Pushkina, G. Maltese, J. Costa-Filho, P. Patel, and A. Lvovsky, Superresolution linear optical imaging in the far field, Physical Review Letters **127**, 253602 (2021).
[21] D. Sych, V. Averchenko, and G. Leuchs, Generic method for lossless generation of arbitrarily shaped photons, Phys. Rev. A **96**, 053847 (2017).
[22] E. Polino, M. Valeri, N. Spagnolo, and F. Sciarrino, Photonic quantum metrology, AVS Quantum Science **2**, 024703 (2020).
[23] V. Giovannetti, S. Lloyd, and L. Maccone, Advances in quantum metrology, Nature photonics **5**, 222 (2011).
[24] C. W. Helstrom, Quantum detection and estimation theory, Journal of Statistical Physics **1**, 231 (1969).
[25] F. M. Miatto, H. di Lorenzo Pires, S. M. Barnett, and M. P. van Exter, Spatial schmidt modes generated in parametric down-conversion, The European Physical Journal D **66**, 1 (2012).
[26] M. Fedorov, Y. M. Mikhailova, and P. Volkov, Gaussian modelling and schmidt modes of spdc biphoton states, Journal of Physics B: Atomic, Molecular and Optical Physics **42**, 175503 (2009).
[27] F. M. Miatto, T. Brougham, and A. M. Yao, Cartesian and polar schmidt bases for down-converted photons, The European Physical Journal D **66**, 1 (2012).
[28] G. S. Thekkadath, L. Giner, X. Ma, J. Flórez, and J. S. Lundeen, Projecting onto any two-photon polarization state using linear optics, New Journal of Physics **20**,

083033 (2018).
[29] S. Straupe, D. Ivanov, A. Kalinkin, I. Bobrov, and S. Kulik, Angular schmidt modes in spontaneous parametric down-conversion, Physical Review A **83**, 060302 (2011).
[30] E. Bolduc, N. Bent, E. Santamato, E. Karimi, and R. W. Boyd, Exact solution to simultaneous intensity and phase encryption with a single phase-only hologram, Optics letters **38**, 3546 (2013).
[31] F. Bouchard, N. H. Valencia, F. Brandt, R. Fickler, M. Huber, and M. Malik, Measuring azimuthal and radial modes of photons, Optics express **26**, 31925 (2018).
[32] N. K. Fontaine, R. Ryf, H. Chen, D. T. Neilson, K. Kim, and J. Carpenter, Laguerre-gaussian mode sorter, Nature communications **10**, 1 (2019).
[33] F. Troiani, E. Rotunno, S. Frabboni, R. B. Ravelli, P. J. Peters, E. Karimi, and V. Grillo, Efficient molecule discrimination in electron microscopy through an optimized orbital angular momentum sorter, Physical Review A **102**, 043510 (2020).
[34] S. Meier, J. Heimerl, and P. Hommelhoff, Few-electron correlations after ultrafast photoemission from nanometric needle tips, arXiv preprint arXiv:2209.11806 (2022).
[35] R. Haindl, A. Feist, T. Domröse, M. Möller, S. V. Yalunin, and C. Ropers, Coulomb-correlated few-electron states in a transmission electron microscope beam, arXiv preprint arXiv:2209.12300 (2022).
[36] I. S. Gradshteyn and I. M. Ryzhik, *Table of integrals, series, and products* (Academic press, 2014).

Supplementary Information for: Super-resolution enhancement in bi-photon spatial mode demultiplexing

Section S1. OPTIMAL PROJECTION

Fisher information describes the amount of information a measurement contains about a certain parameter being estimated. The Cramer-Rao Lower Bound, which is the minimum possible variance on the unbiased estimation of the parameter, is given by the inverse of the Fisher Information[23],

$$\sigma_{crlb} \geq \frac{1}{\sqrt{\mathcal{FI}}} \geq \frac{1}{\sqrt{Tr[\frac{\partial \rho}{\partial \delta} L]}} \tag{S1}$$

where ρ is the state of the system, δ is the parameter to be estimated and L is the so called symmetric logarithmetic operator defined as $\rho L + L\rho = 2\frac{\partial \rho}{\partial \delta}$. Higher the Fisher Information associated with a particular set of measurement, better the precision in the estimates.
In the super resolution schemes for separation estimation with the so called Spatial Mode Demultixplexing (SPADE), a projective measurement is carried out in spatial modes (most commonly in the Hermite Gauss basis). The Fisher Information of a parameter δ, in the basis of such set of spatial modes $\{|j\rangle \langle j|\}$ is given by,

$$\mathcal{FI} = \sum_j \frac{1}{\mathcal{P}_j} \left(\frac{\partial \mathcal{P}_j}{\partial \delta} \right)^2 \tag{S2}$$

where $\mathcal{P}_j$ is probability associated with the successful projection in the corresponding mode $|j\rangle$.

In the small separation regime, where errors from direct imaging start to diverge, one can find an optimal basis of projective measurements for which the Fisher information remains constant. For a general point spread function(PSF) $|\Psi(x)\rangle$, the "optimal" mode of projection is proportional to its derivative which can be seen as follows,

The displaced PSFs $\langle x_s|\Psi\rangle^{\pm} = \langle x_s|\Psi(x \pm s)\rangle$, where $\delta = 2s$, can be expanded in terms of the derivatives of the original PSF as,

$$\langle x_s|\Psi\rangle^{\pm} = \sum_n \frac{(\pm s)^n \langle x_s|\Psi\rangle^{(n)}}{n!} \tag{S3}$$

where $\langle x_s|\Psi\rangle^{(n)}$ is the n^{th} derivative in x_s of $\langle x_s|\Psi\rangle$. For small separations, we can consider only upto the first order term in the separation,

$$\langle x_s|\Psi\rangle^{\pm} \approx \langle x_s|\Psi\rangle \pm s \langle x_s|\Psi\rangle^{(1)} + O(s^2) \tag{S4}$$

If the two displaced PSFs are incoherent then the resulting state is characterized by a completely mixed state,

$$\rho = \frac{1}{2}\left[|\Psi\rangle^{+}\langle\Psi| + |\Psi\rangle^{-}\langle\Psi| \right] \tag{S5}$$

where $|\Psi\rangle^{\pm}$ refer to the wavefunctions displaced by $\pm s$ in the x axis.
If we plug S4 into S5 we find the density matrix approximated for small separations,

$$\rho \approx |\Psi\rangle\langle\Psi| + s^2 |\Psi\rangle^{(1)}\langle\Psi|^{(1)} + \frac{s^2}{2}\left(|\Psi\rangle^{(2)}\langle\Psi| + |\Psi\rangle\langle\Psi|^{(2)} \right) \tag{S6}$$

The probability of successful projection onto the normalized first derivative mode is,

$$\begin{aligned}\mathcal{P}_{der} &\approx \frac{1}{\mathcal{N}} \langle\Psi|^{(1)} \rho_{BI} |\Psi\rangle^{(1)} \\ &\approx \frac{s^2}{\mathcal{N}} |\langle\Psi|^{(1)} |\Psi\rangle^{(1)}|^2 \\ &\approx \frac{s^2}{\mathcal{N}} = \frac{\delta^2}{4\mathcal{N}},\end{aligned} \tag{S7}$$

where $\mathcal{N}$ is the normalization factor. The Fisher information can be calculated as,

$$\mathcal{FI}_{der} = \frac{1}{\mathcal{P}_{der}} \left(\frac{\partial \mathcal{P}_{der}}{\partial \delta}\right)^2 = \mathcal{N} \tag{S8}$$

We see that in the small separation regime, the Fisher Information in the derivative mode is a constant regardless of the separation.

Section S2. SCHMIDT DECOMPOSITION OF SPDC

The bi-photon state generated in Spontaneous Parametric Down Conversion (SPDC) process can be decomposed into a superposition of tensor product of two linear combinations of Hermite-Gauss modes S9,

$$|\Psi\rangle = \sum_{m,n} \sum_{m',n'} C_{mn}^{m'n'} |m,n\rangle_s \otimes |m',n'\rangle_i \tag{S9}$$

Hermite-Gauss $\mathcal{HG}$ modes $|m,n\rangle = |m\rangle \otimes |n\rangle$ form an orthonormal basis of spatial modes for the transverse plane and have the following expressions (2D and 1D respectively) in adimensional coordinates:

$$\langle x_o, y_o | m,n\rangle = \frac{1}{\sqrt{2^m 2^n m! n! \pi}} \mathcal{H}_m(x_o) e^{-\frac{x_o^2}{2}} \otimes \mathcal{H}_n(y_o) e^{-\frac{y_o^2}{2}} \tag{S10}$$

$$\langle x_o | m\rangle = \frac{1}{\sqrt{2^m m! \sqrt{\pi}}} \mathcal{H}_m(x_o) e^{-\frac{x_o^2}{2}} \tag{S11}$$

where $\mathcal{H}_i(x_k)$ is the Hermite polynomial of the i^{th} order for the variable x_k, and $x_o = \frac{\sqrt{2}}{\sigma_s} x$, $y_o = \frac{\sqrt{2}}{\sigma_s} y$ as defined in the main text. When expressed in the Schmidt basis of Hermite Gauss $\mathcal{HG}$ modes the original SPDC state can be simplified to [25, 27, 29],

$$|\Psi\rangle = \sum_{m,n} C_{mn} |m,n\rangle_s \otimes |m,n\rangle_i \tag{S12}$$

where $C_{mn} = \frac{4\gamma}{(1+\gamma)^2} |\frac{1-\gamma}{1+\gamma}|^{(m+n)}$ and where γ is a constant determined by source parameters such as crystal length and pump beam waist. When performing any sort of joint measurement (i-e coincidence counts or coincidence imaging) on the entangled state, we consider the PSF of the form of the biphoton expression given in S12. If a separation is introduced in the signal beam, it becomes a mixed state of two separated beams with the signal photon displaced in the x_s axis. The two-photon density matrix ρ_{BI} resembles equation S5, with $\langle x_s | m^{\pm}\rangle_s = \sqrt{\frac{1}{2^m m! \sqrt{\pi}}} \mathcal{H}_m(x_s \pm s) e^{-\frac{(x_s \pm s)^2}{2}}$:

$$\rho_{BI} = \sum_{m,n} \sum_{u,v} C_{mn} C_{uv}^* |m,n\rangle_{i\,i} \langle u,v| \otimes \left[|m^+,n\rangle_{s\,s} \langle u^+,v| + |m^-,n\rangle_{s\,s} \langle u^-,v| \right] \tag{S13}$$

The derivative of the PSF (S12) in x_s has the following form:

$$|\Psi\rangle^{(1)} = \sum_{m,n} C_{mn} \, |m\rangle_s^{(1)} \, |n\rangle_s \otimes |m,n\rangle_i$$

where we can find from the recurrence relations of the Hermite Polynomials, that:

$$|m\rangle_s^{(1)} = \sqrt{\frac{m}{2}} \, |m-1\rangle_s - \sqrt{\frac{m+1}{2}} \, |m+1\rangle_s \tag{S14}$$

So, the derivative becomes a maximally entangled state with the expression:

$$|\Psi\rangle^{(1)} = \sum_{m,n} C_{m,n} \left(\sqrt{\frac{m}{2}} \, |m-1\rangle_s - \sqrt{\frac{m+1}{2}} \, |m+1\rangle_s \right) |n\rangle_s \otimes |m,n\rangle_i \tag{S15}$$

Projecting onto such a state is not trivial and is outside the scope of this experiment. We instead chose to use measurements readily available to us experimentally in a setup with entangled photon pairs. A variety of measurements (either categorized as joint or single-photon measurements) are possible which will determine the projection outcomes $\mathcal{P}_i$. Using a joint basis of $\mathcal{HG}$ modes as the mode sorting basis, with elements $|k,l\rangle_s \langle k,l|_s \otimes |k',l'\rangle_i \langle k',l'|_i$, the projection outcomes $\mathcal{P}_{kl}^{k'l'}$ can be expressed as:

$$\begin{aligned} \mathcal{P}_{kl}^{k',l'} &= \mathrm{Tr}[|k,l\rangle_s \langle k,l|_s \otimes |k',l'\rangle_i \langle k',l'|_i \, \rho_{BI}] \\ &= \langle k,l|_s \otimes \langle k',l'|_i \, \rho_{BI} \, |k,l\rangle_s \otimes |k',l'\rangle_i \\ &= \frac{1}{2} C_{k',l}^2 \Big\{ |\langle k \, | k'^{+} \rangle|^2 + |\langle k \, | k'^{-} \rangle|^2 \Big\} \delta_{l,l'} \end{aligned} \tag{S16}$$

Section S3. ANALYTICAL EXPANSION OF $\langle m| \, n^{\pm} \rangle$

The inner product between an $\mathcal{HG}$ function of mode m and a displaced $\mathcal{HG}$ function of mode n can be written out as:

$$\langle m| \, n^{\pm} \rangle = \int_{-\infty}^{+\infty} \mathcal{HG}_m(x) \mathcal{HG}_n(x \pm s) dx$$

Applying a change of variables $u = x \pm \frac{s}{2}$ and inserting the expressions in S11:

$$\begin{aligned} \langle m| \, n^{\pm} \rangle &= \frac{1}{\sqrt{2^m 2^n m! n! \pi}} \int_{-\infty}^{+\infty} e^{-\frac{1}{2}[(u \mp \frac{s}{2})^2 + (u \pm \frac{s}{2})^2]} \mathcal{H}_m(u \mp \frac{s}{2}) \mathcal{H}_n(u \pm \frac{s}{2}) du \\ &= \frac{e^{-\frac{s^2}{4}}}{\sqrt{2^{m+n} m! n! \pi}} \int_{-\infty}^{+\infty} e^{-x^2} \mathcal{H}_m(u \mp \frac{s}{2}) \mathcal{H}_n(u \pm \frac{s}{2}) du \end{aligned} \tag{S17}$$

The integral in S17 is given in a table of integrals [36], where for $n \geq m$:

$$\int_{-\infty}^{+\infty} e^{-x^2} \mathcal{H}_m(x+y) \mathcal{H}_n(x+z) dx = 2^n \pi m! z^{n-m} \mathcal{L}_m^{n-m}(-2yz) \tag{S18}$$

where $\mathcal{L}_i^{\alpha}$ is the generalized Laguerre polynomial of order i,α. So, the analytical expression for the inner product is found to be, for $n \geq m$:

$$\langle m| \, n^{\pm} \rangle = \sqrt{\frac{m!}{n!}} 2^{\frac{m-n}{2}} (\pm s)^{n-m} e^{-\frac{s^2}{4}} \mathcal{L}_m^{n-m}(\frac{s^2}{2}) \tag{S19}$$

Section S4. BIPHOTON SPADE BASED ON PROJECTION ONTO HG-MODES

Here, we derive the main result showing the relation between the Fisher information and the Schmidt rank (K) in biphoton SPADE. In the small separation limit (using S4, S14) only three terms in S16 are non-zero:

$$\mathcal{P}_{kl}^{k'l'} \approx C_{k',l}^2 \left[\delta_{k,k'}^2 \{1 - \frac{s^2}{2}(2k'+1)\} + \delta_{k,k'-1}^2 \frac{k'}{2} + \delta_{k,k'+1}^2 \frac{k'+1}{2} \right] \delta_{l,l'}^2.$$

$$\begin{cases} \mathcal{P}_{kl}^{kl} \approx C_{k,l}^2 (1 - \frac{s^2}{2}(2k+1)) \\ \mathcal{P}_{kl}^{k+1,l} \approx s^2 C_{k+1,l}^2 \frac{k+1}{2} \\ \mathcal{P}_{kl}^{k-1,l} \approx s^2 C_{k-1,l}^2 \frac{k}{2} \end{cases} \tag{S20}$$

For $k = k'$ the $\mathcal{FI}$ about the parameter $\delta = 2s$ tends to 0. For $k = k' \pm 1$ the projection outcome has the same form as for optimal measurements, where $\mathcal{P}_i$ is proportional to δ^2.

$$\begin{cases} \mathcal{FI}_{kl}^{kl}(s) \approx \frac{\left[C_{k,l}^2 (2k+1)s\right]^2}{4 - 2s^2(2k+1)} \to 0 \\ \mathcal{FI}_{kl}^{k+1,l} \approx \frac{k+1}{2} C_{k+1,l}^2 \\ \mathcal{FI}_{kl}^{k-1,l} \approx \frac{k}{2} C_{k-1,l}^2 \end{cases} \tag{S21}$$

For example, projecting signal photon onto $|1,0\rangle_s$ and coupling idler photon into a single mode fiber (projection onto $|0,0\rangle_i$) would give a constant Fisher Information, for small separations, of $\frac{1}{2}C_{0,0}^2$. The total $\mathcal{FI}$ is obtained by summing the non-vanishing $\mathcal{FI}$ across all HG mode measurements. Writing out the coefficients explicitly:

$$\begin{cases} \mathcal{FI}_{kl}^{k+1,l} \approx \frac{k+1}{2} C_{0,0}^2 \left(\frac{1-\gamma}{1+\gamma}\right)^{2(k+1)} \left(\frac{1-\gamma}{1+\gamma}\right)^{2l} \\ \mathcal{FI}_{kl}^{k-1,l} \approx \frac{1}{2} k C_{0,0}^2 \left(\frac{1-\gamma}{1+\gamma}\right)^{2(k-1)} \left(\frac{1-\gamma}{1+\gamma}\right)^{2l} \end{cases}$$

and using $\sum_k k \left(\frac{1-\gamma}{1+\gamma}\right)^{2k} = \frac{(1-\gamma)^2(1+\gamma)^2}{16\gamma^2}$, $\sum_k \left(\frac{1-\gamma}{1+\gamma}\right)^{2k} = \frac{(1+\gamma)^2}{4\gamma}$ we can calculate the sum over k for the 1D case S22 or the sum over all k, l S23.

$$\begin{cases} \sum_k \mathcal{FI}_{kl}^{k+1,l} = \frac{1}{2}(\frac{1-\gamma}{1+\gamma})^2 \approx 0.27 \\ \sum_k \mathcal{FI}_{kl}^{k-1,l} = \frac{1}{2} \end{cases} \tag{S22}$$

$$\begin{cases} \sum_{k,l} \mathcal{FI}_{kl}^{k+1,l} = \frac{(1-\gamma)^2}{8\gamma} \approx 0.60 \\ \sum_{k,l} \mathcal{FI}_{kl}^{k-1,l} = \frac{(1+\gamma)^2}{8\gamma} \approx 1.10 \end{cases} \tag{S23}$$

The numerical values correspond to the FI value for a $\gamma = 0.15$, as in the experiment. Note that for strong spatial correlations, the value of γ gets closer to 0 and the total FI increases. In fact, the schmidt number $K = \frac{(\gamma+\gamma^{-1})^2}{4}$, which is often used as a measure to describe the strength of spatial entanglement in the SPDC pair, can be found in the total FI sum:

$$\sum_{k,l} \mathcal{FI}_{coinc} = \frac{1}{4}(\gamma + \gamma^{-1}) = \frac{1}{2}\sqrt{K} \geq \frac{1}{2} \tag{S24}$$

Section S5. GAUSSIAN CASE ($\gamma = 1$)

Note that $\gamma = 1$, corresponds to a simple separable product state of a two gaussian wavefunctions for signal and idler. In that case, the total Fisher Information according to Eq. S24 reduces to $\frac{1}{2}(\frac{N}{\sigma_s^2})$, which can be briefly seen as follows: The state after displacement can be represented by a density matrix $\rho = \frac{1}{2}\big[\,|0^+0\rangle\langle 0^+0| + |0^-0\rangle\langle 0^-0|\,\big]$. At the small separation regime the optimal mode of projection is the first order Hermite Gauss mode $\mathcal{HG}_{01}$, for which the probability for a successful projection is given by,

$$P_1 = \langle 10|\,\rho\,|10\rangle = \frac{1}{2}\big[|\,\langle 1|\,0^+\rangle|^2 + |\,\langle 1|\,0^-\rangle|^2\big]$$

Using equation S19, we have that $\langle 1|\,0^+\rangle = \langle 1^-|\,0\rangle = -\sqrt{\frac{1}{2}}se^{-\frac{s^2}{4}}$ and that $\langle 1|\,0^-\rangle = \langle 1^+|\,0\rangle = \sqrt{\frac{1}{2}}se^{-\frac{s^2}{4}}$. The probability outcome P_1 is given by:

$$P_1 = \frac{1}{2}s^2e^{-\frac{s^2}{2}}$$

with Fisher Information of:

$$FI_1 = \frac{1}{P_1}\left(\frac{\partial P_1}{\partial(2s)}\right) = \frac{1}{4}(2 - 2s^2 + \frac{s^4}{2})e^{-\frac{s^2}{2}} \approx \frac{1}{2}(\frac{N}{\sigma_s^2})$$

The total FI for the simple gaussian case does indeed correspond to the total FI when $\gamma = 1$. The entanglement scheme thus provides an advantage over classical SPADE for any level of entanglement with $\gamma < 1$.

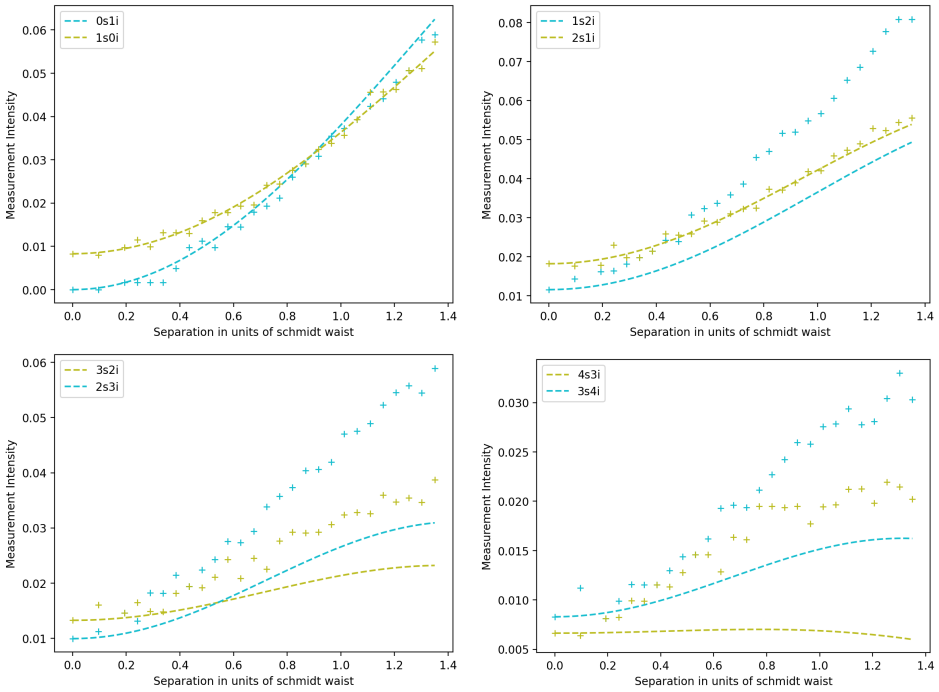

Figure 19: Experimental data versus no-noise non-schmidt model. The plots show the experimental data collected and the simulated projection outcomes from Eq.(43) with $C^{l,l'}_{k,k'}$ chosen as the square root of 7x7 normalized experimental cross-talk matrix coefficients - all coefficients are considered real valued, as we do not have the full SPDC state experimentally characterized to perform a precise tomography. n_i, m_s in the legend represent the joint projection measurement of idler photon onto $\mathcal{HG}_n$ and signal photon onto $\mathcal{HG}_m$.

3 Spin-Orbit Coupling in Spherulite Crystals

In the previous section of this work, we showed that super-resolution methods in far field imaging systems can be obtained by sorting the light field into structured spatial modes. In particular, we saw that spatial mode projection can be accomplished in two steps [10]: imparting a phase and amplitude onto

the reference beam, and coupling the beam into a SMF. While the step 1 of beam shaping is accomplished with a SLM, we explore in this section another mechanism that allows for the generation of structured light. Indeed, we describe how spin-orbit coupling phenomena occurs in birefringent materials and show, by example of ascorbic acid, how many natural crystalline spherulite structures can be exploited to generate beams with orbital angular momentum.

This chapter is based on the following paper:

Grenapin, Florence, D'Errico, Alessio and Karimi, Ebrahim. "Spin–orbit coupling induced by ascorbic acid crystals" Nanophotonics, 2023. https://doi.org/10.1515/nanoph-2022-0502

3.1 Methods

In this section, we hope to clarify the decisions that were made in the process of perfecting the technique described in the paper. We will talk about polarization tomography and interferometry, two methods that confirmed the waveplate nature of ascorbic acid. Finally, we will walk through the fabrication process of ascorbic acid crystals.

3.1.1 Polarization Tomography

In order to measure the polarization effects of the ascorbic acid spherulite waveplate around a defect, we use a tomography method to evaluate the lo-

cal polarization ellipse at every point along the beam wavefront. The local polarization ellipse can be fully determined by the four Stokes parameters: $\{s_0, s_1, s_2, s_3\}$. These parameters represent any polarization state, whether it be fully or partially polarized, and can be obtained simply by measuring the six different local intensities associated to each polarization component $I_{H,V,A,D,L,R}$, and where I_P and I_{NP} are the polarized and non-polarized components of the light, respectively:

$$s_0 = I_{total} = I_P + I_{NP}, \tag{44}$$

$$s_1 = I_H - I_V, \tag{45}$$

$$s_2 = I_A - I_D, \tag{46}$$

$$s_3 = I_L - I_R. \tag{47}$$

The respective intensities are obtained by projecting the light field on the correspondent polarization mode, by means of a polarizer (or a combination of HWP, QWP, and polarizing beamsplitter which act as one). Since the parameters depend on easily measurable quantities, this Stokes representation is useful for characterizing light polarization at any local point on the wavefront. States of linear polarization have $s_3 = 0$ and otherwise the sign of s_3 determines the handedness of the polarization ellipse. For an arbitrary degree of polarization $P = \frac{\sqrt{s_1^2+s_2^2+s_3^2}}{s_0}$ we can define the Stokes vector v_S as:

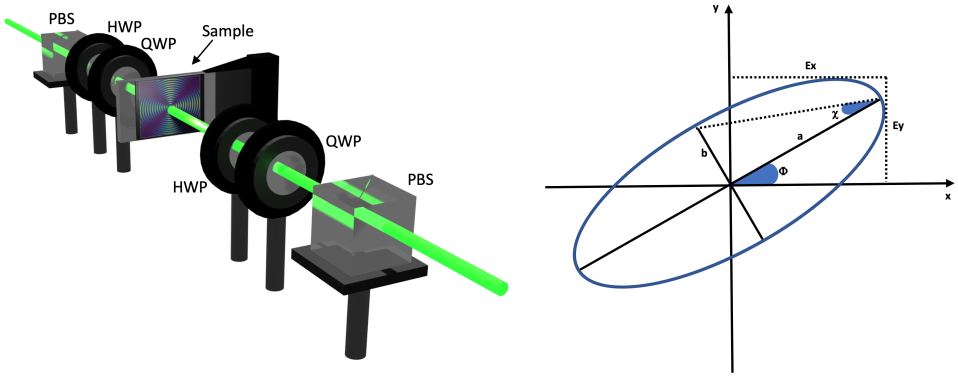

Figure 20: **Left.** Experimental setup used to control input and analyze output polarization states generated by ascorbic acid crystals. Legend: polarizing beamsplitter (PBS); half-wave plate (HWP); quarter-wave plate (QWP). **Right.** Schematic of a polarization ellipse, with x and y axes aligned with the horizontal and vertical components of the electric field, E_x and E_y, respectively.

$$v_S = (1-P)\begin{bmatrix} s_0 \\ 0 \\ 0 \\ 0 \end{bmatrix} + P\begin{bmatrix} s_0 \\ s_1 \\ s_2 \\ s_3 \end{bmatrix} \tag{48}$$

Which, for completely unpolarized light (P=0) is not interesting to our case, and for completely polarized light (P=1), such as is the case in the tomography setup (see Fig.(20)), simply reduces to: $v_s = \begin{bmatrix} s_0 \\ s_1 \\ s_2 \\ s_3 \end{bmatrix}$.

The expression for the angles of the local polarization ellipse (see Fig.(20)) are: $\Phi = \frac{1}{2}Tan^{-1}(\frac{s_2}{s_1})$ and $\chi = Tan^{-1}(\frac{s_3}{\sqrt{s_1^2+s_2^2}})$. Therefore measuring the six projection intensities at various points of a wavefront is enough to obtain the polarization ellipse for those points. Measuring the intensity of the beam

after a projection onto a polarization mode allows us to build the polarization ellipse at almost every pixel covering the wavefront of the beam. For instance, if the polarization pattern of the wavefront is uniform, then the ellipses will be identical at every point. Alternatively, light carrying orbital angular momentum (OAM) of a certain value m, such as vector vortex beams generated by q-plates, has a helical wavefront, which means the polarization ellipses perform a $2m\pi$ rotation around a singular point.

The setup for polarization analysis measurements is shown in Fig.(20). A wavelength of 533nm is used since, experimentally, it showed the most contrasted Maltese pattern and is thus closer to a half-wave retardation. The PBS, HWP, and QWP combination allow us to control polarization of input light. For each input polarization, the second set of HWP, QWP, and PBS allow for projection onto polarization states H(linear horizontal), V(linear vertical), A(linear anti-diagonal), D(linear diagonal), R(right circular), L(left circular).

For each input polarization, the point by point stokes parameters of the output light can be retrieved in a straightforward manner from the projections using their definition Eq.(44):

The local polarization ellipses, or simply the angle of the major axis of the ellipses (see the manuscript 3.2) can then be obtained using the definition of the ellipse angles (see Fig.(23)).

With input H polarization, collecting projections onto the four linear polarization states is sufficient to retrieve all stokes parameters, when we approx-

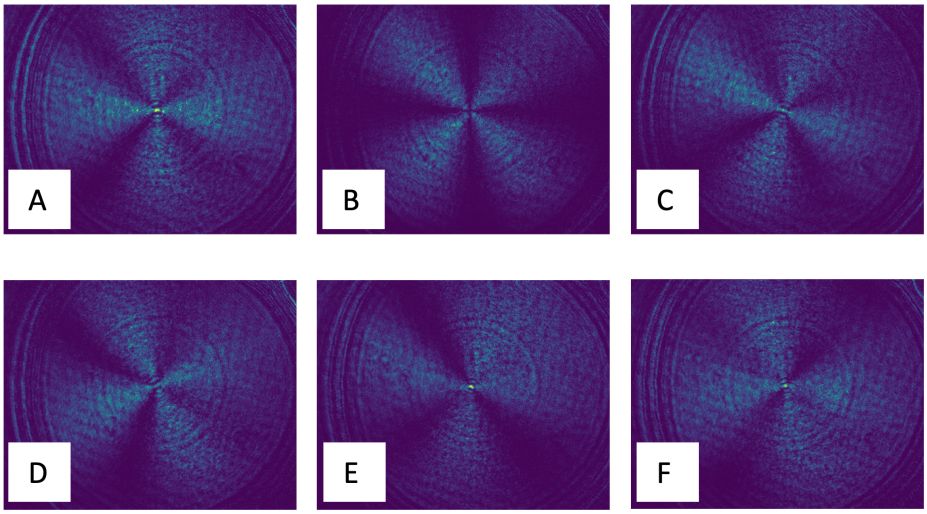

Figure 21: Recorded intensity measurements of light having passed through an ascorbic acid defect with H linear input polarization, after projections onto: **A.** Horizontal. **B.** Vertical. **C.** Antidiagonal. **D.** Diagonal. **E.** Left circular. **F.** Right circular.

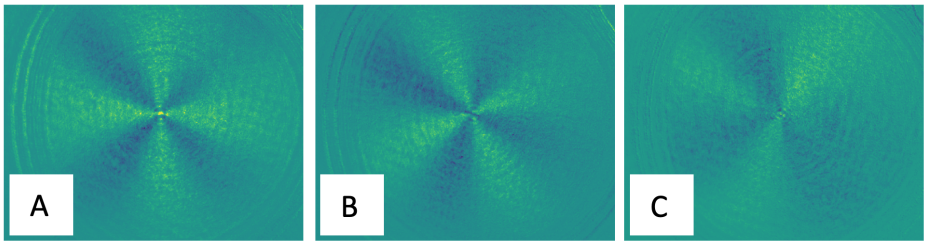

Figure 22: Density plot of local Stokes parameters of light after passing through an ascorbic acid defect with H linear input polarization, obtained from images in fig[21]. **A.** Point by point s_1 parameter. **B.** Point by point s_2 parameter. **C.** Point by point s_3 parameter.

imate the output light to be completely polarized in each point (P=1). For fully polarized light, $s_0^2 = s_1^2 + s_2^2 + s_3^2$ is satisfied and can be used to retrieve s_3 without projecting onto the circular polarization states R and L. This is how we recorded in real time the polarization effects of ascorbic acid during

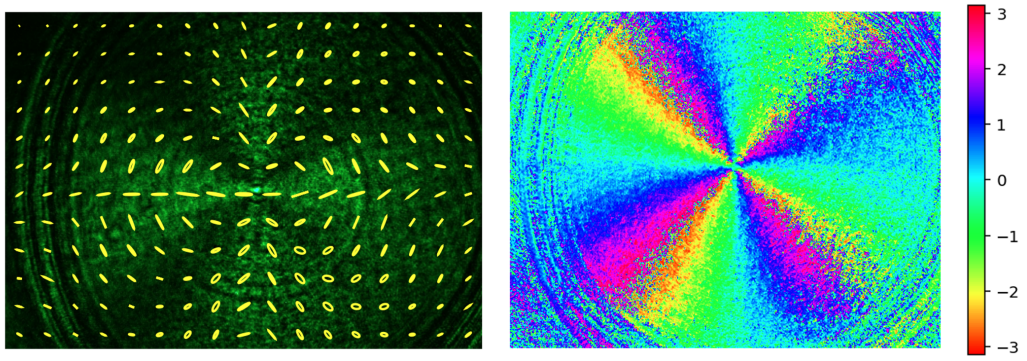

Figure 23: An example of polarization analysis results for H input polarizations. Similar results are shown in our publication 3.2. **Left.** Constructed polarization ellipses of regions 50×50 pixels wide. **Right.** Density plot of local polarization ellipse angle Φ using the CSV colorbar in matplotlib.

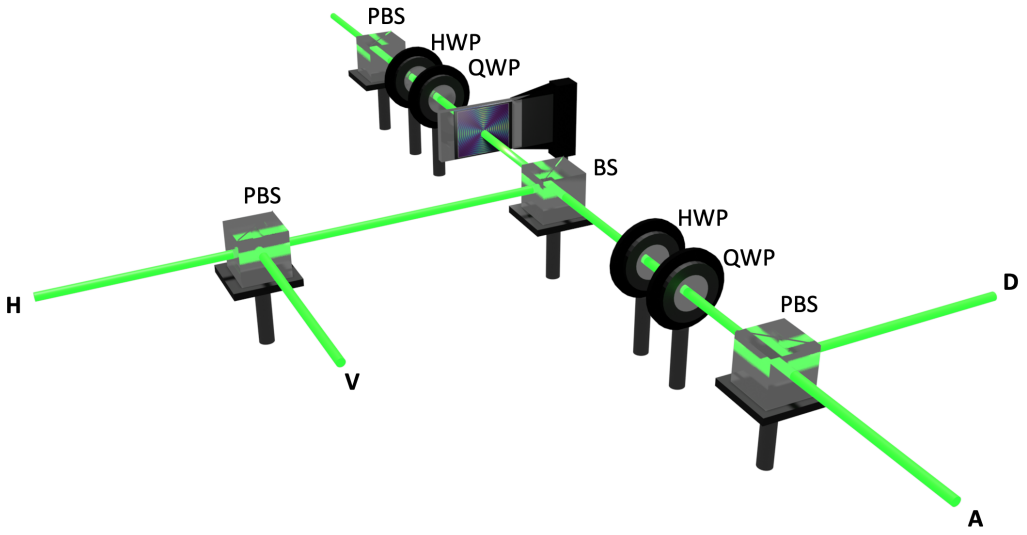

Figure 24: Experimental setup used to control input and analyze output polarization states generated by ascorbic acid crystals, in real time during their growth. Four thorlabs cameras are simultaneously recording at the four output ports H,V,A,D (not shown).

its growth around defects. (Illustrated in Fig.(24), and our manuscript 3.2).

3.1.2 Interferometry

In addition to performing a point by point polarization characterization of the beam passing through the spherulite waveplate, in the work we confirm generation of vector vortex beams by using tilted interferometry. The method consists of interfering a tilted reference beam (Gaussian or plane wave) with the signal beam, whose wavefront was modified by the ascorbic acid. The interference pattern contains the transverse phase information of the signal and thus, can determine the wavefront of the signal beam.

OAM-carrying beams have a helical wavefront since they carry a certain value l of angular momentum, which translates to a transverse phase of $P_{OAM} = e^{il\phi}$. When interfering with a tilted Gaussian, the resulting interference pattern consists of spiral fringes where the number of spirals depends on the OAM number l, and the handedness is determined by the sign of l. To show this quickly let us assume a Gaussian beam E_g is tilted at an angle about the y axis from the z axis of propagation. Because of the tilting, it has phase component in the x-y plane of: $P_g = e^{ikx}$. Then the total transverse field intensity is given in Eq.(49), where A_{oam} and A_g are the amplitudes related to the reference and signal fields. See Fig.(25) for the expected interference patterns.

$$I_{tot} = |A_{OAM}P_{OAM} + A_gP_g|^2 \tag{49}$$

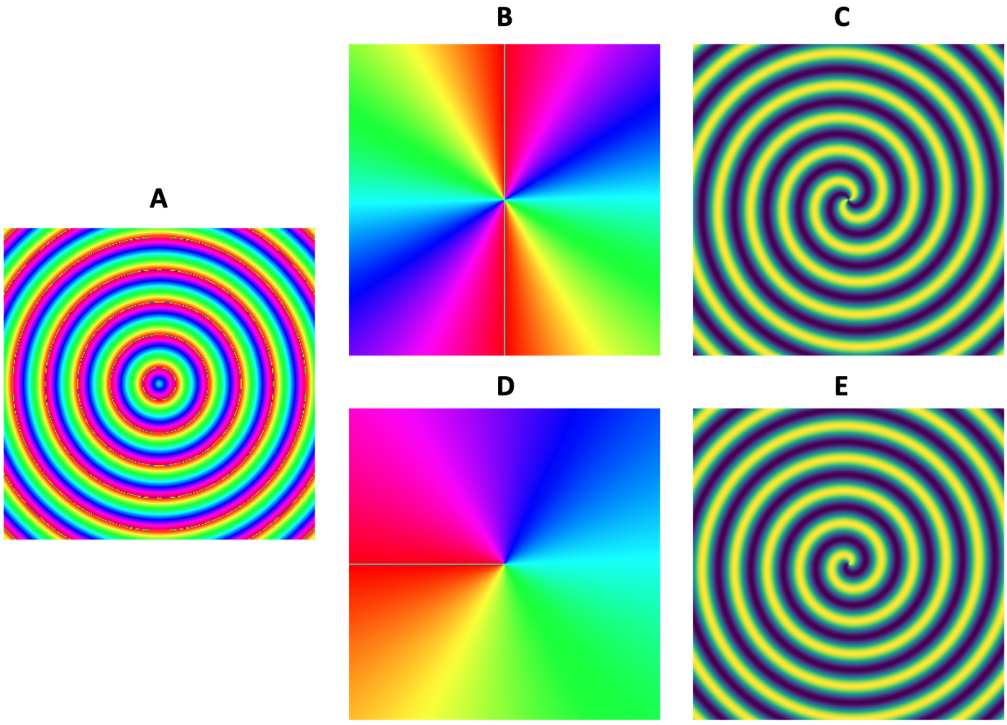

Figure 25: **A**-Plot of the transverse phase of a tilted Gaussian reference beam P_g. **Top.** **B**-Plot of the transverse phase of a vector vortex beam with an OAM value of $l = 2$. **C**-Simulated interference pattern Eq.(49) between **A** and **B**. **Bottom.** Same sequence, but with $l = 1$.

As shown in our manuscript 3.2, the interferometry confirmed generation of OAM-carrying beams, indicating that the spin-to-orbit coupling expected from the theory of a q-plate of q=1 indeed happened.

3.1.3 Fabrication

In nature spherulite structures of ascorbic acid crystals form under fairly standard conditions, and thus fabricating the crystals consisted simply of two steps: a dissolution into a solvent and a drying out phase, during which

the crystals start to form. A mix of water and ethanol was used as a solvent, with varying ratios. We show results for a 10:1 ethanol:water mix, dried at room temperature, and for a 100% water solvent, dried in the oven at varying temperatures (See the manuscript 3.2). Since the scattering of natural defects is a random process, at this scale and with rudimentary equipment, each batch of crystals turned out slightly differently. In most cases, the crystals formed around point defects on the slide or introduced by excess powder grains, and we could observe Maltese patterns. The density of defects present and the room temperature affected the size and shape of the patterns in each batch. For example, at slightly higher temperatures, the patterns were larger and were developing with double bands (see section 1.1.2) more often. In some cases, the crystals formed around line boundaries and the resulting pattern between cross polarizers altered significantly (see Fig.(26)).

3.2 Publication

Research Article

Florence Grenapin, Alessio D'Errico* and Ebrahim Karimi

Spin–orbit coupling induced by ascorbic acid crystals

https://doi.org/10.1515/nanoph-2022-0502
Received August 25, 2022; accepted December 9, 2022;
published online January 16, 2023

Abstract: Some anisotropic materials form semicrystalline structures, called spherulites, when observed in a polarisation microscope, exhibit a characteristic "maltese-cross"-like pattern. While this observation has been hitherto considered as a tool to characterize these materials, we show that these patterns are associated with a strong light's spin–orbit coupling induced by the spherulite structures. We experimentally demonstrate these effects using samples of crystallized ascorbic acid and observing the creation of optical vortices in transmitted laser beams, as well as the formation of inhomogeneous polarisation patterns. Our findings suggest the use of some spherulites based on other materials in frequency ranges, e.g. in the THz domain, where polarisation and spatial shaping of electromagnetic radiation is still a challenging task.

Keywords: metasurfaces; orbital angular momentum; spherulites; structured light.

1 Introduction

Polymer spherulites are spherically symmetric semicrystalline structures typically observed when a molten polymer is slowly cooled down [1]. The slow cooling allows polymer chains to form in ordered configurations. The crystallization starts around point defects and consists of lamellae structures that, in the absence of temperature gradients, grow radially from the defect centre.

***Corresponding author: Alessio D'Errico**, Nexus for Quantum Technologies, University of Ottawa, K1N 5N6, ON, Ottawa, Canada, E-mail: aderrico@uottawa.ca. https://orcid.org/0000-0002-6964-4328
Florence Grenapin, Nexus for Quantum Technologies, University of Ottawa, K1N 5N6, ON, Ottawa, Canada, E-mail: flo.grenazin@gmail.com
Ebrahim Karimi, Nexus for Quantum Technologies, University of Ottawa, K1N 5N6, ON, Ottawa, Canada; and National Research Council of Canada, Ottawa, Canada, E-mail: ekarimi@uottawa.ca. https://orcid.org/0000-0002-8168-7304

The radially directed fibrillar structure can be easily seen at low magnification. Such fibrils are composed of one or multiple crystals elongated in the radial direction. Such media have been the subject of intense research in the last decade due to their effect on optical beams that couples optical polarisation and inhomogeneous phase transformations. As a consequence of the optical anisotropy of the crystals, spherulites can be considered as one of the simplest examples of patterned anisotropic media. More specifically, Pancharatnam–Berry Optical Elements (PBOEs) [2] are slabs of patterned anisotropic materials whose inhomogeneous orientation of the optic axis can be used to structure the phase and polarisation of light in a way that is conditioned by the polarisation of the input beam. The most known and widely used device of this kind is the q-plate, a PBOE with an optic axis that varies linearly with the azimuthal angle [3, 4]. Q-plates have been used as a tool in different areas [5]: from quantum information and simulation [6, 7] to microscopy and surface structuring [8, 9]. Typically, q-plates are based on liquid crystals, in which case their retardation can be finely controlled either thermally [10] or electrically [11]. More recently, q-plates, as well as other PBOEs, based on subwavelength structures have been developed: from nanostructured glasses [12] to plasmonic metasurfaces [13]. Semiconductor microcavities with similar features have been recently demonstrated [14, 15].

Here, we show how slabs of spherulites – specifically how thin layers of ascorbic acid spherulites – also behave like PBOEs with an azimuthal optic axis dependence. Indeed, when observed in the context of polarized light microscopy, i.e. between crossed polarizers, spherulites display "maltese-cross"-like patterns which strongly resemble q-plate patterns with topological charge $q = 1$ (see Figure 1).

In q-plates, the radial optic pattern introduces an azimuthal phase factor to the light transmitted through it, a factor which is associated with a well-defined amount of Orbital Angular Momentum (OAM). Depending on the input polarisation state, one can generate beams with OAM values of ± 2 or induce singular polarisation patterns, e.g. vector vortex beams. This process is called optical spin to orbit coupling. OAM beams, as well as vector vortex beams, may be exploited to encode classical and quantum information

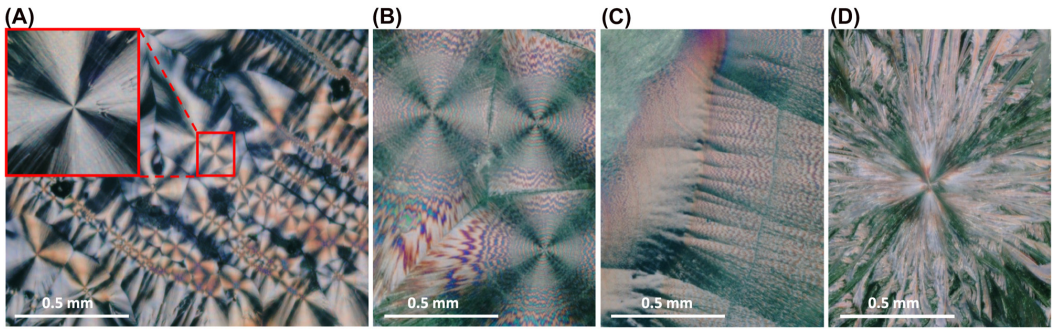

Figure 1: Images of ascorbic acid samples between cross polarizers, illuminated by white light. (A) Sample of ascorbic acid crystals grown at room temperature, from a 10:1 ethanol:water solution. Many "maltese-cross"-like patterns are visible, delimited by boundary regions. In the top left corner, a singled out pattern is enlarged. (B) Sample of ascorbic acid crystals grown at 80 °C, from a pure water solution. The "maltese-cross"-like patterns exhibit a double-banded structure visible as concentric rings of alternating colours. (C) Sample grown in the same conditions as B. Point defects aligned close together on a physical boundary cause a different pattern to arise in the sample. The double-bandedness remains visible, without the cross pattern. (D) Sample of ascorbic acid crystals grown at 120 °C, from a pure water solution. A "maltese-cross"-like pattern is visible, but appears disorganized and coarse. The fibrils themselves are almost recognizable.

[11, 16–20]. Spin–orbit coupling is the basic phenomenon behind the optical spin Hall effect [21, 22].

Spherulite-like structures are observed when evaporating solutions of ascorbic acid dissolved in water (or other solvents, like ethanol). We confirmed our prediction by performing interferometric experiments to ascertain the OAM character of the transmitted beam and spatial Stokes polarimetry to reconstruct the generated polarisation patterns during and after the spherulite formation.

2 Materials and methods

Ascorbic acid ($C_6H_8O_6$), commonly referred to as vitamin C, forms biaxial crystals with monoclinic spheroidal crystal units of $P2_1$ symmetry [23, 24]. The unit cell and indicatrix ellipsoid are shown in Figure 2(A), and the molecular structure of ascorbic acid is shown in Figure 2(C). The molecules themselves are roughly planar and at room temperature growth they are almost strictly oriented in the (010) plane (the plane generated by the axes a and c in Figure 2(A)), the smallest refractive index of the indicatrix is aligned in the b direction.

In our experiment, commercially available ascorbic acid was spread over a slide, dissolved in a solution which was made to evaporate and leave free and dispersed ascorbic acid molecules in the sample. Water and ascorbic acid have great affinity, however, due to its high surface tension, water does not spread out as well on the slide and can take up to a couple hours to dry, at room temperature [25]. The choices of solvent and temperature are important as they determine the thickness of the sample (which affects the retardation), the rate of crystal formation, subtle variations in crystal structure, and the number of molecules present on the slide (whether or not the effects will be visible). Therefore, at first, we chose to dissolve the ascorbic

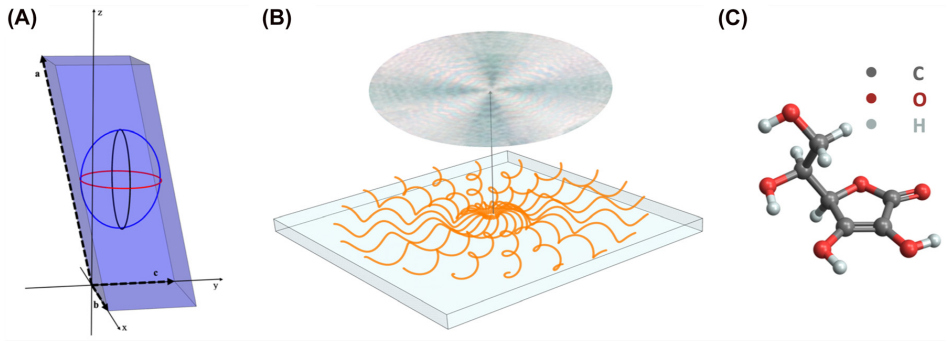

Figure 2: Structure of ascorbic acid spherulites. (A) Schematic of the ascorbic acid crystal unit cell and indicatrix ellipsoid. The three axes of the unit cell are: $a = 17.299(8)$ Å, $b = 6.353(3)$ Å, $c = 6.411(3)$ Å, with $\omega = 102°11'(08')$ the angle between a and c. The three axes of the ellipsoid are: $\alpha = 1.46$, $\beta = 1.6$, $\gamma = 1.75$, with α parallel to b. (B) Twisting of indicatrix ellipsoid along the fibril growth directions. (C) The molecular structure of ascorbic acid. Legend: C, carbon; O, oxygen; H, hydrogen.

acid at room temperature in a solution of 1:10 ethanol:water [26]. On the sample, the spherulite structures formed around point defects from residual powder grains, either accidentally present from undissolved powder grains in the solution or introduced manually after evaporation [25, 27–29]. There is a large variety of patterns that can be observed under different conditions of humidity and temperature [1, 29]. In particular, in specific humidity conditions (relative humidity $RH \approx 30-40\%$) and at room temperature [29], one can observe "maltese-cross"-like patterns when viewing the sample between crossed polarizers and under white light illumination (see Figure 1(A)). Under different conditions, for example at slightly higher temperatures, the crystals can form with a twist, rotating around the fibrillar axis at a certain angle, resulting in a periodic rotation of the indicatrix ellipsoid along the radial direction [30]. This alternation of adjacent regions of relative high and low birefringence forms "banded maltese-cross"-like patterns, where, when viewed under cross-polarizers, regularly spaced concentric rings of alternating brightness appear overtop of the cross-like intensity pattern. In the case of ascorbic acid, "double-banded maltese-cross" patterns form because of the biaxial nature of the rotating ellipsoid [Figure 1(B) and (C)]. By choosing pure water as a solvent which we heated at near boiling point, we observed the double-banded patterns more clearly. In more extreme conditions at higher temperatures, the spherulite patterns become coarse and less organized (see Figure 1(D)).

3 Results

In order to understand the action of ascorbic acid crystals on a light beam around point defects we can adopt the model of a wave retarder with an inhomogeneous optic axis orientation. This model works equally for biaxial media once one fixes the propagation direction of the transmitted light. In such a case, there are still two (effective) refractive indexes associated with specific orthogonal polarizations, which can be calculated by knowing the wavevector of the incident beam and the orientation of the index ellipsoid (see e.g. [31]). In the following, we conventionally define as "optic axis" the axis corresponding to the highest refractive index experienced by the incident light beam. Assuming the sample is sufficiently thin and lying in the plane $z = 0$, we have an optic axis angle θ which is a function of the azimuthal angle and radius in cylindrical coordinates: $\theta(\rho, \phi)$. The action of an anisotropic uniaxial medium can be expressed by the following Jones matrix, written in circular polarization basis:

$$U(\delta, \theta) = \cos\left(\frac{\delta}{2}\right)\begin{bmatrix}1 & 0\\ 0 & 1\end{bmatrix} + i\sin\left(\frac{\delta}{2}\right)\begin{bmatrix}0 & \mathrm{e}^{-2i\theta}\\ \mathrm{e}^{2i\theta} & 0\end{bmatrix}, \quad (1)$$

where the parameter δ is the optical retardation of the medium, $\delta = 2\pi(n_1 - n_2)d/\lambda$, with $n_{1,2}$ the two effective refractive indices, d the sample thickness and λ the wavelength. Note that δ can be position dependent as well, and in particular, in the case of banded "maltese-cross"-like patterns.

At half-wave retardation $\delta = \pi$, the effect of such a medium is to invert the handedness of circular polarisation and introduce a phase factor $\exp(\pm i2\theta(\rho, \phi))$, where the $+$sign is in the case of input left circular polarisation, and the $-$sign for input right circular polarisation. In particular, media characterized by the optic axis angle anisotropy

$$\theta_q(\rho, \phi) = q\phi + \theta_0, \quad (2)$$

where q is the topological charge of the molecular director field and θ_0 an offset angle, introduce azimuthal phase factors of $\exp(\pm i2\theta_0)\exp(\pm i2q\phi)$. Beams characterized by $\exp(i\ell\phi)$ factors are known for carrying a well-defined amount of OAM equal to $N\hbar\ell$ (where N is the average number of photons). Therefore, the medium described by $U(\pi, \theta_q)$ is converting the input spin angular momentum (SAM) of each input photon into OAM, a process known as SAM-to-OAM conversion (STOC), first investigated with q-plates [4]. Moreover, an input beam that is linearly polarized (or in a generic elliptical polarisation state) will be transformed into a non-separable state of polarisation and OAM, which manifests in inhomogeneous polarisation patterns [32, 33].

To test that our samples of ascorbic acid spherulites have a local optic axis around defects of $\theta = \phi$, we observed both the STOC phenomenon and the generation of inhomogeneous polarisation patterns.

3.1 Experimental characterization of the optic axis pattern

We first confirmed that the ascorbic acid crystals orient radially by measuring the optic axis pattern $\theta := \theta(\rho, \phi)$. This can be done by shining the sample with circular polarisation and projecting the transmitted beam into a linear polarisation state. The resulting intensity distribution is given by

$$I(\rho, \phi) \propto 1 + \sin(\delta)\sin(2\theta(\rho, \phi)), \quad (3)$$

where we assumed input right-circular polarisation and a projection on horizontal polarisation. The measurement was performed with a 633 nm diode laser source. At this wavelength our sample exhibits a retardation close to $\delta = \pi/2$, ensuring a good visibility of the intensity modulation in the measured pattern. As shown in Figure 3(B), near point defects, the recorded intensity distribution (averaged over different radial positions) is well described by the relation $\theta = \phi$, associated with a radial distribution of the molecular director around the defect. In proximity of boundaries

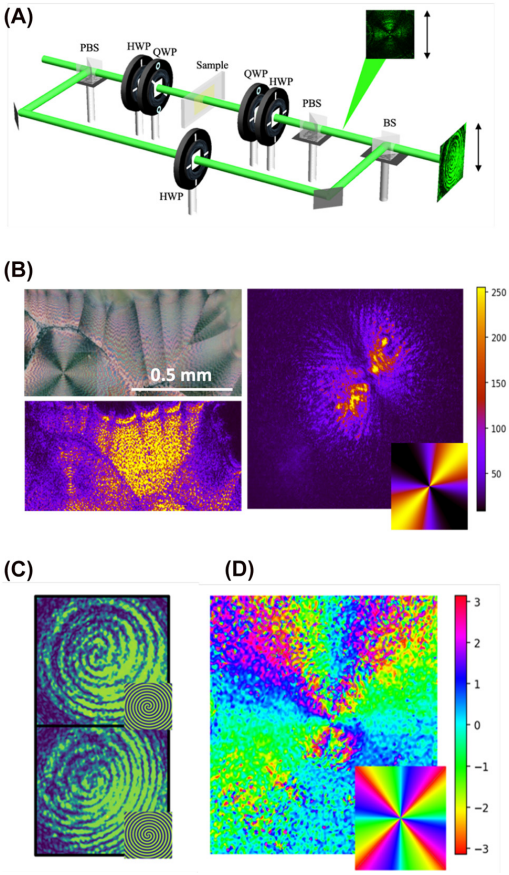

Figure 3: Structured light emerging from ascorbic acid spherulites. (A) Schematics of the interferometry and polarimetry setups. The reference beam's polarization is rotated in the reference arm to ensure non-orthogonal polarizations at the output of the BS. A lens (not shown) is also added to the reference arm to induce a spherical wavefront onto the reference Gaussian beam. For polarization tomography, the reference beam is ignored and the camera is placed between the PBS and the BS, as shown. (B) Intensity patterns characterizing the optic axis angle in two different regions of the sample. Right-circular polarization is incident on the sample and projected onto horizontal polarization, resulting in an intensity distribution related to the optic axis angle by 3. On the right, the distribution around a defect. It matches the simulated intensity for $\theta = \phi$, shown in the bottom right corner. On the bottom left, the intensity distribution of the image above, showing a region near a physical boundary. The intensity does not vary in that region. (C) On top, interference pattern generated with input right circular polarization, compared to the theoretical pattern between a spherical Gaussian and a beam carrying OAM +2. On the bottom, interference pattern generated with input left circular polarization, compared to the theoretical pattern between a spherical Gaussian and a beam carrying OAM -2. (D) Density plot of the major axes of the point-by-point polarization ellipses from a beam transmitted through a defect region of the sample. The V-point is visible. A simulation of the expected density plot is shown in the bottom right corner.

which separate regions containing point defects, we observe a jump in the optic axis angle.

3.2 STOC in ascorbic acid samples

A simple way to ascertain the generation of OAM in a laser beam is to look at its interference with a reference Gaussian beam [4]. It is easy to show that, in the case of co-propagating beams, the interference pattern consists of spiral fringes where the number of arms is dictated by the OAM absolute value of the analyzed beam, and the handedness by the OAM sign (see insets in Figure 3(C) for simulations). We thus verified this result by inserting the samples in one arm of an interferometer and recording the interference pattern for right-handed and left-handed circular polarisation inputs (the experimental setup is shown in Figure 3(A)). We used a laser beam at 525 nm, where the optical retardation of the samples is typically close to π. This was checked by looking at the conversion efficiency from left circular to right circular polarization [5].

The resulting interference patterns are shown in Figure 3(C) for right and left circular polarisations, respectively, showing that the STOC phenomenon is realized.

3.3 Polarimetry of vector modes

As the next step we illuminated the sample with the same laser beam but with linear polarisation. The q-plate model predicts that the resulting field, on the sample plane and at half-wave retardation, is given by

$$\mathbf{E}_{\text{out}}(\rho,\phi) \propto \left(e^{i2\phi}\mathbf{e}_R + e^{-i2\phi}\mathbf{e}_L\right)e^{-\rho^2/w^2}, \tag{4}$$

where we assumed a Gaussian envelope field with waist w, and $\mathbf{e}_{R,L} = \left(\mathbf{x} \pm i\mathbf{y}\right)/\sqrt{2}$, with $\mathbf{x}$ and $\mathbf{y}$ the unit vectors of the x and y axes. Such a field is linearly polarised everywhere but with an angle of the polarisation ellipse given by ϕ and a singular point on the beam axis (known as a "V"-point) [33]. A detailed account of polarization singularities emerging from biaxial media is given in Ref. [34]. We observed the generation of these patterns by a point-by-point measurement of the Stokes parameters, defined by: $s_0 = I_{\text{total}}$, $s_1 = I_H - I_V$, $s_2 = I_A - I_D$, $s_3 = I_L - I_R$, where $I_{H,V,A,D,L,R}$ are the intensities of, respectively, horizontal, vertical, anti-diagonal, diagonal, left circular and right circular polarisation, and I_{total} stands for total intensity. These intensities, and consequently the Stokes parameters, can all be easily measured by a sequence containing a quarter-wave plate, a half-wave plate and a polarizing beam splitter (Figure 3(A)). In particular, the density plot of the

polarisation ellipse orientation (which is the phase of the field $s_1 + is_2$) clearly shows a singular pattern (Figure 2(D)). By according the different projection intensities on a camera, we reconstructed the local polarisation ellipse. The resulting pattern is quantitatively close to the expected one. Due to the optical retardation not being exactly π, the "V"-point is split in four points of circular polarisation ("C"-points) each with a topological charge 1/2 (see also ref. [33]).

The generation of singular polarization patterns was observed also during the growth of the sample (Figure 4). Figure 4 shows how the radial pattern appears first around the defect and then spreads through the sample.

4 Discussion

We have shown that ascorbic acid spherulites crystallize around defects, in the absence of twisting, with a local optic axis pattern of $\theta = \phi$. We have also shown experimentally the generation of OAM modes and vector beams. Our findings show how ascorbic acid can be exploited as a material for fabricating devices which exploit photonic spin–orbit phenomena. In future, we plan to develop techniques to better control the growth of the ascorbic acid samples in ways analogous to what is done with liquid crystals [5].

The radial growth around the defect is likely the most energetically efficient way to form the hydrogen bonds between atoms inside the crystal. It can be interesting to explore the different crystallization structures when ascorbic acid is grown on a polar substrate, instead of around a defect on a neutral glass substrate.

Ascorbic acid is part of a large family of spherulites, each of which has structures suggesting certain anisotropy of optic axis patterns around defects. It would be interesting to explore the STOC phenomena in other kinds of spherulites, which may have advantages over ascorbic acid. In particular, while ascorbic acid has relevant absorption above 1.5 THz [35], the recently demonstrated controlled generation of quartz spherulites [36, 37] may offer an interesting way for creating vortex beams in the TeraHertz frequency domain [38] (q plates for this regime have been recently realized using either 3D printing techniques [39] or quartz segmented waveplates [40]). It would also shed light on the role of different crystal structures and symmetries in the shaping of light.

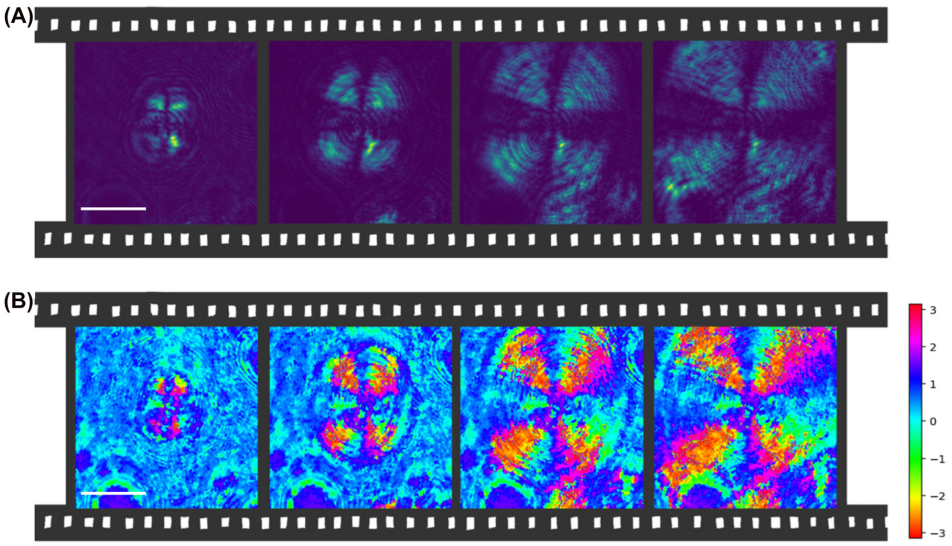

Figure 4: Frames showing the evolution of polarization distribution during the growth of the sample at $t = 0$ min, 6.5 min, 12.8 min, 19.1 min. The sample was grown at room temperature, from a solution of 10:1 ethanol:water. (A) Intensity of the beam between cross polarizers at different times during crystal growth. (B) Plot of the major axis angle of the point-by-point polarization ellipses at different times during crystal growth.

Author contributions: All the authors have accepted responsibility for the entire content of this submitted manuscript and approved submission.
Research funding: This work was supported by the Canada Research Chairs (CRC) and Canada First Research Excellence Fund (CFREF) Program, and Joint Centre for Extreme Photonics (JCEP).
Conflict of interest statement: The authors declare no conflicts of interest regarding this article.

References

[1] B. Crist and J. M. Schultz, "Polymer spherulites: a critical review," *Prog. Sci. Polym.*, vol. 56, p. 1, 2016.
[2] L. Marrucci, C. Manzo, and D. Paparo, "Pancharatnam-berry phase optical elements for wave front shaping in the visible domain: switchable helical mode generation," *Appl. Phys. Lett.*, vol. 88, p. 221102, 2006.
[3] G. Biener, A. Niv, V. Kleiner, and E. Hasman, "Formation of helical beams by use of pancharatnam—berry phase optical elements," *Opt. Lett.*, vol. 27, p. 1875, 2002.
[4] L. Marrucci, C. Manzo, and D. Paparo, "Optical spin-to-orbital angular momentum conversion in inhomogeneous anisotropic media," *Phys. Rev. Lett.*, vol. 96, p. 163905, 2006.
[5] A. Rubano, F. Cardano, B. Piccirillo, and L. Marrucci, "Q-plate technology: a progress review," *JOSA B*, vol. 36, p. D70, 2019.
[6] E. Nagali, F. Sciarrino, F. De Martini, et al., "Quantum information transfer from spin to orbital angular momentum of photons," *Phys. Rev. Lett.*, vol. 103, p. 013601, 2009.
[7] F. Cardano, E. Karimi, L. Marrucci, C. de Lisio, and E. Santamato, "Generation and dynamics of optical beams with polarization singularities," *Opt. Express*, vol. 21, p. 8815, 2013.
[8] L. Yan, P. Gregg, E. Karimi, et al., "Q-plate enabled spectrally diverse orbital-angular-momentum conversion for stimulated emission depletion microscopy," *Optica*, vol. 2, p. 900, 2015.
[9] E. Karimi, B. Piccirillo, E. Nagali, L. Marrucci, and E. Santamato, "Efficient generation and sorting of orbital angular momentum eigenmodes of light by thermally tuned q-plates," *Appl. Phys. Lett.*, vol. 94, p. 231124, 2009.
[10] J. J. J. Nivas, S. He, A. Rubano, et al., "Direct femtosecond laser surface structuring with optical vortex beams generated by a q-plate," *Sci. Rep.*, vol. 5, p. 1, 2015.
[11] B. Piccirillo, V. D'Ambrosio, S. Slussarenko, L. Marrucci, and E. Santamato, "Photon spin-to-orbital angular momentum conversion via an electrically tunable q-plate," *Appl. Lett.*, vol. 97, p. 4085, 2010, arXiv:1010.4473.
[12] M. Beresna, M. Gecevičius, P. G. Kazansky, and T. Gertus, "Radially polarized optical vortex converter created by femtosecond laser nanostructuring of glass," *Appl. Phys. Lett.*, vol. 98, p. 201101, 2011.
[13] E. Karimi, S. A. Schulz, I. De Leon, H. Qassim, J. Upham, and R. W. Boyd, "Generating optical orbital angular momentum at visible wavelengths using a plasmonic metasurface," *Light: Sci. Appl.*, vol. 3, p. e167, 2014.
[14] A. Kavokin, G. Malpuech, and M. Glazov, "Optical spin hall effect," *Phys. Rev. Lett.*, vol. 95, p. 136601, 2005.
[15] N. C. Zambon, P. St-Jean, M. Milićević, et al., "Optically controlling the emission chirality of microlasers," *Nat. Photonics*, vol. 13, p. 283, 2019.
[16] V. D'Ambrosio, E. Nagali, S. P. Walborn, et al., "Complete experimental toolbox for alignment-free quantum communication," *Nat. Commun.*, vol. 3, p. 961, 2012.
[17] R. Fickler, R. Lapkiewicz, W. N. Plick, et al., "Quantum entanglement of high angular momenta," *Science*, vol. 338, p. 640, 2012.
[18] G. Vallone, V. D'Ambrosio, A. Sponselli, et al., "Free-space quantum key distribution by rotation-invariant twisted photons," *Phys. Rev. Lett.*, vol. 113, p. 060503, 2014.
[19] A. E. Willner, Y. Ren, G. Xie, et al., "Recent advances in high-capacity free-space optical and radio-frequency communications," *Philos. Trans. R. Soc., A*, vol. 375, p. 20150439, 2017.
[20] A. Sit, R. Fickler, F. Alsaiari, et al., "Quantum cryptography with structured photons through a vortex fiber," *Opt. Lett.*, vol. 43, p. 4108, 2018.
[21] K. Yu Bliokh and Y. P. Bliokh, "Conservation of angular momentum, transverse shift, and spin hall effect in reflection and refraction of an electromagnetic wave packet," *Phys. Rev. Lett.*, vol. 96, p. 073903, 2006.
[22] S. Liu, S. Chen, S. Wen, and H. Luo, "Photonic spin hall effect: fundamentals and emergent applications," *Opto-Electron. Sci.*, vol. 1, p. 220007, 2022.
[23] E. G. Cox, "Crystalline structure of hexuronic acid," *Nature*, vol. 130, p. 205, 1932.
[24] J. Hvoslef, "The crystal structure of l-ascorbic acid, 'vitamin c'. i. the x-ray analysis," *Acta Crystallogr. Sect. B: Struct. Crystallogr. Cryst. Chem.*, vol. 24, p. 23, 1968.
[25] H. Uesaka and R. Kobayashi, "Pattern formation in the crystallization of ascorbic acid," *J. Cryst. Growth*, vol. 237, p. 132, 2002.
[26] W. Omar, *Effect of Solvent Composition on Cristallization Process of Ascorbic Acid*, vol. 29, Weinheim, Chemical Engineering & Technology: Industrial Chemistry-Plant Equipment-Process Engineering-Biotechnology, 2006. Available at: https://doi.org/10.1002/ceat.200500283.
[27] Y. Yamazaki, H. Yoshino, M. Izui, Y. Sato, and M. Matsushita, "Humidity—"temperature dependence of domain growth of ascorbic acid crystal"," *J. Phys. Soc. Jpn.*, vol. 78, p. 074001, 2009.
[28] S. K. Kon and M. B. Watson, "The effect of light on the vitamin c of milk," *Biochem. J.*, vol. 30, p. 2273, 1936.
[29] M. Ito, M. Izui, and M. Matsushita, "Morphological diversity in crystal growth of l-ascorbic acid dissolved in methanol," *J. Phys. Soc. Jpn.*, vol. 72, p. 1834, 2003.
[30] F. P. Price, "The structure of high polymer sperulites," *J. Polym. Sci.*, vol. 37, p. 71, 1959.
[31] B. E. A. Saleh and M. C. Teich, *Fundamentals of Photonics*, Hoboken, New Jersey, John Wiley & Sons, 2019.
[32] F. Cardano, E. Karimi, S. Slusarenko, L. Marrucci, E. Santamato, and C. de Lisio, "Polarisation pattern of vector vortex beams generated by q-plates with different topological charges," *Appl. Opt.*, vol. 52, p. C1, 2012.
[33] A. D'Errico, M. Maffei, B. Piccirillo, C. de Lisio, F. Cardano, and L. Marrucci, "Topological features of vector vortex beams

perturbed with uniformly polarized light," *Sci. Rep.*, vol. 7, p. 1, 2017.
[34] M. V. Berry and M. R. Dennis, "The optical singularities of birefringent dichroic chiral crystals," *Proc. R. Soc. London, Ser. A*, vol. 459, p. 1261, 2003.
[35] L. Jiang, M. Li, C. Li, et al., "Terahertz spectra of l-ascorbic acid and thiamine hydrochloride studied by terahertz spectroscopy and density functional theory," *J. Infrared, Millimeter, Terahertz Waves*, vol. 35, p. 871, 2014.
[36] S. Zhou, J. Antoja-Lleonart, P. Nukala, V. Ocelik, N. R. Lutjes, and B. Noheda, "Crystallization of geo2 thin films into alpha-quartz: from spherulites to single crystals," *Acta Mater.*, vol. 215, p. 117069, 2021.
[37] N. R. Lutjes, S. Zhou, J. Antoja-Lleonart, B. Noheda, and V. Ocelík, "Spherulitic and rotational crystal growth of quartz thin films," *Sci. Rep.*, vol. 11, p. 1, 2021.
[38] H. Wang, Q. Song, Y. Cai, et al., "Recent advances in generation of terahertz vortex beams and applications," *Chin. Phys. B*, vol. 29, p. 097404, 2020.
[39] A. I. Hernandez-Serrano, E. Castro-Camus, and D. Lopez-Mago, "q-plate for the generation of terahertz cylindrical vector beams fabricated by 3d printing," *J. Infrared, Millimeter, Terahertz Waves*, vol. 38, p. 938, 2017.
[40] A. Minasyan, C. Trovato, J. Degert, E. Freysz, E. Brasselet, and E. Abraham, "Geometric phase shaping of terahertz vortex beams," *Opt. Lett.*, vol. 42, p. 41, 2017.

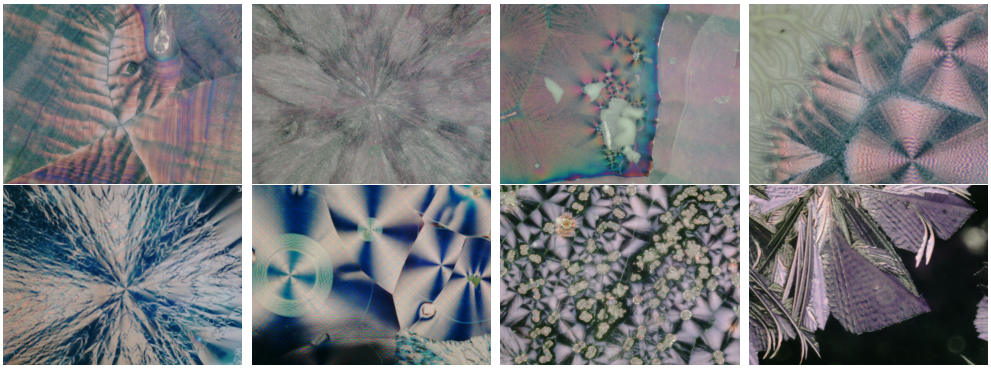

Figure 26: Images of ascorbic acid between cross polarizers, in various conditions of temperature and solvent choices. For the pleasure of the reader.

4 Conclusion

In conclusion, we developed and experimentally demonstrated a super-resolution technique applicable to coincidence imaging setups with potential for low-light imaging applications. We also show that the total FI scales as $\sqrt{K}$, highlighting the super-resolution potential in high-dimensionally entangled light. Despite suffering from cross-talk, the optimal modes measured in the experiment provided enough FI to estimate separations much smaller than the Schmidt beam waist. The clear first step from here would be to repeat the experiment under more controlled circumstances in the lab and to accumulate data repetitively over longer periods of time to get a proper experimentally realizable CRLB for this technique. Additionally, the proof of principle experiment could be repeated with a coherent separation, where we expect the advantages conferred by the high spatial correlations between photons to remain. Given that the use of high-dimensional entanglement

further enhances the advantages of SPADE, it would be interesting to incorporate neural networks into the biphoton SPADE technique. As mentioned previously, conventional SPADE super-resolution has been generalized to and experimentally achieved with arbitrary objects using ML and deconvolution algorithms, which could altogether be enhanced in a biphoton setup like ours. These advances could help achieve high resolution of more complex, light sensitive objects.

Furthermore, we showed, by verifying the OAM character of the output beam, that ascorbic acid crystals grow radially around point defects, with local optic axes varying linearly with the azimuthal angle. We also show that in less ordered crystal growths, the local optic axis adopts dependencies on two other angles, as the crystal grows with small twisting of its radial fibrils. In the future, efforts to tune the growth of ascorbic acid crystals by applying external electric fields or more polar substrates, could allow for more precise control and arbitrary shaping of the structured waveplate. Since ascorbic acid is part of a class of crystal spherulites with similar birefringent properties, it would also be interesting to explore the fabrication and optical properties induced by different spherulite waveplates. In particular, the study of quartz spherulites, which are transparent in the THz regime where standard q-plates are rare, seems like a promising direction for future work in this field.

References

[1] Lorenzo Marrucci, C Manzo, and D Paparo. Pancharatnam-berry phase optical elements for wave front shaping in the visible domain: switchable helical mode generation. *Applied Physics Letters*, 88(22):221102, 2006.

[2] Filippo Cardano, Ebrahim Karimi, Sergei Slussarenko, Lorenzo Marrucci, Corrado de Lisio, and Enrico Santamato. Polarization pattern of vector vortex beams generated by q-plates with different topological charges. *Appl. Opt.*, 51(10):C1–C6, Apr 2012.

[3] Ugo Fano. Description of states in quantum mechanics by density matrix and operator techniques. *Reviews of modern physics*, 29(1):74, 1957.

[4] Franz Schwabl. *Quantum mechanics*. Springer Science & Business Media, 2007.

[5] Jun John Sakurai and Eugene D Commins. Modern quantum mechanics, revised edition, 1995.

[6] S Magnitskiy, D Frolovtsev, V Firsov, P Gostev, I Protsenko, and M Saygin. A spdc-based source of entangled photons and its characterization. *Journal of Russian Laser Research*, 36(6):618–629, 2015.

[7] ZY Ou and L Mandel. Violation of bell's inequality and classical probability in a two-photon correlation experiment. *Physical review letters*, 61(1):50, 1988.

[8] SS Straupe, DP Ivanov, AA Kalinkin, IB Bobrov, and SP Kulik. Angular schmidt modes in spontaneous parametric down-conversion. *Physical Review A*, 83(6):060302, 2011.

[9] Filippo M Miatto, Thomas Brougham, and Alison M Yao. Cartesian and polar schmidt bases for down-converted photons. *The European Physical Journal D*, 66(7):1–8, 2012.

[10] Frédéric Bouchard, Natalia Herrera Valencia, Florian Brandt, Robert Fickler, Marcus Huber, and Mehul Malik. Measuring azimuthal and radial modes of photons. *Optics express*, 26(24):31925–31941, 2018.

[11] Eliot Bolduc, Nicolas Bent, Enrico Santamato, Ebrahim Karimi, and Robert W Boyd. Exact solution to simultaneous intensity and phase encryption with a single phase-only hologram. *Optics letters*, 38(18):3546–3549, 2013.

[12] Isabelle Percheron, Jeffrey T Baker, Mark Gruneisem, Ty Martinez, and David Wick. Blazed holographic optical aberration compensation. In *Adaptive Optics For Industry And Medicine*, pages 384–388. World Scientific, 2000.

[13] Luigi Santamaria, Deborah Pallotti, Mario Siciliani de Cumis, Daniele Dequal, and Cosmo Lupo. Balanced spade detection for distance metrology. *arXiv preprint arXiv:2206.05246*, 2022.

[14] Fan Yang, Arina Tashchilina, Eugene S Moiseev, Christoph Simon, and Alexander I Lvovsky. Far-field linear optical superresolution via heterodyne detection in a higher-order local oscillator mode. *Optica*, 3(10):1148–1152, 2016.

[15] Colin JR Sheppard. The development of microscopy for super-resolution: confocal microscopy, and image scanning microscopy. *Applied Sciences*, 11(19):8981, 2021.

[16] JW Gordon. Diffraction in optical instruments. *Journal of the Royal Microscopical Society*, 25(5):563–565, 1905.

[17] Claudette M St. Croix, Stuart H Shand, and Simon C Watkins. Confocal microscopy: comparisons, applications, and problems. *Biotechniques*, 39(6):S2–S5, 2005.

[18] James B Pawley. Fundamental limits in confocal microscopy. In *Handbook of biological confocal microscopy*, pages 20–42. Springer, 2006.

[19] Mats GL Gustafsson. Surpassing the lateral resolution limit by a factor of two using structured illumination microscopy. *Journal of microscopy*, 198(2):82–87, 2000.

[20] Manish Saxena, Gangadhar Eluru, and Sai Siva Gorthi. Structured illumination microscopy. *Advances in Optics and Photonics*, 7(2):241–275, 2015.

[21] Eric Betzig, George H Patterson, Rachid Sougrat, O Wolf Lindwasser, Scott Olenych, Juan S Bonifacino, Michael W Davidson, Jennifer Lippincott-Schwartz, and Harald F Hess. Imaging intracellular fluorescent proteins at nanometer resolution. *science*, 313(5793):1642–1645, 2006.

[22] Stefan W Hell and Jan Wichmann. Breaking the diffraction resolution limit by stimulated emission: stimulated-emission-depletion fluorescence microscopy. *Optics letters*, 19(11):780–782, 1994.

[23] Jerry Tersoff and Donald R Hamann. Theory of the scanning tunneling microscope. *Physical Review B*, 31(2):805, 1985.

[24] KD Vernon-Parry. Scanning electron microscopy: an introduction. *III-Vs Review*, 13(4):40–44, 2000.

[25] Daniel Rugar and Paul Hansma. Atomic force microscopy. *Physics today*, 43(10):23–30, 1990.

[26] Mankei Tsang, Ranjith Nair, and Xiao-Ming Lu. Quantum theory of superresolution for two incoherent optical point sources. *Physical Review X*, 6(3):031033, 2016.

[27] Jeffrey H Shapiro and Robert W Boyd. The physics of ghost imaging. *Quantum Information Processing*, 11(4):949–993, 2012.

[28] Alessandra Gatti, Enrico Brambilla, Morten Bache, and Luigi A Lugiato. Ghost imaging with thermal light: comparing entanglement and classicalcorrelation. *Physical review letters*, 93(9):093602, 2004.

[29] Avshalom C Elitzur and Lev Vaidman. Quantum mechanical interaction-free measurements. *Foundations of Physics*, 23(7):987–997, 1993.

[30] Yingwen Zhang, Alicia Sit, Frédéric Bouchard, Hugo Larocque, Florence Grenapin, Eliahu Cohen, Avshalom C Elitzur, James L Harden, Robert W Boyd, and Ebrahim Karimi. Interaction-free ghost-imaging of structured objects. *Optics express*, 27(3):2212–2224, 2019.

[31] Paul-Antoine Moreau, Ermes Toninelli, Peter A Morris, Reuben S Aspden, Thomas Gregory, Gabriel Spalding, Robert W Boyd, and Miles J Padgett. Resolution limits of quantum ghost imaging. *Optics express*, 26(6):7528–7536, 2018.

[32] Ronan Kerviche, Saikat Guha, and Amit Ashok. Fundamental limit of resolving two point sources limited by an arbitrary point spread function. In *2017 IEEE International Symposium on Information Theory (ISIT)*, pages 441–445. IEEE, 2017.

[33] Martin Paúr, Bohumil Stoklasa, Zdenek Hradil, Luis L Sánchez-Soto, and Jaroslav Rehacek. Achieving the ultimate optical resolution. *Optica*, 3(10):1144–1147, 2016.

[34] Pauline Boucher, Claude Fabre, Guillaume Labroille, and Nicolas Treps. Spatial optical mode demultiplexing as a practical tool for optimal transverse distance estimation. *Optica*, 7(11):1621–1626, 2020.

[35] Weng-Kian Tham, Hugo Ferretti, and Aephraim M Steinberg. Beating rayleigh's curse by imaging using phase information. *Physical review letters*, 118(7):070801, 2017.

[36] Jing Yang, Shengshi Pang, Yiyu Zhou, and Andrew N Jordan. Optimal measurements for quantum multiparameter estimation with general states. *Physical Review A*, 100(3):032104, 2019.

[37] Sisi Zhou and Liang Jiang. Modern description of rayleigh's criterion. *Physical Review A*, 99(1):013808, 2019.

[38] Zdeněk Hradil, Jaroslav Řeháček, Luis Sánchez-Soto, and Berthold-Georg Englert. Quantum fisher information with coherence. *Optica*, 6(11):1437–1440, 2019.

[39] Kevin Liang, Sultan Abdul Wadood, and AN Vamivakas. Coherence effects on estimating two-point separation. *Optica*, 8(2):243–248, 2021.

[40] Stanislaw Kurdzialek. Back to sources–the role of coherence in super-resolution imaging revisited. *arXiv preprint arXiv:2103.12096*, 2021.

[41] Stanislaw Kurdzialek. Back to sources–the role of losses and coherence in super-resolution imaging revisited. *Quantum*, 6:697, 2022.

[42] Carl W Helstrom. Quantum detection and estimation theory. *Journal of Statistical Physics*, 1(2):231–252, 1969.

[43] Kevin Liang, SA Wadood, and AN Vamivakas. Quantum fisher information for estimating n partially coherent point sources. *Optics Express*, 31(2):2726–2743, 2023.

[44] Katherine KM Bearne, Yiyu Zhou, Boris Braverman, Jing Yang, SA Wadood, Andrew N Jordan, AN Vamivakas, Zhimin Shi, and Robert W Boyd. Confocal super-resolution microscopy based on a spatial mode sorter. *Optics Express*, 29(8):11784–11792, 2021.

[45] AA Pushkina, G Maltese, JI Costa-Filho, P Patel, and AI Lvovsky. Superresolution linear optical imaging in the far field. *Physical Review Letters*, 127(25):253602, 2021.

[46] Manuel Gessner, Claude Fabre, and Nicolas Treps. Superresolution limits from measurement crosstalk. *Physical Review Letters*, 125(10):100501, 2020.

[47] Yink Loong Len, Chandan Datta, Michał Parniak, and Konrad Banaszek. Resolution limits of spatial mode demultiplexing with noisy detection. *International Journal of Quantum Information*, 18(01):1941015, 2020.